Master's thesis

NTNU
Norwegian University of Science and Technology
Faculty of Natural Sciences
Department of Biotechnology and Food Science

Karina Gjerdevik Osebakken

Conformation of the Acid Form of Xanthan in Water and DMSO

Master's thesis in Chemical Engineering and Biotechnology
Supervisor: Prof. Bjørn E. Christensen
June 2019

NTNU
Norwegian University of
Science and Technology

Karina Gjerdevik Osebakken

Conformation of the Acid Form of Xanthan in Water and DMSO

Master's thesis in Chemical Engineering and Biotechnology
Supervisor: Prof. Bjørn E. Christensen
June 2019

Norwegian University of Science and Technology
Faculty of Natural Sciences
Department of Biotechnology and Food Science

NTNU
Norwegian University of
Science and Technology

Preface

This master thesis was written during the spring of 2019 at the Norwegian University of Science and Technology (NTNU) in Trondheim. The lab work was performed at the biopolymer laboratory at the Department of Biotechnology, NTNU Trondheim and in the Sato laboratory at the Department of Macromolecular Science at Osaka University, Toyonaka in Japan.

I would start to thank my primary supervisor, professor Bjørn E. Christensen for exciting projects, both the project work in the autumn of 2018 and the master thesis itself. Thank you for interesting discussions, your guidance and help throughout the projects. I would also like to thank my co-supervisor during the project work, doctor Marianne Øksnes Dalheim, for teaching me good lab routines and procedures crucial to this master project. Senior engineer at IBT, NTNU Trondheim, Ann-Sissel T. Ulset also have my most enormous gratitude for helping me run SEC-MALS-VISC analysis and for helping me out in the lab on a daily basis.

Furthermore, I would like to thank the KIFEE project for providing me with funding to perform parts of my master project in the Sato laboratory at Osaka University, Japan. I am forever grateful to professor Takahiro Sato and professor Ken Terao for welcoming me in their lab and to doctor Tetiana Sezonenko for helping me out in the Sato laboratory and for showing me cultural aspects of Japan during my stay.

With this thesis, I finish up my five years as a student in the master program Chemical Engineering and Biotechnology. The study has provided me with knowledge which I will carry with me further in my career, but also great friendships and connections. I want to give my last thanks to my friends, family and boyfriend for supporting me through good and bad days. This degree would not have been possible without you.

17 June 2019

Karina Gjerdevik Osebakken

Abstract

Xanthan is a high molecular weight polysaccharide widely used in industrial applications due to its ability to provide high solution viscosity at even low concentrations. The viscosifying property is partially caused by its native structure, which is widely accepted to be a double helix. The helix does, however, dissociate upon heating under low ionic strength in aqueous solutions or when the solvent is changed, a phenomenon referred to as order-disorder transitions. In this work, xanthan samples, mechanically degraded by high shear forces, were characterised to establish a procedure that prevents order-disorder transitions during degradation from taking place. Such a procedure could, in turn, allow for more efficient degradation of xanthan samples and thus make analysis or, e.g. chemical modifications more feasible. The mechanically degraded samples were further used to study the conformation of xanthan in water, pure DMSO and water/DMSO mixtures, based a publication by Fantou *et al.*, claiming xanthan to be disordered in DMSO through CD. The aim has been to reproduce the CD spectra in order to confirm a possible disorder in DMSO and determine at which fraction of DMSO (f_{DMSO}) the disorder occur, which in turn could allow for a wide range of new possibilities in terms of chemical modifications in the disordered state.

By analyses using SEC-MALS-VISC, mechanical degradation by high shear forces was found to be a suitable and efficient method for reducing the molecular weight, intrinsic viscosity and radius of gyration. However, to maintain the ordered conformation, the ionic strength during mechanical degradation had to be kept high, i.e. 2 M (0.5 M $MgSO_4$). It was found that desalting of the degraded samples by dialysis at room temperature gives rise to a more flexible, but yet ordered conformation, compared to degraded and non-purified samples. Dialysis gave rise to various salt-forms, which were also found to influence the conformation after purification: Mg^{2+} as counterion resulted in the most ideal and rigid conformation, compared to both H^+ and Na^+. An improved, ordered conformation was also found when acetate and pyruvate substituents were removed from the degraded xanthan.

The study of xanthan in DMSO, proved mechanically degraded xanthan to be directly soluble in DMSO without heating, when on the acid form. Acidic xanthan in water was found to have an ellipticity decreasing linearly with increasing temperature by CD, suggesting no thermal order-disorder transition in the measured temperature interval, 20 to 90°C. CD of acidic xanthan in DMSO, on the other hand, was found to be impossible at the required wavelength due to

absorption of light. This finding raises a question to the CD spectra claiming disorder in DMSO. However, f_{DMSO} was determined to be approximately 0.8 by optical rotation and capillary viscometry of water/DMSO mixtures, suggesting that DMSO as solvent influences the xanthan molecules, and may cause order-disorder transitions. The molecular weights and radii of gyration of xanthan samples dissolved in both pure water and DMSO were found to be independent of temperature in the interval 20 to 50°C, measured by light scattering. This suggests that no thermal order-disorder transition takes place. It was further found that xanthan in pure DMSO has higher apparent molecular weights and radii of gyration compared to aqueous solvent. As the disordered state have both lower molecular weights and smaller radii of gyration, the findings suggest that xanthan does not become disordered in DMSO.

Sammendrag

Xantan er et høymolekylært polysakkarid som på grunn av sine viskositetsfremmende egenskaper er mye brukt i ulike industrier. Disse egenskapene skyldes strukturen, hvilket er bekreftet å være en dobbel heliks. Heliksen dissosierer imidlertidig ved oppvarming under lav ionestyrke i vann eller dersom løsningsmiddelet endres, et fenomen kalt orden-uorden transisjoner. I denne masteroppgaven har xantan blitt mekanisk nedbrutt av høye skjærkrefter og karakterisert for å etablere en prosedyre som forhindrer orden-uorden transisjoner under nedbryting. En slik prosedyre kan muliggjøre mer effektiv nedbryting av xantan og dermed gjøre analyser eller f. eks. kjemisk modifisering mer gunstig å gjennomføre. Basert på en publikasjon fra Fantou med flere, som gjennom CD spektroskopi fant at xantan er uordnet løst i DMSO, ble de mekanisk nedbrutte xantan prøvene brukt for å undersøke konformasjonen i rent vann, ren DMSO og vann/DMSO blandinger. Målet var å bekrefte en mulig uorden i DMSO ved reprodusere CD spektrumet og undersøke ved hvilken vektfraksjon av DMSO uorden forekommer. I en større sammenheng kan uorden i DMSO muliggjøre nye analysemetoder og kjemisk modifisering i uordnet tilstand.

Fra SEC-MALS-VISC analyse ble mekanisk nedbryting av høye skjærkrefter funnet å være en effektiv metode for å redusere molekylvekt, egenviskositet og gyrasjonsradius. For å opprettholde ordnet konformasjon må imidlertidig ionestyrken under nedbryting være høy, nærmere bestemt 2 M (0.5 M $MgSO_4$). Avsalting gjennom dialyse resulterte i mer en mer fleksibel, men likevel ordnet konformasjon, sammenlignet med nedbrutte, salt-rike prøver. Konformasjonen til de nedbrutte prøvene var også avhengig av saltformen til xantanet, generert gjennom dialyse, hvor saltformen med Mg^{2+} som motion resulterte i den mest ideelle og rigide konformasjonen, sammenlignet med H^+ and Na^+. Fjerning av acetat og pyruvat fra det nedbrutte xanthanet forårsaket også en mer rigid konformasjon sammenlignet med de substituerte prøvene.

Gjennom studien av xantan i DMSO ble syreformen av xantan funnet å være direkte løselig i DMSO, uten oppvarming. CD viste at syreformen av xantan i rent vann har en lineært avtagende elliptisitet ved økende temperatur, hvilket indikerer at orden-uorden transisjoner ikke forekommer i det målte temperaturintervallet, 20 til 90°C. CD av syreformen i DMSO var derimot umulig på spesifisert bølgelengde, grunnet høy absorpsjon av lys. Denne oppdagelsen stiller spørsmål til CD spektrumet som viser uorden i DMSO. Likevel ble f_{DMSO} bestemt til å

være omtrent 0.8 gjennom optisk rotasjon og kapillærviskometri, hvilket indikerer at DMSO påvirker xantanmolekylene og forårsaker muligens orden-uorden transisjoner. Videre analyse med lysspredning viste at molekylvekt og gyrasjonsradius av xantan løst i både rent vann og DMSO var uavhengig av temperatur mellom 20 to 50°C. Denne observasjonen indikerer at orden-uorden transisjoner ikke forekommer. Videre hadde xantan løst i DMSO tilsynelatende høyere molekylvekt og gyrsjonsradius, sammenlignet med de samme prøvene løst i vann. Ettersom uordnet xantan ville ha hatt lavere molekylvekt og gyrasjonsradius, indikerer disse observasjonene at xantan ikke er uordnet i DMSO.

Table of Contents

List of Figures

List of Tables

Abbreviations

AFM	Atomic force microscopy
APD	Avalanche photo diode
Cadoxen	Cadmium dihydroxide
CD	Circular dichroism
DLS	Dynamic light scattering
DMSO	Dimethyl sulfoxide
DP	Degree of polymerisation
DS	Degree of substitution
Glc	Glucose
GlcA	Glucuronic acid
HPLC	High performance liquid chromatography
IBT	Department of Biotechnology and Food Science
IRIS	International Research Institute Stavanger
LS	Light scattering
L-CPL	Left handed-circularly polarised light
MALS	Multi-angle light scattering
Man	Mannose
MHS	Mark-Houwink-Sakaruda

MQ	Milli-Q
MWCO	Molecular weight cut off
MX	Marianne xanthan
MX_1	Marianne xanthan, run through Star Burst Mini 1 time in a solution of 0.5 M $MgSO_4$
MX_{10}	Marianne xanthan, run through Star Burst Mini 10 times in a solution of 0.5 M $MgSO_4$
NMR	Nuclear magnetic resonance
NTNU	Norwegian University of Science and Technology
PEM	Photo-elastic modulator
RI	Refractive index
RU	Repeating unit
R-CPL	Right handed-circularly polarised light
SEC	Size exclusion chromatography
SLS	Static light scattering
XCD	Kelzan XCD from CP Kelco

List of Symbols

Symbol	Explanation	Unit
α	Detected optical rotation	°
Γ	Decay rate	s^{-1}
γ_p	Proton gyromagnetic ratio	-
$\dot{\gamma}$	Shear rate	s^{-1}
δ	Chemical shift	ppm
ε	Detected ellipticity by CD	°
η	Shear viscosity	Pa s
η_r	Relative viscosity	-
η_{sp}	Specific viscosity	-
η_0	Shear viscosity of pure solvent	Pa s
θ	Scattering angle	°
λ	Wavelength of incoming light	nm
λ_0	Wavelength in vacuum	nm
μ	Magnetic moment	$J\ T^{-1}$
μ_0	Dynamic viscosity of pure solvent	Pa s
ν	Resonance frequency	Hz
π	Mathematical constant	-
ρ	Shape parameter from light scattering	-
τ	Shear stress	Pa
τ'	Correlation time	s
A	Area	m^2
A^*	DLS parameters and constants	-

Symbol	Explanation	Unit
A_2	Second virial constant	mol mL g^{-2}
a	Shape parameter RMS-conformation plot	-
B	Magnetic field	T
b	Shape parameter from MHS equation	-
c	Mass concentration of polymers	g L^{-1}
D	Diffusion coefficient	m^2 s^{-1}
$Đ_M$	Molar mass dispersity	-
E	Energy	J
E^*	Correction term for calculation of Hagenbach Correction Time	-
F	Force	N
$F(R_H)$	Size distribution function	-
f_{DMSO}	Critical fraction of DMSO	-
$G(\Gamma)$	Decay distribution function	-
$g_1(\tau, q)$	Field correlation function	-
$g_2(\tau, q)$	Scattering intensity correlation function	-
H^*	Correction term for calculation of Hagenbach Correction Time	-
h	Planck's constant	J s^{-1}
I	Spin quantum number	-
I_i	Integral of peak i	-
I_0	Incoming light intensity	W m^{-2}
i_0	Intensity of radiated light	W m^{-2}
i_{soln}	Intensity of light radiated from solution	W m^{-2}
i_{solv}	Intensity of light radiated from solvent	W m^{-2}
i_{tol}	Intensity of light radiated from toluene	W m^{-2}

Symbol	Explanation	Unit
K	MHS constant	-
K^*	Optical constant	-
k_B	Boltzmann-constant	J K^{-1}
k'	Huggins' constant	g L^{-1}
L_c	Contour length	nm
l	Length	m
M	Molecular weight	g mol^{-1} (Da)
M_0	Molecular weight of monomer	g mol^{-1} (Da)
M_L	Mass per unit length	nm^{-1}
M_n	Number average molecular weight	g mol^{-1} (Da)
M_w	Weight average molecular weight	g mol^{-1} (Da)
M_z	Z-average molecular weight	g mol^{-1} (Da)
m	Magnetic quantum number	-
N_{Avo}	Avogadro's number	mol^{-1}
N_i	Number of molecules	-
n_0	Refractive index of solvent	-
n_i	Number of moles	-
P	Pressure	Pa
q	Persistence length	nm
q^*	Scattering vector module	cm^{-2}
R_θ	Rayleigh factor	cm^{-1}
R_G	Radius of gyration	nm
$R_{G,app}$	Apparent radius of gyration	nm
R_H	Hydrodynamic radius	nm

Symbol	Explanation	Unit
$R_{H,app}$	Apparent hydrodynamic radius	nm
R_{Tol}	Rayleigh factor of toluene	cm^{-1}
r	Radius of capillary viscometer	m
r^*	Instrument constant of SLS	m
T	Temperature	°C (K)
T_m	Melting temperature of xanthan	°C
t	Time / Hagenbach corrected flow-through time	s
t_H	Hagenbach Correction Time	s
t_m	Measured flow-through time	s
t_0	Hagenbach corrected flow-through time of pure solvent	s
u	Velocity	$m\ s^{-1}$
V	Volume	m^3
W_i	Weight fraction	-
w_i	Sample weight	g
X_i	Mole fraction	-
z	Position in the direction perpendicular to fluid flow	m
$[\eta]$	Intrinsic viscosity	$mL\ g^{-1}$
$[\alpha]$	Specific optical rotation	$m°\ cm^2\ g^{-1}$
$[\varepsilon]$	Specific ellipticity of CD	$m°\ cm^2\ g^{-1}$
$\frac{\partial n}{\partial c}$	Refractive index increment	$mL\ g^{-1}$
$\left(\frac{\partial n}{\partial c}\right)_\mu$	Refractive index increment with constant chemical potential	$mL\ g^{-1}$

1 Introduction

Xanthan is an extracellular polysaccharide produced by the bacterium *Xanthomonas campestris*. Due to its viscosifying properties, xanthan is widely used in food products, pharmaceuticals and detergents, whereas the oil and gas industry is currently investigating its use as a polymer for enhanced oil recovery [1, 2]. The viscosifying properties are partially caused by its native structure, which is widely accepted to be a double helix [3]. The helix does, however, dissociate upon heating under low ionic strength in aqueous solution or when the solvent is changed, a phenomenon referred to as order-disorder transitions [1, 4]. Order-disorder transitions cause structural alterations, which affects both behaviour and properties. Hence, much research has been put into understanding and characterising the changes, which are known to depend on temperature, the solvent conditions, type of solvent and the acetate and pyruvate content of the xanthan [1, 5-7].

The ordered and disordered states of xanthan have different characteristics, i.e. the radii of gyration (R_G), molecular weights (M) and intrinsic viscosity ($[\eta]$). These characteristics can be detected by light scattering, viscometry and by SEC-MALS with an on-line viscometry detector [1, 8, 9]. An increase in optical rotation or a decrease in ellipticity determined by circular dichroism (CD), are also reasonable indications of order-disorder transitions taking place. From the two latter methods, the critical melting temperature (T_m) where xanthan is 50% disordered, can also be determined [10]. Atomic force microscopy (AFM), on the other hand, allows for visual observation of the xanthan structure and thus, a potential disorder can be determined [4].

Chemical modification can improve the properties of xanthan and allow for new industrial applications. Chemical modification and analysis are, however, simpler to perform at lower molecular weight and solution viscosities. Thus, degradation is required. Mechanical degradation by sonication can be used to prepare xanthan fragments of lower molecular weight with an intact, ordered conformation [11, 12]. However, sonication may not be suited for industrial degradation due to low efficiency and high noise levels [13]. Instead, mechanical degradation by high shear forces might be applied, as it allows for a higher throughput per time [13, 14]. The high shear forces are, however, caused by a high gauge pressure, which ultimately causes high temperature. Hence, order-disorder transitions are likely to occur during degradation. Establishment of a protocol that maximises the preservation of the ordered

structure of xanthan could allow for mechanical degradation by high shear forces in an industrial scale and further, make chemical modification and other analyses more feasible.

Chemical modification can be performed on both the ordered and disordered states of xanthan. The reactivity of the disordered state might even be better, similar to that of denatured proteins [15]. At lower temperatures, T < 100°C, full conversion of the xanthan double helix into single strands has so far only been observed in cadmium dihydroxide (cadoxen), a degrading solvent commonly known to dissolve cellulose [16-18]. The disorder of xanthan found in cadoxen conflicts data obtained when in aqueous solution, where complete dissociation of the double helix only occurs at low ionic strength and high temperature. At these conditions, measurements and modifications are difficult to perform. Other solvents for the disordered state have not yet been described. However, in 2017, Fantou *et al.* published a CD spectrum of the acid form (H^+-form) of xanthan in dimethyl sulfoxide (DMSO), corresponding to the disordered state [19]. The CD spectrum is presented in Figure 1.1, together with spectra of other xanthan samples.

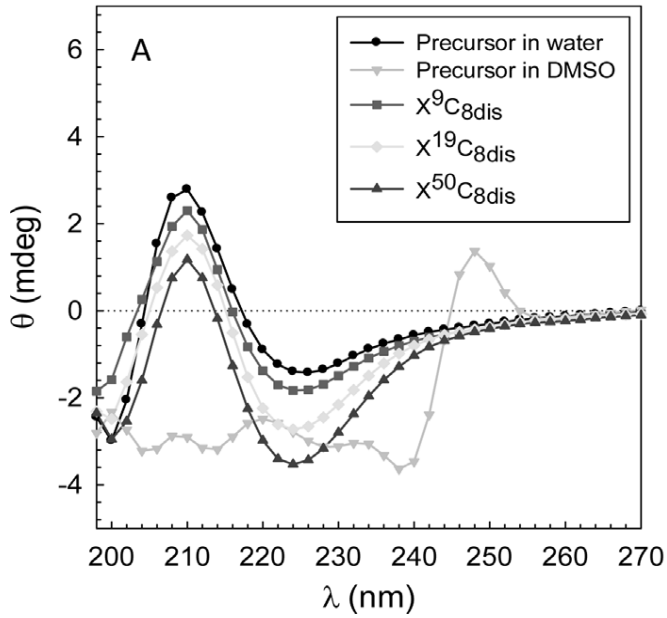

Figure 1.1: The CD spectrum of xanthan (precursor) in DMSO obtained by Fantou *et al* [19]. The spectrum shows that xanthan is in its disordered state in DMSO.

If xanthan is found to be disordered in DMSO, it opens a wide range of new possibilities, especially as DMSO is much less degrading compared to cadoxen [20].

2 The Scope of the Thesis

The overall aim of the thesis has been twofold:

1. Optimise the protocol for mechanical degradation of xanthan with high shear forces with maximum preservation of the double-stranded structure.
    a. Prepare fraction of xanthan with a range of molecular weights and investigate the conformation before and after desalting/purification.
    b. Remove acetate and pyruvate from xanthan samples for subsequent studies.
2. Verify and further investigate the possible disordered state for the acid form of xanthan in DMSO by the following methods:
    a. CD – to reproduce spectrum by Fantou *et al* [19] and determine the melting temperature (T_m) of the xanthan samples
    b. Optical rotation – to detect f_{DMSO}, i.e. the fraction of DMSO where a possible order-disorder transition occurs.
    c. Viscometry – to confirm f_{DMSO}
    d. Static light scattering – to evaluate the effect of DMSO on molecular weight and radius of gyration compared to water.
    e. Dynamic light scattering – to evaluate the effect of DMSO on hydrodynamic radius and the shape-parameter, both compared to water

Xanthan purified from a fermentation broth without formaldehyde (MX) obtained from the International Research Institute Stavanger (IRIS) was used to develop the protocol for mechanical degradation. The purification removes cells and unwanted proteins from the samples. 0614-3 XCD, a sample of KELZAN XCD xanthan sonicated for 30 minutes, was included in some analyses to serve as a positive control due to its known, optimal conformation.

3 Theory

This section elaborates more specifically on the structure and properties of xanthan, as well as explaining the degradation mechanism applied and the analytical tools used to evaluate and analyse the samples. Some of the theory sections have been adapted with modifications from the project thesis [21].

3.1 Xanthan

Xanthan is an extracellular polysaccharide produced by the plant pathogenic bacterium *Xanthomonas campestris*. The polysaccharide is composed of a pentasaccharide repeating unit (RU) that consists of two β-(1,4)-linked D-glucose (Glc) residues, forming the backbone, to which a trisaccharide side chain is attached. The first residue in the side chain is α-D-Mannose (α-Man) which is β-(1,3)-linked to alternating D-glucose residues in the backbone. D-glucuronic acid (GlcA) is α-(1,2)-linked to α-Man and is β-(1,4)-linked to the terminal residue, β-D-Mannose (β-Man) [1].

Acetate and pyruvate groups can be substituted to the RU of xanthan. The degree of substitution and substitution pattern depend on both the fermentation conditions and the strain used for xanthan production [22, 23]. Six different variations of the RUs are known to exist. The most abundant RU has O-6-acetylation of α-Man and pyruvate substitution on β-Man through diketal linkages on O-4 and O-6 [1, 24]. If this RU is present, approximately 90% of α-Man has found to be acetylated, and 30–50% of β-Man are substituted with pyruvate [25]. The second most abundant RU have O-6-acetylation on both α-Man and β-Man [24]. The structure of the most abundant RU of xanthan is given in Figure 3.1.

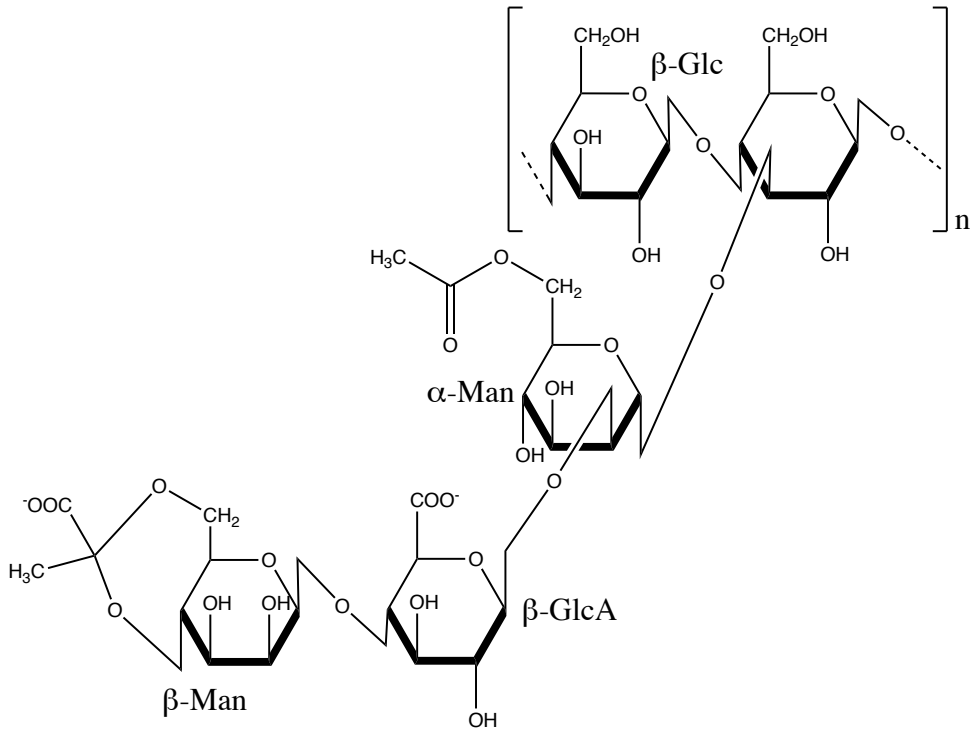

Figure 3.1: The most abundant pentasaccharide repeating unit (RU) of xanthan. α-Mannose (α-Man) is O-6 substituted with acetate and pyruvate is linked to β-Mannose (β-Man) via diketal linkages.

Xanthan is a double-stranded polysaccharide. The cellulose backbone of two strands lies back to back, stabilised by hydrogen-bonds with the trisaccharide chains pointing outwards [1, 3]. Its double helical structure has been confirmed by both electronic microscopic- and AFM-studies [3, 26]. The structure of xanthan visualised by AFM is presented in Figure 3.2, where the double- stranded coil and its splitting into single strands are shown by a curve and an arrow, respectively.

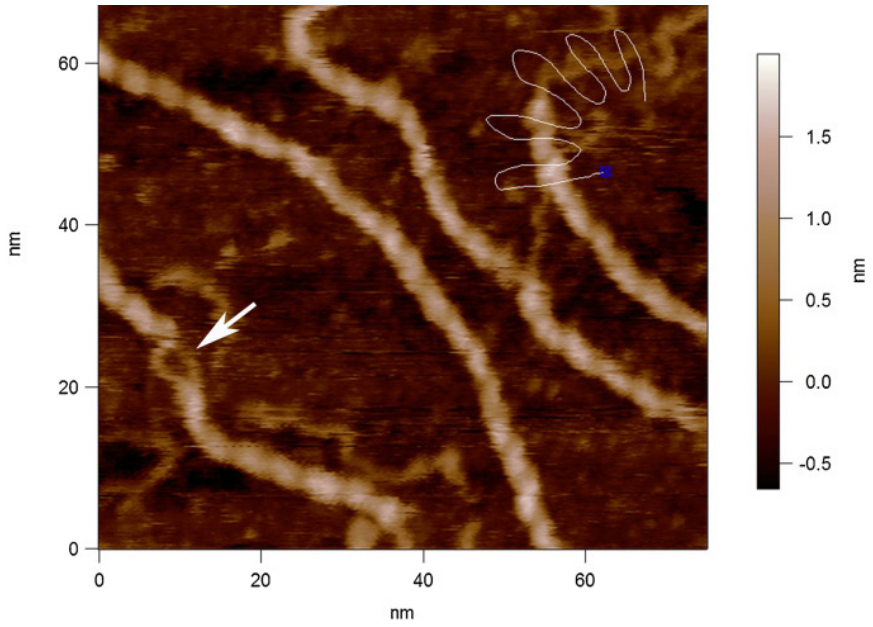

Figure 3.2: The double helical structure of xanthan visualised by AFM [3]. The curves show a helical region, while the arrow points at a region where unwinding has occurred, exposing single strands.

The double helical structure gives rise to properties sought by many industries, but also makes xanthan susceptible to thermal order-disorder transitions, which is further elaborated in section 3.1.2.

3.1.1 General Properties

Xanthan has a very high molecular weight, typically in the range from 10^6-10^7 Da [27]. The double helical structure makes xanthan one of the stiffest biopolymers known, with a persistence length of about 120 nm. It also gives rise to high salt tolerance and stability towards degradation agents. Xanthan makes even dilute solution very viscous compared to other polysaccharides at the same concentration, which makes it a suitable viscosifier in food, pharmaceuticals and other technical applications [1]. The viscosity does, however, exhibit different apparent viscosities at different shear rates. At low shear rates, the apparent viscosity is high compared to when high shear rates are applied, a concept defined as shear thinning. The shear thinning behaviour is illustrated in Figure 3.3.

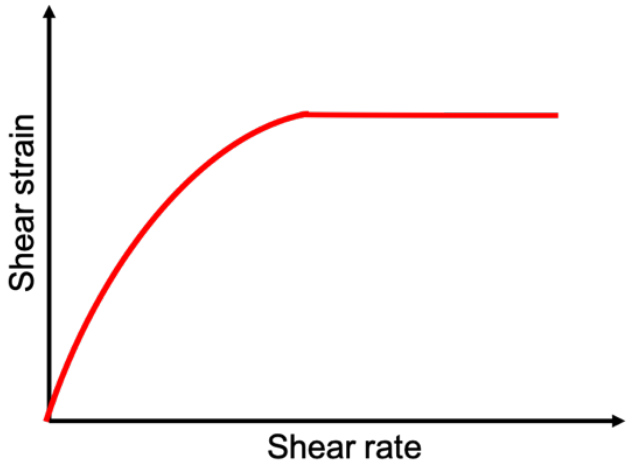

Figure 3.3: Shear thinning behaviour of a fluid with increasing shear rate.

The shear thinning property is typical for a non-Newtonian fluid, meaning that the behaviour becomes pseudo plastic for increasing shear rates [28]. The concept will be further elaborated in section 3.4.3, where viscometry is introduced.

3.1.2 Order-Disorder Transitions

Xanthan is susceptible to order-disorder transitions upon heating above a specific temperature or when the solvent conditions are changed [1, 6, 7]. The ordered state of xanthan is known as a stiff double helix, whereas the disordered state exposes single strands, which are more flexible and holds random coil properties [3, 26]. Disordered xanthan has reduced R_G, M and $[\eta]$ as well as increased sensitivity to both salt and depolymerisation by cellulases and chemicals, making it less favourable for industrial applications [1, 27]. The transition between order and disorder can be detected by numerous methods, among them chiroptical methods, light scattering and viscometry [8, 29].

3.1.2.1 Melting Temperature

From experimental data, it is possible to determine T_m, i.e. the temperature where xanthan is 50% disordered. Figure 3.4 illustrates how an order-disorder transition is detected by optical rotation and how T_m can be determined [1].

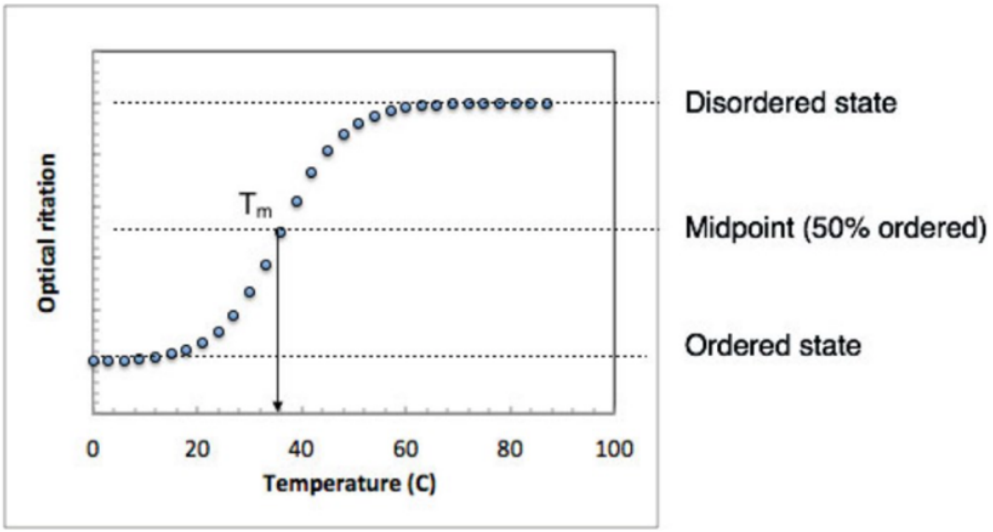

Figure 3.4: An example of an order-disorder transition curve of xanthan. The transition curve was determined by optical rotation, and the melting temperature (T_m) was determined from the curve [1].

The melting temperature is influenced by ionic strength and pyruvate- and acetate content [6, 8, 30]. High ionic strength favours the ordered helical structure and increases T_m [8]. The same relation is observed with increasing substitution of acetate [30]. A high content of pyruvate groups, on the other hand, decreases T_m [6]. It has also been shown that order-disordered transitions are dependent on the xanthan concentration, where a concentration of 10 mg/mL stabilises the double helical structure due to increased ionic strength caused by xanthan itself [31].

3.1.2.2 Renaturation Mechanisms

Thermal denaturation is almost entirely reversible. However, local transitions which cannot be recovered during renaturation might be introduced. The renaturation mechanism is suggested to depend on xanthan concentration, as well as ionic strength and temperature. In case of a concentration of xanthan < 1 mg/mL, the reformed double helical structure might be obtained with a hairpin loop of a single xanthan molecule. At higher concentrations, where a substantial part of the double helix is thought to be stabilised by the ionic strength from xanthan itself, renaturation occurs by different mechanisms [31]. The different renaturation mechanisms proposed are illustrated in Figure 3.5 [32].

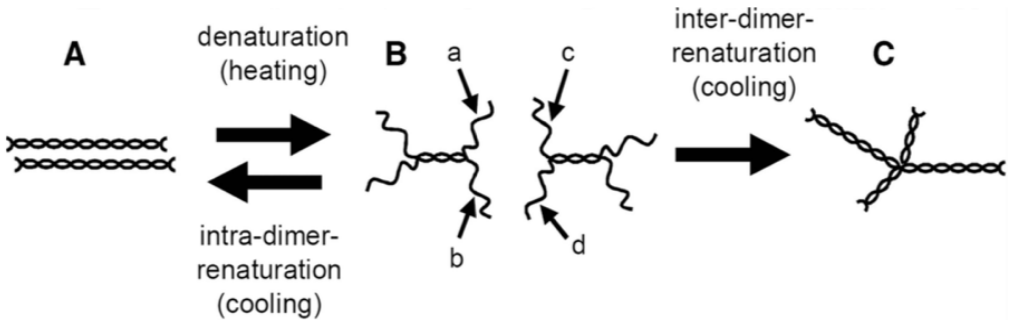

Figure 3.5: Schematic overview of denaturation and renaturation of xanthan under high concentrations. Intra-dimer renaturation is caused by aggregation of single- stranded ends on the same molecule. Inter-dimer renaturation takes place between ends of different molecules [32].

Upon heating, single-stranded ends may form, as shown in Figure 3.5B. When cooled, intra- and inter-dimer renaturation can take place. In case of intra-dimer renaturation, the ends on the same molecule, e.g. **a** and **b** in Figure 3.5B, aggregate, creating a molecule similar to the original. In case of inter-molecular dimer renaturation, ends of different polymer-chains, e.g. **b** and **d**, aggregate creating a molecule with more random conformation than the original, as illustrated in Figure 3.5C [32]. Both xanthan in its disordered conformation and inter-molecular renatured state will have a decreased persistence length, and thus altered properties compared to the original, ordered structure.

3.1.3 The Acid Form of Xanthan

Xanthan on the acid form (H^+-form) possess properties different from sodium xanthan. The double helical conformation is preserved; however, the structure becomes more flexible, and the persistence length decreases. The intrinsic viscosity and radius of gyration are also known to decrease around 20% compared to sodium xanthan in neutral, aqueous solution. The reduced radius of gyration and intrinsic viscosity for acidic xanthan compared to Na^+-xanthan is illustrated in Figure 3.6A and B, respectively [33].

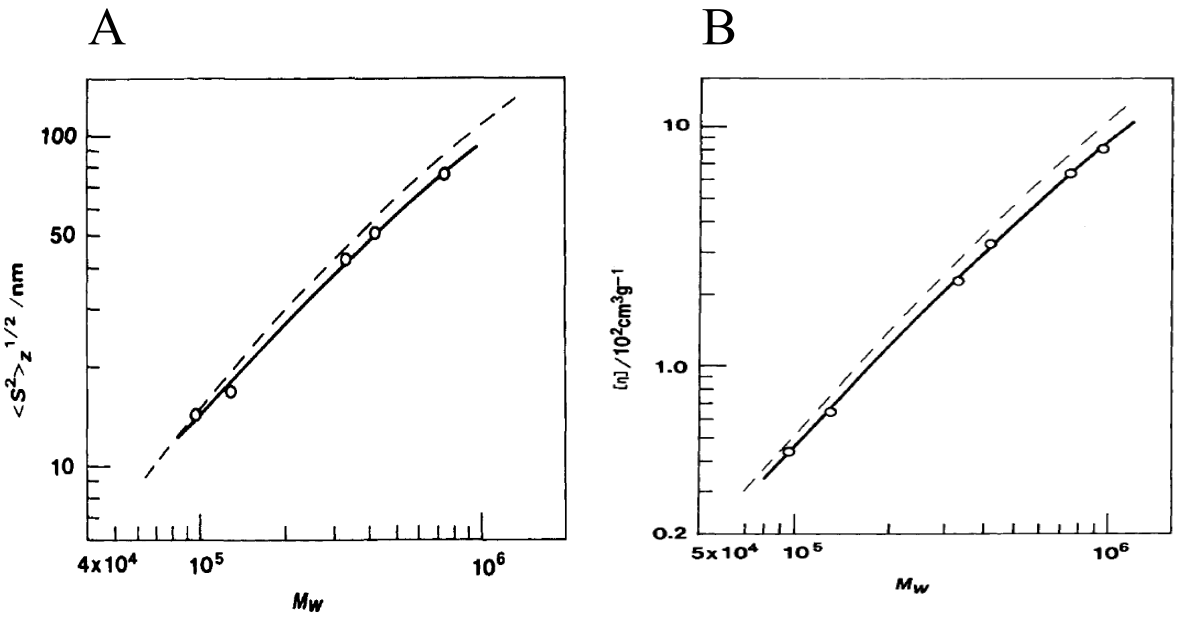

Figure 3.6: Molecular weight dependency of radius of gyration (A) and intrinsic viscosity (B) for Na^+-xanthan (dashed) and H^+-xanthan (circles) at 25°C [33].

Furthermore, xanthan on the acid form show increased stability at higher temperatures and thus have a higher T_m. The stability of H^+-xanthan as a function of temperature has previously been shown by optical rotation, where it was found that the optical rotation of acidic xanthan increases linearly with temperature. The sodium form followed a linear trend for lower temperatures before a sigmoidal shaped curve was observed, characteristic for order-disorder transitions (Figure 3.4). The stability of H^+-xanthan compared to Na^+-xanthan is reproduced in Figure 3.7 [34].

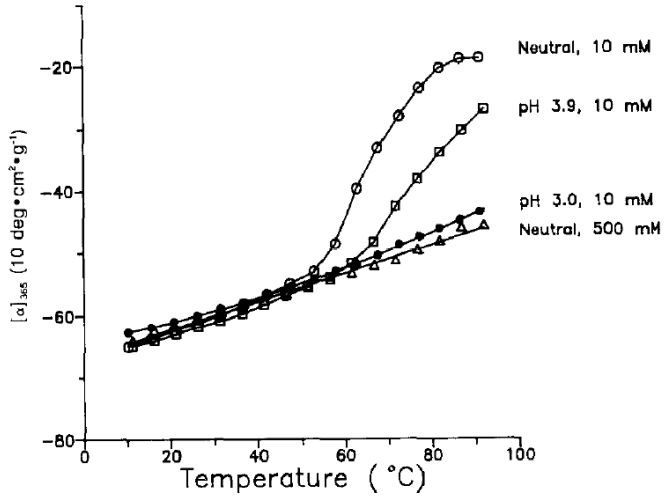

Figure 3.7: Temperature dependence of the specific optical rotation of xanthan [34]. The pH and NaCl concentration are denoted on the curve. The graph illustrates the stability of H^+-xanthan (pH 3) compared to Na^+-xanthan (Neutral) towards increasing temperature.

From Figure 3.7, it can be seen that the positive sigmoidal curve vanishes as pH is decreased from neutral to pH 3, leaving no order-disorder transition to occur in the measured temperature range: 10 to 90°C [34].

Furthermore, the acid form of xanthan becomes soluble in organic solvents such as DMSO also, due to the neutralisation of negative charges. Complete solubility has, however, been found to only occur after heating [19].

3.1.4 Acetate- and Pyruvate-Free Xanthan

The acetylation of α-Man and pyruvate substitution of β-Man influence the order-disorder transition, both T_m and the transition rate. Thus, to eliminate any effect of side chain chemistry, the acetyl- and pyruvate groups can be selectively removed by mild alkaline and acidic hydrolysis, respectively [35]. Xanthan without acetate and pyruvate substituents is known to have similar rheological properties as native xanthan, i.e. xanthan whose substituents has not been removed [36].

3.1.5 Macromolecular Characteristics

An overview of the molecular characteristics of xanthan in aqeous solution is summarised in Table 3.1 [37].

Table 3.1: Molecular characteristics of xanthan in aqueous solution [37].

Ordered state	
Double helix	
Molecular weight, M:	10^6-10^7 Da
Intrinsic viscosity, $[\eta]$:	3000-7000 mL/g
Persistence length, q:	70-120 nm
Mass per unit length, M_L:	Ca. 2000 nm^{-1}
Rigid rod-like due to high persistence length	
Stable towards degradation	
Solution properties insensitive towards variations in pH (3-10) and ionic strength	
Pseudoplastic/shear thinning behaviour	
Disordered state	
Helix split into single-stranded chains, completely or partially	
Random coil like	
Reduced stability towards degradation	
Less viscous solutions	

3.2 Molecular Weight Averages in Polymer Science

The molecular weight (M) of a homopolymer, i.e. a polymer whose monomers are all identical, could be determined from its monomer weight (M_0) and the degree of polymerisation (DP) as expressed in Equation (3-1) [1].

$$M = \mathrm{DP} \cdot M_0 \tag{3-1}$$

DP refers to the number of monomers residues forming the polymer. However, most polysaccharides, including xanthan, exhibit dispersity, meaning that a sample is a mixture of different chain lengths. The dispersity of a polymer sample makes it difficult to determine the exact molecular weight. Instead, the molecular weight distribution could be determined, where the relative amount of each chain length is assigned to a certain DP. The relative amount of each DP is usually expressed as weight fraction, W_i or mole fraction, X_i. The index, i, referrers to the specific DP [1].

From the molecular weight distribution of a polymer sample, the average molecular weight of the polymer could be determined. M_n is the number average molecular weight and is calculated the same way as arithmetic mean, as presented in Equation (3-2) [1, 38].

$$M_n = \frac{\sum_i N_i M_i}{\sum_i N_i} = \frac{\sum_i n_i M_i}{\sum_i n_i} = \sum_i X_i M_i \tag{3-2}$$

N_i is the number of molecules having DP i, while M_i and n_i are the molecular mass and number of moles at this specific DP. In M_n, all molecules are treated equally, irrespective of their shape or size [38]. Another molecular weight average is M_w, the weight average molecular weight. M_w is obtained by replacing the mole fractions in Equation (3-2) with weight fractions. The resulting expression is presented in Equation (3-3) [1, 39].

$$M_w = \frac{\sum_i N_i M_i^2}{\sum_i N_i M_i} = \frac{\sum_i w_i M_i}{\sum_i w_i} = \sum_i W_i M_i \tag{3-3}$$

Here, w_i refers to the weight of the fraction having DP i. A third molecular weight average is the z-average molecular weight, denoted M_z. M_z is a higher-degree average, more sensitive to

the largest molecules present in the sample compared to M_n and M_w. M_z is expressed as in Equation (3-4) [40].

$$M_z = \frac{\sum_i N_i M_i^3}{\sum_i N_i M_i^2} = \frac{\sum_i w_i M_i^2}{\sum_i w_i M_i} \quad \textbf{(3-4)}$$

In total, the different molecular weight averages provide valuable information. The ratio between M_w and M_n is known as the molar mass dispersity, $Đ_M$, expressed in Equation (3-5) [41].

$$Đ_M = \frac{M_w}{M_n} \quad \textbf{(3-5)}$$

For polymers degraded randomly, $Đ_M$ = 2. However, in case of a monodisperse sample, $Đ_M$ approaches 1. Thus, for a monodisperse sample $M_n = M_w = M_z$ [1, 41].

3.3 The Shape of Polymers in Solution

Polymers in solution can roughly be categorized into three groups: Solid spheres, rigid rods and random coils [1]. The shape of a biopolymer can be determined by the relation between the radius of gyration, R_G, and the molecular weight, M, of the polymer, presented in Equation (3-6) [1].

$$R_G = KM^a \quad \textbf{(3-6)}$$

In Equation (3-6), K is a constant and a is the shape parameter for the polymer, which takes different values depending on the shape. Similarly, the shape could also be determined by a relation between the intrinsic viscosity, $[\eta]$, and M. This relation is known as the Mark-Houwink-Sakurada (MHS) equation and is expressed in Equation (3-7), where the shape parameter is denoted b [1].

$$[\eta] = KM^b \quad \textbf{(3-7)}$$

The molecular weight in Equation (3-6) and (3-7) could be any of the molecular weight averages presented in section 3.2. Consequently, R_G and $[\eta]$ can also be number, weight or z-averages, depending on the weight average used.

The specific values for the shape parameters of the different shapes in Equation (3-6) and (3-7) are presented in Table 3.2. A good solvent is assumed for the random coil [1, 42].

Table 3.2: The expected shape parameters for biopolymers in solution [1, 42].

	a	b
Rigid rod	1	1.8
Random coil	0.6	0.8
Solid sphere	0.33	0

The persistence length (q) is a quantifying measure of the stiffness of a polymer, linked to both the worm-like chain model and Kuhn length, l_k. However, for the scope of this thesis, the models and proof behind its connection to the persistence length will not be explained further. The persistence length is linked to both R_G and M through Equation (3-8). Thus, it can be determined from experimental data [1].

$$R_G^2 = \frac{qM}{3M_L} - q^2 + \frac{1q^3M_L}{M}\left[1 - \frac{qM_L}{M}\left(1 - e^{-\left(\frac{M}{qM_L}\right)}\right)\right] \quad \textbf{(3-8)}$$

M_L is the mass per unit length, defined as in Equation (3-9), through M and the contour length, L_c.

$$M_L = \frac{M}{L_c} \quad \textbf{(3-9)}$$

The persistence length is determined by fitting of Equation (3-8) to experimental R_G and M_w data, systematically varying the unknown parameters. An illustration of the procedure of finding q is presented in Figure 3.8 [11]. Here, various values of q are tested. q = 120 nm have the best fit to the R_G and M_w data, and hence the persistence length of xanthan was determined to be 120 nm.

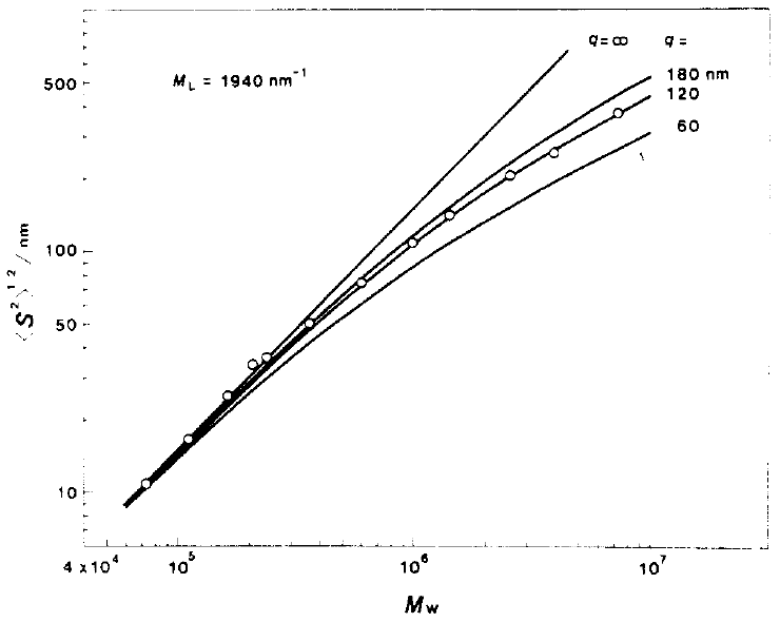

Figure 3.8: An illustration of the procedure finding the persistence length (q) for xanthan [11].

3.4 Experimental Theory

3.4.1 Mechanical Degradation by High Shear Forces

Polymers with a rod-like conformation can be degraded by forcing a solution to flow at a high shear rate [13]. Wet Jet Mill Star Burst Mini, referred to as Star Burst Mini is a wet-type micronizing device to which high gauge pressure, up to 245 MPa, can be applied in order to obtain high shear rates. When the desired pressure is set, the polymer solution is extracted into a chamber, where a plunger acts and pressurises the solution. The solution is further sent through a narrow nozzle, which increases the shear rate before it collides with a ceramic ball [14]. The collision causes larger particles to be dispersed into smaller, more homogeneous particles [43]. An overview of the events taking place inside the Star Burst Mini is presented in Figure 3.9 [14].

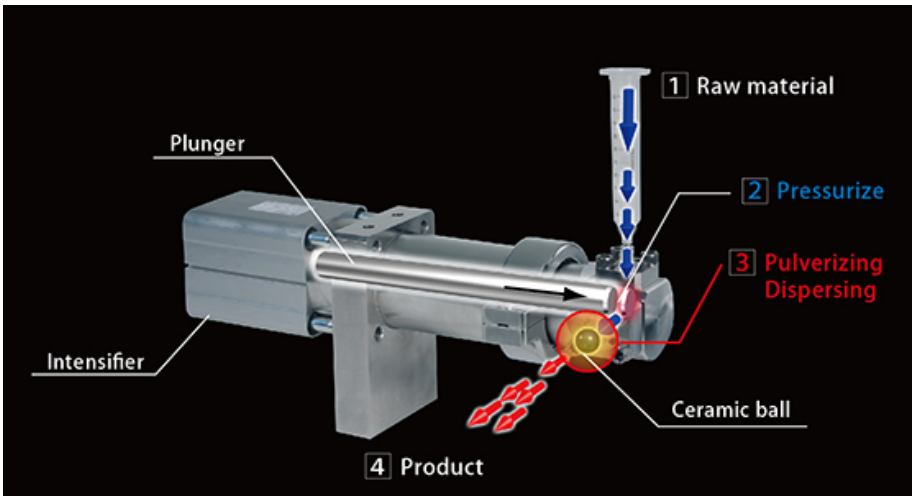

Figure 3.9: Overview of the mechanism of high shear rate degradation using Star Burst Mini. A plunger pressurises the raw material solution, which is further sent through a nozzle to increase the shear rate. The pressurised solution collides with a ceramic ball, which causes dispersion of larger particles [14].

When a high shear rate is applied to a polymer, it degrades similar to when ultrasonic treatment is applied, i.e. the glucosidic bonds in the main chain are broken, whereas carbon-carbon bonds within sugars monomers, hydrogen bonding and other glucosidic bonds are left intact [13]. An illustration of the mechanism of mechanical degradation and its effect on xanthan is presented in Figure 3.10.

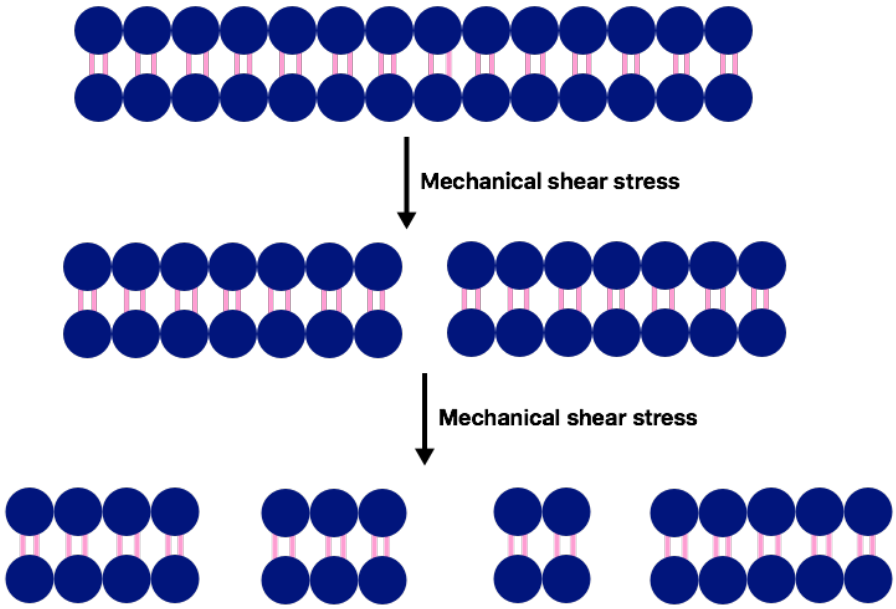

Figure 3.10: A simplified overview of the effect of high shear stress on the xanthan double strand. The double strand is fragmented into smaller fractions, however, the hydrogen bonds between the double strands are kept intact.

3.4.2 ^{1}H-NMR Spectroscopy

NMR spectroscopy is a non-destructive technique for identifying and analysing the structure of organic compounds. The method is based on the magnetic nuclear properties of the atomic nuclei. The atomic nuclei have a positive charge and a nuclear spin. The nuclear spin has an associated spin quantum number (I) which depends on the nuclear mass and atomic number. The I implies that each isotope of an element has different spin quantum numbers. However, only nuclei with a non-zero spin number, such as ^{1}H, ^{13}C and ^{15}N are active in NMR-spectroscopy and yield a signal [44].

In ^{1}H-NMR, the signals from the ^{1}H isotope are measured. This isotope has a nuclear spin quantum number, $I = \frac{1}{2}$, and thus the proton has two different alignments in the presence of a static magnetic field: $+\frac{1}{2}$ and $-\frac{1}{2}$. The different alignments are defined as the magnetic quantum number (m) [44]. When the charged nucleus spins, it generates a magnetic field with a magnetic moment (μ) [1]. μ can be linked to m through Equation (3-10) [44].

$$\mu = \frac{\gamma_p h}{2\pi} m \qquad \textbf{(3-10)}$$

In Equation (3-10), h is Planck's constant and γ_p is the proton gyromagnetic ratio. When a magnetic field, B is applied to a dipole such as the ^{1}H nucleus, the magnetic moment of the protons will interact with the external magnetic field. The result is that some of the spins will align parallel to the external field, while some become anti-parallel. Parallel spins have lower energy compared to those oriented anti-parallel. The difference in energy (ΔE) between the two levels is given in Equation (3-11) [44].

$$\Delta E = \frac{\gamma_p h B}{2\pi} m \qquad \textbf{(3-11)}$$

Spins can be transferred to a higher energy level by applying electromagnetic irradiation with frequency (ν) corresponding to ΔE, as shown in Equation (3-12) [1].

$$\Delta E = \frac{h}{\nu} \quad \textbf{(3-12)}$$

Combining Equation (3-11) and (3-12) yields an expression for the characteristic resonance frequency for each nucleus, presented in Equation (3-13).

$$\nu = \frac{\gamma_p B}{2\pi} \quad \textbf{(3-13)}$$

Depending on their chemical environment, different protons have different resonance frequencies due to nuclear shielding of the external magnetic field, caused by electrons in the molecule. The shielding leads to a chemical shift (δ) defined in Equation (3-14) [44].

$$\delta = \frac{\nu_{sample} - \nu_{standard}}{\nu_{spectrometer}} \cdot 10^6 \text{ ppm} \quad \textbf{(3-14)}$$

ν_{sample}, $\nu_{standard}$ and $\nu_{spectrometer}$ is the resonance frequency for the sample, a known standard and the spectrometer used, respectively. The chemical shift causes different signals in an NMR-spectrum and makes it possible to distinguish the different parts of the molecule from each other. Integration of a signal reveals the relative number of protons responsible for the particular signal [44].

The ^{1}H-NMR Spectrum of Xanthan

Xanthan can be O-acetylated, and pyruvate substituted depending on both the *Xanthomonas* stain and fermentation conditions. The substituents can be distinguished and quantified in a ^{1}H-NMR spectrum at elevated temperatures, i.e. > 80°C [45]. The signals arise from the CH_3-group found on both substituents; however, due to different chemical environment, their chemical shift is different. The pyruvate signal is located around 1.5 ppm, while the acetate signal is found close to 2.2 ppm. If free acetate is present in the sample, i.e. if acetate groups have been cleaved off, a signal is expected around 2.0 ppm. A signal at approximately 5.2 ppm originates from the anomeric proton at α-Man, the inner mannose unit in the xanthan side chain. This signal is referred to as H-1 α-Man. A typical ^{1}H-NMR-spectrum of xanthan is presented in Figure 3.11 [46].

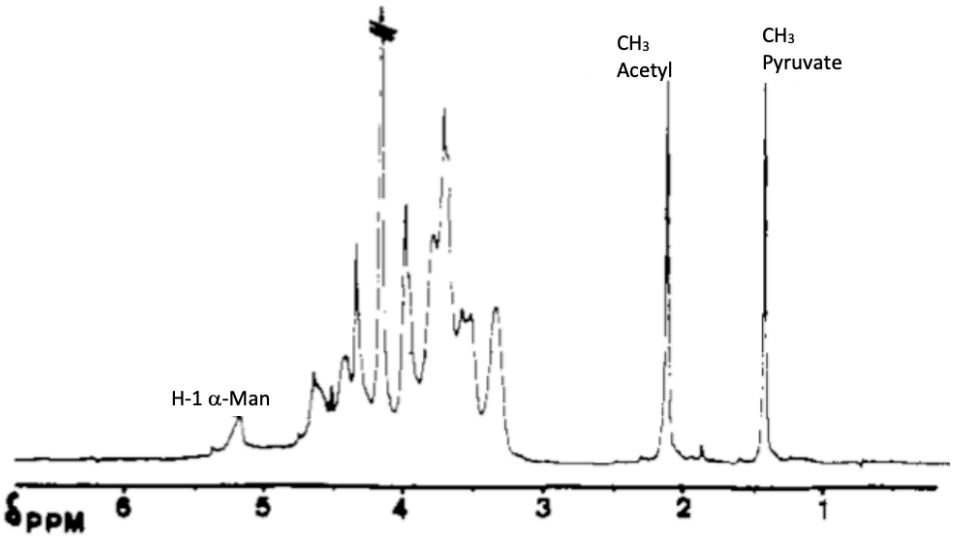

Figure 3.11: A typical ^{1}H-NMR spectrum of xanthan. The pyruvate signal is expected to occur around 1.5 ppm, while the acetate signal is expected close to 2.2 ppm. The reference signal, H-1 α-Man should be located around 5.2 ppm [46].

The signals of acetyl, pyruvate and α-Man can be integrated, and thus it is possible to quantify the number of substituents relative to the number of RUs, known as the degree of substitution (DS). H-1 α-Man is present of all xanthan samples, and thus serve as a reference signal representing the number of RUs. The general relation for the DS of substituent i is presented in Equation (3-15) [47].

$$\mathrm{DS}_i = \frac{n_i}{n_{\mathrm{RU}}} = \frac{N_{H,ref} \cdot I_i}{N_{H,i} \cdot I_{ref}} \qquad \textbf{(3-15)}$$

In Equation (3-15), n_i and n_{RU} is the molar quantity of substituent i and repeating units, respectively. N_H represents the number of hydrogen responsible for the signal, and I is the integral of the signal. The subscripts "ref" and "i" refer to the reference signal, i.e. the H-1 α-Man signal, and substituent i, respectively. As the signal from both acetyl and pyruvate derive from three hydrogens (CH_3), their integrals need to be divided by three to only represent one hydrogen.

Pyruvate can only be substituted on β-Man and with only one β-Man per repeating unit, the maximal DS of pyruvate equals 1, indicating that all side chains of xanthan possess pyruvate. Acetylation can, on the other hand, occur at both α-Man and at β-Man (if no pyruvate group is present). Hence, the degree of acetate substitution can be higher than 1, maximum 2, depending on the DS of pyruvate.

3.4.3 Viscometry

Viscometry is a method used to determine the viscosity of a fluid. The viscosity of a fluid is defined as the resistance the fluid has towards deformation by shear stress or tensile stress. Shear viscosity, also known as dynamic viscosity, has the symbol η and is dependent on both shear stress (τ) and shear rate ($\dot{\gamma}$). The relation between these variables is presented in Equation (3-16) [48].

$$\eta = \frac{\tau}{\dot{\gamma}} = \frac{\frac{F}{A}}{\frac{du}{dz}} \tag{3-16}$$

The shear viscosity and thus, Equation (3-16) can be explained in terms of a liquid flowing between two parallel plates, illustrated in Figure 3.12 [1].

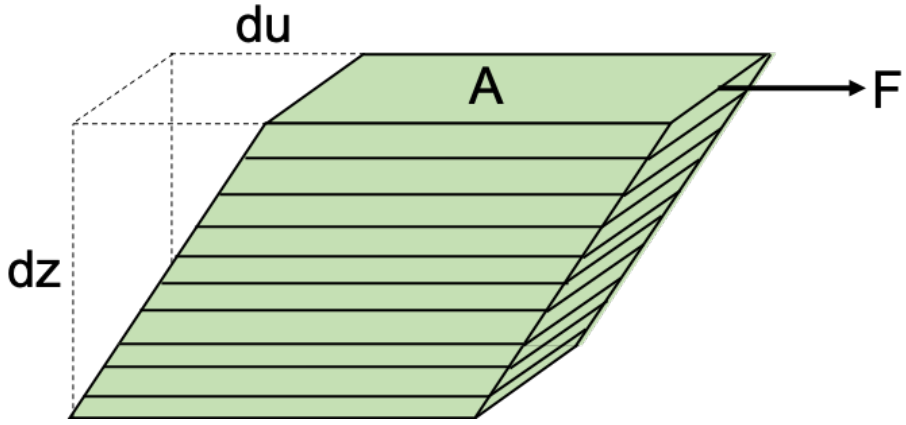

Figure 3.12: Flow between two vertical and parallel plates. A force, *F*, is applied to one of the plates with the area, *A*, causing a shear stress *τ*. The liquid between the plates move with flow gradient, $\frac{du}{dz}$, which represents the change in velocity, *du,* relative to the change in distance, *dz,* from the fixed, lower plate.

A force (F) is applied to one of the plates with area (A) causing a shear stress. The shear stress further causes the liquid between the plates to move with flow gradient ($\frac{du}{dz}$). To describe du and dz, laminar flow is considered, where the flowing liquid can be regarded as infinitely thin and parallel layers. Between the layers, F acts and creates a flow gradient, explaining the change in fluid velocity, du, relative to a distance dz from a fixed point on the lower and stationary plate [1].

From Equation (3-16), τ increase proportionally with $\dot{\gamma}$, a property specific for Newtonian fluids, indicating that the fluids internal resistance is independent of the force acting on the liquid [48]. For non-Newtonian fluids like xanthan in aqueous solutions, however, τ will not increase proportionally with $\dot{\gamma}$. Instead, increasing shear rate causes the growth rate of τ to decline. As a consequence, η will also decline for increased $\dot{\gamma}$ [49, 50]. The non-Newtonian behaviour of xanthan is caused by its rigid structure in ordered conformation, which tend to align more with the direction of flow as the shear rate increases [1].

Capillary viscometry is a type of viscometry, where the flow-through time in a capillary (t) is measured. The flow-through-time can be linked to viscosity through Hagen-Poiseuille's Law, Equation (3-17) [51].

$$\eta = \frac{\pi \Delta P r^4 t}{8 V l} \tag{3-17}$$

In Hagen-Poiseuille's Law, ΔP is the pressure difference over the capillary, whereas r and l is the capillary radius and length, respectively. V equals the volume of liquid that passes the capillary in time t. Hence, η is proportional to t [51]. However, the flow-model in Hagen-Poiseuille's Law is not ideal as it does not take into account pressure losses occurring at the in- and outflow of the capillary. As a consequence, the measured flow-through time (t_m) is greater than the t from Hagen-Poiseuille's Law. To account for the pressure losses, the Hagenbach Correction Time (t_H) is introduced. The relation between the t_H, t_m and t is presented in Equation (3-18) [52].

$$t = t_m - t_H \tag{3-18}$$

The Hagenbach Correction Time is dependent on the type of capillary viscometer. For funnel-shaped capillary ends, t_H is calculated as in Equation (3-21) [52].

$$t_H = \frac{E^*}{H^* t_m^2} \tag{3-19}$$

Here, E^* and K^* are correction terms stated at the operating instructions of the capillary viscometer or can be taken from relevant DIN standards [52].

Furthermore, the relative viscosity (η_r) and specific viscosity (η_{sp}) can be defined as in Equation (3-20) and (3-21), respectively [1].

$$\eta_r = \frac{\eta}{\eta_0} = \frac{t}{t_0} \tag{3-20}$$

$$\eta_{sp} = \frac{\eta - \eta_0}{\eta_0} = \eta_r - 1 = \frac{t}{t_0} - 1 \tag{3-21}$$

η_0 is proportional to t_0, which represent the viscosity and flow-through-time of pure solvent, respectively [1].

Both the relative- and specific viscosity are dependent on the mass concentration (c) of dissolved polymers in the solution. The parameter $\frac{\eta_{sp}}{c}$ is referred to as the reduced viscosity. The limiting value of $\frac{\eta_{sp}}{c}$ when c approaches zero is further defined as the intrinsic viscosity ($[\eta]$) as described in Equation (3-22). The intrinsic viscosity is an exclusive property for a specific polymer/solvent system.

$$[\eta] = \lim_{c \to 0} \left(\frac{\eta_{sp}}{c} \right) \tag{3-22}$$

When capillary viscometry is performed, a given volume of solution with known polymer concentration is transferred to a viscometer, similar to the illustration in Figure 3.13 [51].

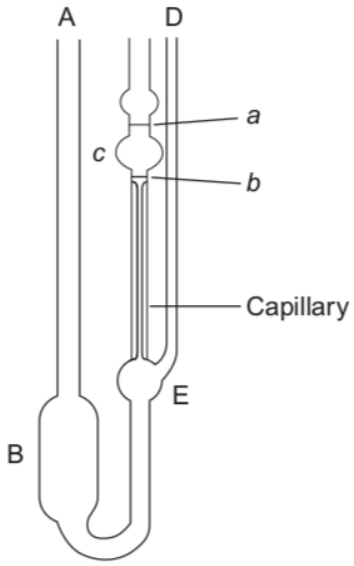

Figure 3.13: Illustration of a viscometer commonly used in capillary viscometry [51].

The viscometer is placed into a water bath, controlled at the desired temperature. The solution is pushed up from **B** to bulb **c** by applying a pressure on stem **A** as column **D** is sealed. The pressure is then released, and the flow-through time is measured as the time for the solution meniscus to pass from mark **a** to mark **b** in bulb **c** above the capillary, as illustrated in Figure 3.13. The flow-through time is measured for a set of known polymer concentrations, as well as for pure solvent. The obtained data can then be used to find η_r, η_{sp} and thus $[\eta]$ for the given polymer. One approach to obtain $[\eta]$ is the Huggins' equation, where $\frac{\eta_{sp}}{c}$ is plotted against the concentration, yielding $[\eta]$ as intercept. The slope is $k'[\eta]^2$, where k' is Huggins' constant. Huggins' equation is described in Equation (3-23) [51, 53].

$$\frac{\eta_{sp}}{c} = [\eta] + k'[\eta]^2 c \qquad \textbf{(3-23)}$$

3.4.4 Chiroptical methods

Chiroptical methods are based on chiral molecules possibility to affect the plane of linear polarised light, i.e. the light whose oscillations are confined to a single plane [54, 55]. All polarised light states can be described as the sum of two linearly polarised states, perpendicular to each other, usually referred to as vertically and horizontally polarised light. Circularly polarised light (CPL) arises when one of the polarised states is out of phase with the other by a quarter-wave. Chiroptical methods include both optical rotation and circular dichroism (CD)

spectroscopy, both in which will be described further in Section 3.4.4.1 and 3.4.4.2, respectively [55].

3.4.4.1 Optical Rotation

The physical basis of optical rotation, also referred to as optical activity, is the different refraction index of left (L) and right (R) CPL measured at a given wavelength [56]. The difference between L- and R-CPL is presented in Figure 3.14 [55].

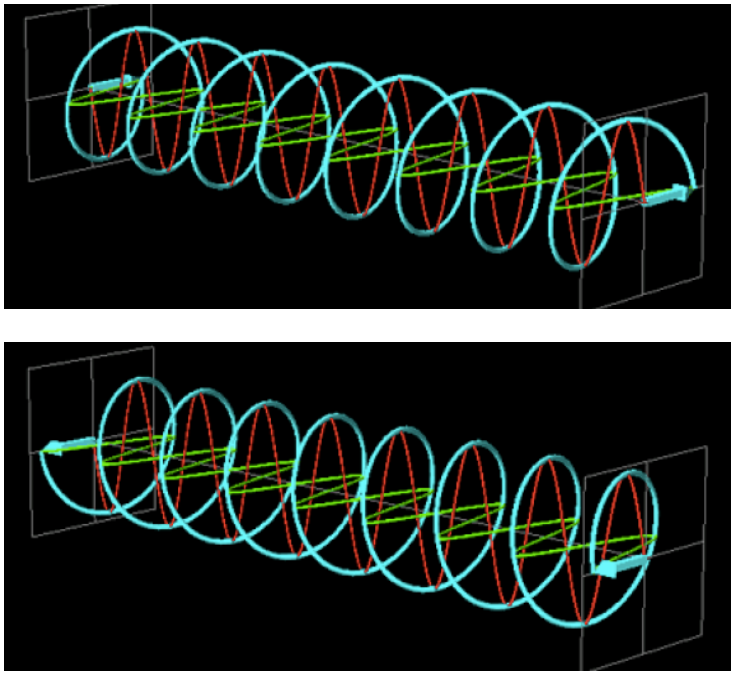

Figure 3.14: An illustration of the difference between left- (top) and right- (bottom) circularly polarised light (CPL). The blue lines correspond to CPL, whereas red and green waves represents vertically and horizontally plane polarised light, respectively [55].

At the given wavelength, the optical rotation is the resultant of both short- and long-range Cotton effects [57]. A drawback of optical rotation is, however, that the various optically active groups of a compound generally have overlapping bands, which are difficult to separate [54].

A polarimeter measures the optical rotation of a sample, which represent the extent, measured in degrees, to which the sample rotates the plane-polarised light irradiating the sample. In the polarimeter, light of a specified wavelength (λ) passes through a polariser, which only allows light aligned in one direction to pass. The aligned light further transmits through the sample to be studied. If the sample contains chiral molecules, the light will rotate and further be detected. The detected optical rotation is referred to as α. An illustration of a polarimeter is presented in Figure 3.15.

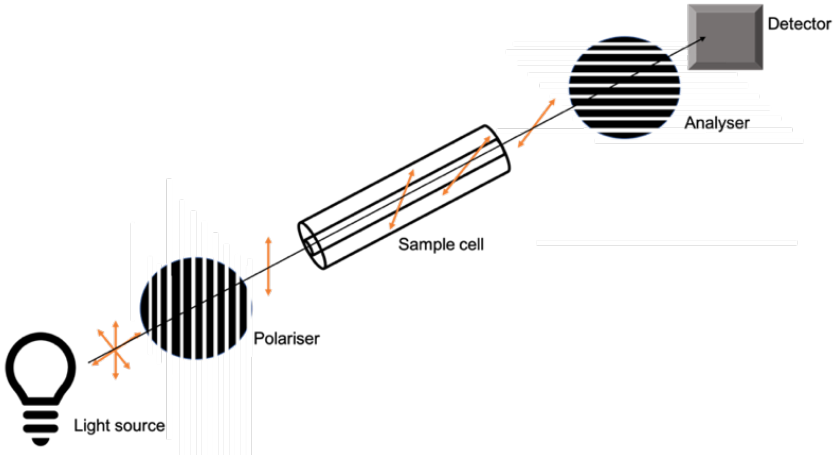

Figure 3.15: An overview of the set-up and mechanism of a polarimeter used to determine the optical rotation of a chiral molecule.

The optical rotation of a sample is dependent on the concentration, solvent, the temperature and wavelength used, as well as the path length, i.e. the sample cell length. In order to be able to compare the optical rotation of different samples, α is standardised. This standardisation is referred to as specific rotation ($[\alpha]_\lambda^T$) and is calculated by applying Equation (3-24) [58]. The superscript and subscript refer to the temperature and the wavelength of the measurements, respectively.

$$[\alpha]_\lambda^T = \frac{\alpha}{l \cdot c} \tag{3-24}$$

In Equation (3-24), l is the optical path length, whereas c represent the sample concentration.

3.4.4.2 Circular Dichroism Spectroscopy

The physical basis of circular dichroism (CD) is the difference in the absorption of L- and R-CPL. CD spectroscopy is a technique where the ellipticity of molecules is measured over a range of wavelengths and is a widely used technique to study chiral molecules of all types and sizes. A primary use is analysis of macromolecules sensitive to its environment, temperature or pH [55]. Oppositely to optical rotation, which provides signals in a wide range of wavelengths, CD only provides a signal around an optically active absorption band. This is an advantage when analysing samples of diverse optical activity. A disadvantage is, on the other hand, that it can be applied only in the absorption range of the samples studied [54].

The circular dichroism spectrum of a sample is measured using a circular dichroism spectrometer, equipped with a piezoelectric photo-elastic modulator (PEM) cemented to a block of fused silica. When measurements are performed, the piezoelectric PEM oscillates at its resonance frequency and induces alternating stress in the silica element, which further turns the silica into a dynamic quarter-wave, turning the vertical and horizontal linearly polarised light into L-CPL and R-CPL at the given drive frequency. A light detector on the other side of the sample position detects the difference in the intensity between the two circular polarisations. If the sample studied is found to be chiral, one of the two states of the CPL will be absorbed to a greater extent than the other, and thus the ellipticity at the specific wavelength is obtained. If the L-CPL is absorbed to a greater extent than the right, the ellipticity would be positive. Oppositely, the ellipticity becomes negative if R-CPL is absorbed to a greater extent [55].

CD measurements are also standardised by applying Equation (3-24). However, instead of $[\alpha]$, the measured values is usually referred to as $[\varepsilon]$ for ellipticity [55].

3.4.5 Light Scattering

Light scattering (LS) is a tool for characterising various molecules as it provides the z-average radius of gyration (R_G) hydrodynamic radius (R_H) and the weight average molecular weight (M_w) The physical basis of LS is interactions between light and electrons in the irradiated molecule. Light contains an oscillating electric field, which in contact with a macromolecule creates an oscillating dipole moment around the molecule. The oscillating dipole is a source of electromagnetic radiation which will re-radiate or emit light in all direction. The intensity of emitted light (i_0) is dependent on both the intensity of incoming light (I_0) and the polarizability of the macromolecule [1]. An illustration of the scattering of light is presented in Figure 3.16.

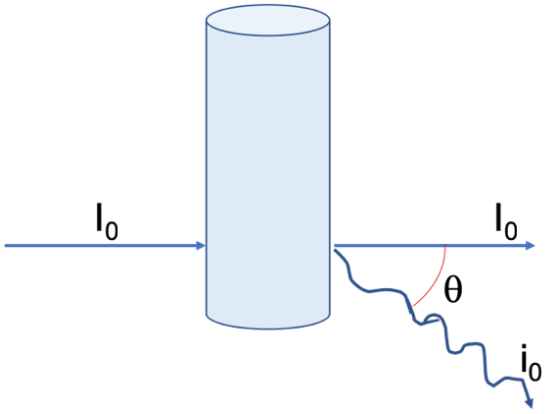

Figure 3.16: The scattering of light (i_0) relative to the incoming light (I_0) at scattering angle θ.

LS can further be divided into dynamic light scattering (DLS) and static light scattering (SLS). SLS refers to the analysis of the absolute mean scattered intensity of the reradiated light as a function of the scattering angle, whereas DLS analyses the time-fluctuations of the scattered intensity at a specific scattering angle [59]. DLS and SLS are further elaborated in Section 3.4.5.1 and 3.4.5.2, respectively.

3.4.5.1 Dynamic Light Scattering

In DLS, the motion of particles is investigated by analysing the correlation of intensity fluctuations. When light irradiates small particles, the light scatters in all directions; a phenomenon called Rayleigh scattering. The scattering does, however, fluctuate over time, due to Brownian motion of particles, causing the distance between scatters in the solution to change with time constantly. The change in scattering can either be constructive or destructive interference by surrounding particles, providing an intensity of the fluctuations, known as the scattering intensity correlation function, $g_2(\tau', q^*)$. For an ergodic system $g_2(\tau', q^*)$ can be written in terms of the field correlation function $g_1(\tau', q^*)$ through the Siegert relation, expressed in Equation (3-25) [60, 61].

$$g_2(q^*, \tau') = \frac{\langle I(q^*, t) I(q^*, t + \tau') \rangle_t}{\langle I(q^*, t) \rangle^2} = 1 + \beta |g_1(q^*, \tau')|^2 \quad \textbf{(3-25)}$$

In Equation (3-25), $I(q^*, t)$ represent the net scattered light intensity at time t, τ' is the correlation time, whereas β is an intercept from the Siegert correlation between the scattering intensity correlation function and the electric field correlation function. The scattering vector module (q^*), i.e. the vector between the scattered and the incoming light, can further be expressed through the refractive index of the solution solvent (n_0), the laser wavelength in vacuum (λ_0) and the scattering angle (θ) as expressed in Equation (3-26) [62].

$$q^* = \frac{4\pi n_0}{\lambda_0} \sin\left(\frac{\theta}{2}\right) \quad \textbf{(3-26)}$$

For diffusive, strictly monodisperse suspensions, $g_1(\tau, q^*)$ decays exponentially with τ', as expressed in Equation (3-28) [60, 61].

$$g_1(q^*, \tau') = \exp(-\Gamma\tau') \quad \textbf{(3-27)}$$

From the definition of the decay rate (Γ), presented in Equation (3-28), the diffusion coefficient (D) of solutes can be determined [61].

$$\Gamma = q^{*2} D \quad \textbf{(3-28)}$$

D is further used to determine the hydrodynamic volume (R_H) of the molecules in solution, by applying the Stokes-Einstein relation, Equation (3-29) [61, 62].

$$R_H = \frac{k_B T}{6\pi\mu_0 D} = \frac{k_B T q^{*2}}{6\pi\mu_0 \Gamma} \quad \textbf{(3-29)}$$

In the Stokes-Einstein relation, k_B is the Boltzmann-constant, T is the temperature and μ_0 is the viscosity of the solvent.

In the case of analysing polydisperse solutions, the decay rate can no longer be represented as an exponential function. As a consequence, $g_1(q^*, \tau')$ must be expressed by an integral over the decay rate, instead of a function of a single exponential. If Rayleigh scattering, i.e. when $q^* R_H \leq \frac{1}{2}$, $g_1(q^*, \tau')$ can be expressed as in Equation (3-30) [63].

$$g_1(q^*, \tau') = \int_0^\infty d\Gamma G(\Gamma) \exp(-\Gamma\tau') \quad \textbf{(3-30)}$$

$G(\Gamma)$ corresponds to the decay distribution function, which is normalised so that $\int_0^\infty G(\Gamma) \mathrm{d}\Gamma = 1$. The CONTIN computer program has a built-in algorithm for solving Equation (3-30), which allows for a good approximation of the actual size distribution in the solution analysed. In short, the CONTIN program analyses of the field correlation function, acquired during DLS analysis by assuming initial parameters. The algorithm is run so that optimal regulation parameters can be obtained. These are further used to rerun the algorithm, obtaining a Γ which is substituted into Equation (3-29) to attain an expression for R_H, which is further substituted into Equation (3-30). The resulting equation is presented in Equation (3-31), where A^* includes all the constants and parameters from Equation (3-29) [63].

$$g_1(q^*,\tau') = \int_0^\infty F(R_H)\exp\left(-\frac{A^*\tau'}{R_H}\right)dR_H \qquad \textbf{(3-31)}$$

$F(R_H) = (A^*/R_H^2)G(\Gamma)$ equals the size distribution function, which is also normalised so that $\int_0^\infty F(R_H)dR_H = 1$ [63].

Then DLS is performed, a laser beam passes through a beam splitter, allowing for the monitor diode to detect the reference intensity of the light. The light further impinges a glass cuvette immersed in a toluene or xylene bath set at the desired temperature, which also avoids reflexes around the sample under investigation. The light scattered from the sample is detected at an angle θ by an avalanche photodiode (APD), which logs the signal on a computer [60, 61]. A high-quality DLS analysis should always be performed at several scattering angles. The proposed setup of DLS is illustrated in Figure 3.17 [60].

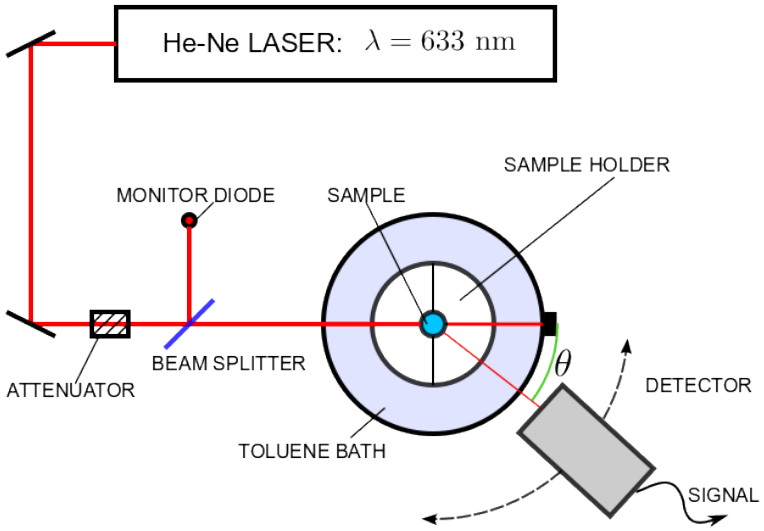

Figure 3.17: A proposed setup of dynamic light scattering (DLS) at 633 nm [60].

3.4.5.2 Static Light Scattering

Static light scattering (SLS) is an optical technique where the intensity of the scattered light in dependence of the scattering angle is measured to obtain information on the molecule studied, i.e. the radius of gyration and molecular weight [64]. For a disperse sample, the z-average radius of gyration ($R_{G,z}$) and weight average molecular weight (M_w) are determined.

The main quantities influencing the SLS intensity are the concentration, molecular weight and the size of the particles in solution. For a large number of "small" macromolecules moving independently in solution, the total scattering intensity equals the sum of intensities from each particle. In the category "small", R_G should be less than $\frac{\lambda}{20}$, where λ is the wavelength of the incoming light. However, for larger macromolecules, i.e. molecules with R_G between $\frac{\lambda}{20}$ and $\frac{\lambda}{2}$, independent and interfering scattering elements need to be considered. The interference from such particles is strongly dependent on the scattering angle, θ and is always destructive, except at $\theta = 0°$. Nevertheless, for lower concentrations, it is possible to condense all the dependencies into Equation (3-32) [1, 65].

$$\frac{K^* c}{R_\theta} = \left(1 + \frac{16\pi^2 R_{G,z}^2}{3\lambda^2} \sin^2\left(\frac{\theta}{2}\right)\right)\left(\frac{1}{M_w} + 2A_2 c\right) \qquad \textbf{(3-32)}$$

In Equation (3-32), A_2-term is a thermodynamic parameter reflecting the interactions between polymer and solvent in the solution and c is the concentration of polymer. Note that a concentration series needs to be analysed by light scattering in order for A_2 to be determined. The optical constant, K^*, of Equation (3-32) can be expressed as in Equation (3-33) for vertically polarized light [1].

$$K^* = \frac{4\pi^2 n_0^2 \left(\frac{\partial n}{\partial c}\right)_\mu^2}{N_{Avo}\lambda_0^4} \qquad \textbf{(3-33)}$$

In Equation (3-33), n_0 represents the refractive index of the sample solvent, and N_{Avo} is Avogadro's number. $\left(\frac{\partial n}{\partial c}\right)_\mu$ is the differential refractive index increment of the polymer at constant chemical potential [1, 66].

The Rayleigh ratio (R_θ) is introduced as a quantity independent of the experimental setup and is used to normalise the scattering intensity. Normalisation is needed to overcome scattering from the solvent due to thermally induced density fluctuations in the liquid. Also, the surface of the sample cuvette unavoidably scatters some light [65]. R_θ is expressed as in Equation (3-34).

$$R_\theta = \frac{i_{soln} - i_{solv}}{i_{tol}} \left(\frac{n_o}{n_{tol}}\right)^2 R_{tol} \quad \textbf{(3-34)}$$

i_{soln}, i_{solv} and i_{tol} refer to the scattering intensity of the solution analysed, its solvent and the calibration substance toluene, respectively. R_{tol} and n_{tol} is the Rayleigh ratio and refractive index of pure toluene, respectively [67].

Analysis of SLS data and thus solving Equation (3-32) can be done by applying one out of many analysis models. However, for larger molecules, the Berry fit model is recommended and will be described further. In the Berry fit model, $\sqrt{\frac{K^* c}{R_\theta}}$ is plotted against $\sin^2\left(\frac{\theta}{2}\right)$ so that M_w and $R_{G,z}$ can be determined from the intercept and slope, respectively [68].

If only one concentration is analysed by light scattering, A_2 cannot be determined, and thus have to be assumed. Calculations without assuming A_2, due to negligible concentration, results in apparent M_w and $R_{G,z}$, referred to as $M_{w,app}$ and $R_{G,z,app}$, respectively.

3.4.6 Differential Refractometry

In order to perform calculations on light scattering data, the differential refractive index increment at constant chemical potential $\left(\left(\frac{\partial n}{\partial c}\right)_\mu\right)$ has to be known. Determination of $\left(\frac{\partial n}{\partial c}\right)_\mu$ can be done through differential refractometry, a method that allows for measurement precision up to $\pm\ 3 \cdot 10^{-6}$ [69]. The basis of differential refractometry is the difference in refractive index between the sample studied and the sample solvent [70].

When differential refractometry is performed, a sample of known concentration and its solvents is transferred to different compartments of a cell designed for differential refractometry determination [69]. An illustration of a cell used for measurements in a Schulz-Cantow refractometer is presented in Figure 3.18.

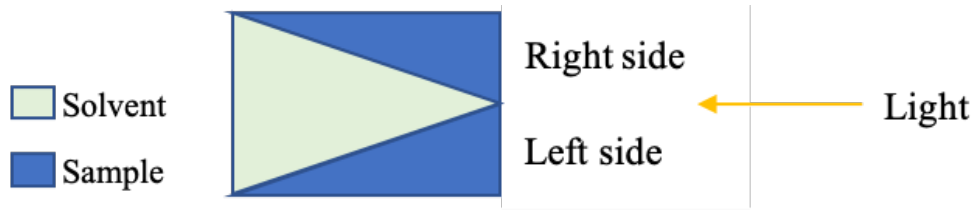

Figure 3.18: A top view of the cell used for differential refractive index increment measurements in a Schulz-Cantow differential refractometer. The sample is filled in two compartments, and measurements are performed on the left- and right-hand side, with the opposite side, covered.

Light is immersed through a filter of known wavelength before it impinges upon a slit and forms a slit image which is transmitted down a blackened light tube, where it passes through the cell and is reflected by a mirror. The mirror-image is sent back down the tube before it strikes a new mirror, which reflects the light downward by 90°. The light further impinges a circuit, to which two oppositely polarised photoelectric cells are mounted with a gap between them. A micrometre screw, which controls the position of the circuit, is further rotated until the illumination is acknowledged by an attached voltmeter [71]. The micrometre screw is further rotated until its arrow stops increasing, i.e. when the maximum voltage is observed. The screw is then rotated back until the voltmeter shows half of the maximum voltage and the number of the micrometre screw is read off. Numbers are also noted for ± 10 µA of half of maximum voltage, from both sides of the peak the electrical circuit causes. The average of each parallel is furthermore calculated, and thus represents the centre of the peak. The curve and the sampling points are illustrated in Figure 3.19.

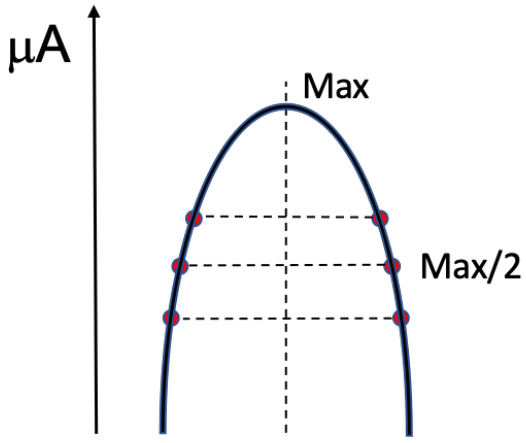

Figure 3.19: An illustration of the voltage peak arising from differential refractometry. Measurements are made at half of the maximum voltage ± 10 µA at both sides of the peak, and the average between each parallel is calculated. The average thus represents the centre of the peak.

Measurements should be performed on both the left- and right-hand side of the sample cell, covering the opposite side for both the solvent and the sample. Equation (3-35) is further applied to determine the distance (ΔD) between pure solvent ($n_{solvent}$) and the sample (n_{sample}) measured at both the left- and right-hand side (n_l and n_r respectively).

$$\Delta D = (n_r - n_l)_{sample} - (n_r - n_l)_{solvent} \quad \textbf{(3-35)}$$

ΔD is multiplied with a constant of the filter of known wavelength to provide the difference in refractive index between the sample and pure solvent (Δn). $\left(\frac{\partial n}{\partial c}\right)_\mu$ is obtained as the slope of Δn measurements performed at different concentrations, plotted against the respective concentration. If a filter of the light scattering wavelength is not available, measurements should be performed at a minimum of three other wavelengths and extra- or interpolated towards the desired wavelength.

3.4.7 SEC-MALS

SEC-MALS is an analytical tool that combines size-exclusion chromatography (SEC) with on-line multi-angle light scattering (MALS). It is a commonly used method to determine the different molecular weight averages and the molecular weight distribution, as well as the different averages radius of gyration for a polymer [1]. A SEC-MALS system consists of one or more size-exclusion chromatography columns, usually in a high-performance liquid chromatography (HPLC) system, which fractionates solvated polymer molecules according to their hydrodynamic volume and thus molecular weight [72]. Each eluted volume from the SEC-column runs through a concentration sensitive detector, either a refractive index (RI)- or a UV-detector. A light scattering detector is connected in series to the concentration detector and monitors scattering at up to 18 angles simultaneously [1]. A typical set-up for SEC-MALS is illustrated in Figure 3.20 [73].

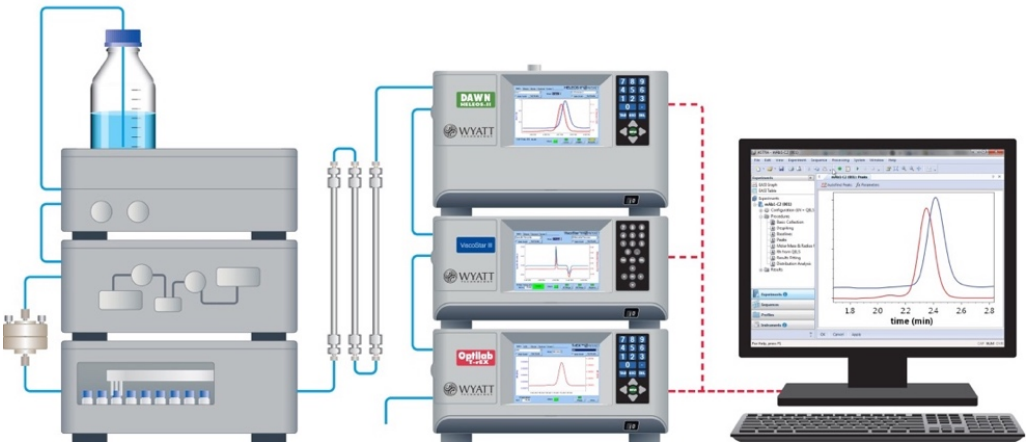

Figure 3.20: A basic set-up for SEC-MALS.

The separation mechanism of SEC is based on hydrodynamic volume. The stationary phase of the column is a porous material and separation is a result of the solute molecules passively diffusing into the pores [72]. Molecules that are larger than the pores will not, or to a lower degree diffuse in and out of the pores and thus be eluted first. Smaller molecules will be retained in the stationary phase for a longer time. The retention time in the column separates the molecules from largest to smallest. The mechanism of MALS is identical to SLS (section 3.4.5.2) however, the detector monitors up to 18 angles simultaneously [1].

When performing SEC-MALS, data is collected in a matrix for 1000-5000 elution volumes and c, M and R_G are determined for each of these. The result is the molecular weight distribution and the distribution of R_G, which can be used to calculate various averages and generate conformation plots to evaluate chain stiffness and thus conformation. A_2, on the other hand, has to be known when performing SEC-MALS analyses [1].

In addition to a RI- or UV-detector, an on-line viscosity detector can be added to SEC-MALS set-up. The method is then referred to as SEC-MALS-VISC. A viscosity detector uses the principles of capillary viscometry and determines the pressure difference over a capillary. As the concentration is known from the RI- or UV-detector, $\frac{\eta_{sp}}{c}$ can be calculated from each elution slice and thus $[\eta]$ can be calculated using Huggins' equation, Equation (3-23). This method does, however, require knowledge of Huggins' constant unless the concentration is low so that $k'[\eta]^2 c \ll [\eta]$. Then $[\eta] \approx \frac{\eta_{sp}}{c}$ [1].

Data-Processing in ASTRA

After performing SEC-MALS or SEC-MALS-VISC, the collected data can be analysed by the data program ASTRA. In general, ASTRA solves Equation (3-32) for each elution slice, which is assumed to be monodisperse. Under the parameter “Fit method/model", a regression model is chosen, allowing for optimal fit of the angular dependency, extrapolated towards zero angle. R_G and M can be determined from the slope and the intercept, respectively [68]. In the work of this thesis, the Berry fit model, described in Section 3.4.5.2, was applied. Once R_G and M of each monodispersed elution slice are determined, ASTRA calculates all the molecular weight averages by applying Equation (3-2) to (3-4).

4 Materials and Methods

4.1 Xanthan Samples

Measurements and analyses were performed on purified xanthan (MX) and Kelzan XCD (XCD). XCD is a commercial product by CP Kelco and is dried fermentation broth in a powder form. MX is xanthan purified from a fermentation broth without formaldehyde, purchased from IRIS (research institute), November 2016. The purification of MX had been performed by Marianne Øksnes Dalheim (IBT, NTNU Trondheim, 2016). In short, the fermentation broth was diluted 1:25 using 10 mM NaCl solution. The diluted solution was centrifuged, followed by rinsing of the supernatant by filtration. A two-step filtration was performed using filters of pore size 1.6 μm followed by 0.7 μm. Optical density was measured at a wavelength of 600 nm, using Milli-Q (MQ) water as a blank in order to estimate the bacterial cell concentration. Xanthan was precipitated by addition of solid NaCl to a concentration of 0.1 M NaCl, followed by addition of isopropanol to a final concentration of 60 v/v%. The precipitate was collected by a glass rod and washed two times using 80 v/v% isopropanol followed by one time using 100 v/v% isopropanol before it was left to dry in a heating cabinet at 37°C. The MX was further stored at room temperature.

4.1.1 Preparation of 0614-3 XCD: Sonication

The XCD used is referred to as 0614-3 XCD and had previously been prepared by Ina Beate Jenssen during her master thesis work (IBT, NTNU Trondheim 2013/2014). The powdered XCD had been dissolved in MQ-water and sonicated for 30 minutes, before centrifugation, filtration and dialysis against $NaNO_3$/EDTA at pH 7 took place. The final sample was freeze-dried and further stored cold in a freezer [12]. The 0614-3 XCD showed MHS- and RMS-conformation plots in good accordance with published data and was thus included as a reference for the MX samples.

To prepare 0614-3 XCD on the H^+-form, the original sample was dissolved in MQ-water to a final concentration of 5 mg/mL. The sample was left at stirring until completely dissolved, minimum overnight. The sample was further dialysed against MQ-water adjusted to pH 3 using HCl at room temperature, using Spectra/Por membrane tubing with a molecular weight cut off (MWCO) of 12-14 kDa. The membranes were soaked in MQ-water for 10-20 minutes and washed with distilled water 2 times before the samples were introduced. Five shifts of acidic

water were performed; two of them were overnight. The acidic dialysis was followed by dialysis against MQ-water to a conductivity below 2 μS was observed.

The DS of acetate and pyruvate of 0614-3 XCD had previously been determined to be 0.58 and 0.85, respectively, by Christian Holmvik (IBT, NTNU Trondheim 2017/2018) [47].

4.1.2 Preparation of MX_1 and MX_{10}: Mechanical degradation

In preparation of mechanical degradation, MX was dissolved in MQ-water to a concentration of 5 mg/mL and stirred in room temperature until dissolved, minimum overnight. When dissolved, MQ-water was added to a concentration of 2 mg/mL MX, before the sample was diluted 1:1 with 1 M $MgSO_4$, obtaining a final concentration of 1 mg/mL MX, 0.5 M $MgSO_4$. The ionic strength during mechanical degradation was determined based on results from the specialisation project in the autumn of 2018 [21].

Mechanical degradation was performed using Star Burst Mini. The Star Burst Mini was warmed up and washed with approximately 500 mL MQ water at 100 MPa following the procedure described in Wet Jet Mill Star Burst HJP-25001CE Instruction manual. The operational pressure of was set to 220 MPa, based on results from the master thesis of Christian Holmvik (IBT, NTNU Trondheim 2017/2018) [47]. After the first round, 50% of the sample was separated from the rest and stored cold. This fraction is further referred to as MX_1. The remaining part was further run through Star Burst Mini ten times, including sufficient cooling on ice between each run, in order to prevent overheating of the xanthan and thus unwanted dissociation of the double helices. The fraction of the original MX sample run through Star Burst Mini ten times is referred to as MX_{10}. The separation into two fractions after one run through Star Burst Mini was done to obtain samples of various molecular weight.

After degradation, both samples with MX_1 and MX_{10} were up-concentrated to about 2 mg/mL MX using a Büchi rotary evaporator at 35°C, in order to obtain volumes more suitable for dialysis. MX_1 and MX_{10} were further split into approximately three equal portions, in order to be able to prepare different salt-forms of xanthan. All portions were first dialysed against MQ-water at room temperature using Spectra/Por membrane tubing with an MWCO of 12-14 kDa in order to remove most of $MgSO_4$. The membranes were soaked in MQ-water for 10-20 minutes and washed with distilled water 2 times before the samples were introduced. The water was changed every three hours, followed by one night. After dialysis against pure MQ-water,

one portion of both the MX_1 and MX_{10} samples were dialysed against MQ-water adjusted to pH 3 with HCl in order to obtain H^+-xanthan. To obtain Na^+-xanthan, the second portion where dialysed against 0.05 M NaCl. The HCl and NaCl dialysis was performed five times, including two nights, before the portions were dialysed against MQ-water until a conductivity below 2 μS was observed. The last portion of both MX_1 and MX_{10} were only dialysed towards MQ-water until a conductivity below 2 μS was observed, yielding Mg^{2+}-xanthan. The samples were further freeze-dried to obtain a dry MX, further stored at room temperature. In total, six samples were prepared: H^+-MX_1 and MX_{10}, Na^+-MX_1 and MX_{10} and Mg^{2+}-MX_1 and MX_{10}.free

In the project thesis, the DS of acetate and pyruvate of MX were determined to be 0.52 and 0.70, respectively. These values are assumed to be valid for both MX_1 and MX_{10}, due to no observation of free acetate in neither of the ^{1}H-NMR spectra of MX [21].

4.1.3 Acetate- and Pyruvate-Free Xanthan

Removal of acetate and pyruvate of xanthan was performed after a procedure described by Christensen and Myhr [35]. In preparation of removal of substituents, Mg^{2+}-MX_1 and MX_{10} and 0614-3 XCD were dissolved in MQ-water to a concentration of 5 mg/mL and left at stirring at room temperature until dissolved, minimum overnight. To remove the pyruvate groups concentrated HCl was added to a final concentration of 0.1 M. The samples were bubbled with nitrogen gas for seven minutes each and placed in a water bath preheated to 80°C for 8 hours, based on unpublished kinetics calculations from prof. Christensen. This procedure has been shown to not to reduce the molecular weight much, i.e. only 1.1-1.5 times reduction [74]. The samples further cooled to room temperature and neutralised using 5 M NaOH.

To remove the acetate groups, 5 M NaOH was added to a final concentration of 0.025 M, resulting in a pH between 12 and 12.5. The samples were bubbled with nitrogen gas for seven minutes each and left at stirring in room temperature for 3 hours. The samples were then neutralised slowly, using 1 M HCl. In order to obtain acetate- and pyruvate-free MX, suitable for ^{1}H-NMR spectroscopy, one third was taken out from the original sample before adjusting to pH 3 using 5 M and 1 M HCl.

All samples were dialysed using Spectra/Por membrane tubing with an MWCO of 12-14 kDa. The acidic xanthan samples were dialysed against MQ-water adjusted to pH 3 with HCl at 4°C, where five shifts were performed. Two of the shifts were overnight. The acidic dialysis was

followed by dialysis against MQ-water at 4°C until a conductivity below 2 µS was observed. The dialysis bags with neutral xanthan samples were dialysed against MQ-water directly at 4°C. The water was changed two times each day until a conductivity below 2 µS was reached. The samples were further freeze-dried to obtain dry xanthan, further stored at room temperature.

4.2 Analysis of Acetate- and Pyruvate free Samples by ^{1}H-NMR Spectroscopy

To confirm the removal of acetate and pyruvate from the various xanthan samples, ^{1}H-NMR was conducted. In preparation of ^{1}H-NMR, acetate- and pyruvate-free xanthan samples were dissolved in D_2O to a concentration final concentration between 10 and 20 mg/mL, depending on their solution viscosity. The exact concentration of each sample is presented in Table 4.1.

Table 4.1: Concentration of the three different samples subjected to ^{1}H-NMR spectroscopy.

Sample name	Concentration [mg/mL]
MX_1, Ac+Pyr free	12.71
MX_{10}, Ac+Pyr free	19.27
0614-3 XCD, Ac+Pyr free	11.47

When dissolved, 500 µL of each sample were transferred to NMR tubes, and all samples were analysed with a Bruker Avance III HD at a frequency of 400 MHz, at 80°C.

4.3 Determination of Macromolecular Properties by SEC-MALS-VISC

Molecular weight distributions, intrinsic viscosity and thus conformation of both regular and acetate- and pyruvate-free MX_1, MX_{10} and 0614-3 XCD were investigated using SEC-MALS with connected viscometry detector. The set-up used, consisted of Agilent Technology 1260 Infinity and 1260 Infinity II HPLC columns, a Shodex RI-501 RI-detector connected to a Wyatt Technology DAWN Heleos-II multi-angle light scattering detector, further connected to a Wyatt Technology ViscoStar III viscometry detector.

All samples were first dissolved in MQ-water to a concentration of 2x the analysis concentration. When dissolved, the samples were diluted 1:1 with 2x buffer (0.3 M $NaNO_3$/0.02 M EDTA, pH 6), i.e. the mobile phase of the set-up. The measurements of MX_1 and 0614-3 XCD were performed at a final concentration of 0.5 mg/mL, due to high molecular weight. The MX_{10} samples had a final concentration of 1 mg/mL.

All samples were filtered using PALL 5 µm Acrodisc Syringe filters with Versapor membrane before transferred to SEC-MALS vials. Senior engineer at IBT, NTNU Trondheim Ann-Sissel T. Ulset ran all analyses. The differential refractive index increment and the second virial coefficient were set to $\frac{\partial n}{\partial c} = 0.15$ mL/g and $A_2 = 1.0 \cdot 10^{-4}$ mol·mL/g, respectively, based on literature [1].

4.4 Analysis of Acidic Xanthan in Water and DMSO

4.4.1 Circular Dichroism

Circular dichroism (CD) spectroscopy was applied to compare the behaviour of xanthan in DMSO compared to aqueous solvent and determine the melting temperature. In preparation for circular dichroism, all xanthan samples were dried overnight in a desiccator connected to a vacuum, before dissolved in two different solvents to a final concentration of 1 mg/mL, based on initial concentration analysis performed on MX_{10} samples. This analysis is presented in Appendix A. All samples were left at stirring overnight to allow for complete dissolution.

It has previously been reported by Fantou *et al.* that xanthan needs to be heated to be dissolved in DMSO [19]. However, all samples were completely dissolved in DMSO at room temperature overnight; thus, no heating was needed.

Before performing temperature scans at a fixed wavelength, a wavelength scan of all MX-samples dissolved in water was conducted. The scan was performed from 210-270 nm at both 20°C and 90°C using a Jasco J-720WO Spectropolarimeter. Lower wavelengths could not be applied due to equipment limitations. The quartz cell used had an optical wavelength of 0.5 cm at room temperature. The spectra obtained were averaged over 10 scans with a bandwidth of 1 nm. Based on the obtained spectra and discussion with prof. Sato, the temperature scans were performed at 215 nm, from 20-90°C. The bandwidth of the measurement was set to 1 nm and the rate of heating to 2 °C/min.

The ellipticity of the MQ-water was measured by the same approach, both wavelength and temperature scans were performed. These spectra serve as a baseline for further calculations.

Fantou *et al.* have previously studied xanthan in DMSO and water by CD, by performing a wavelength scan from 200-270 nm [19]. However, when performing a wavelength scan of DMSO from 210-270 nm in a 0.5 cm quartz cell, voltage > 1000 V was observed, indicating that light is not able to pass through the sample. To overcome this quartz cell of shorter optical wavelength, i.e. 0.2 cm, 0.1 cm and 0.1 mm was tested for DMSO measurements, but still high voltage was observed. CD of DMSO and xanthan in DMSO was thus not possible to perform.

4.4.2 Optical Rotation

Optical rotation was conducted in order to investigate a possible order-disorder transition as a function of w/w% DMSO. In preparation of optical rotation, solvents of 0-100 w/w% DMSO/MQ-water were prepared. 0614-3 XCD and MX_{10} were dissolved directly in each solvent, to a final concentration of 0.5 mg/mL and 1 mg/mL, respectively. All samples were left at shaking overnight for complete dissolution. No heating was needed for complete dissolution in DMSO.

Optical rotation was performed using an Anton Paar Modular Circular Polarimeter at 486 nm, using a 10 cm quartz cell at 25°C. Between each measurement, the quartz cell was washed two times with the solvent of the next sample, discarding the solvent used for washing. Optical cleaning of the samples was not performed to avoid adsorption of xanthan to the filter and thus change the concentration.

4.4.3 Capillary Viscometry

In preparation of capillary viscometry, the H^+-forms of MX_{10}, 0614-3 XCD and acetate- and pyruvate-free 0614-3 XCD were weighed out and dissolved directly in each solvent. The solvents prepared under preparation of optical rotation were used. The final analysis concentration of each sample is presented in Table 4.2.

Table 4.2: Overview of the samples analysed by capillary viscometry.

Sample name	Concentration [mg/mL]
H^+-0614-3 XCD H^+-0614-3 XCD, Ac+Pyr free	0.5
H^+-MX_{10}	1

All samples were left at shaking overnight to dissolve. No heating was needed to dissolve the samples in DMSO.

Capillary viscometry was performed at 25±0.01°C in a Julaba water bath with AVS measuring stand and Julaba MB temperature regulation. To determine the flow-through time of the solvents and the samples, t_0 and t, respectively, 4 mL of the samples were transferred into an AVS 33610/I Schott Geate viscometer. The flow-through times were measured five times for each sample. The viscometer was washed with 10 v/v% deconex, MQ-water and dried with acetone and compressed air before a new measurement was started. No filtration was performed in order to avoid adsorption of xanthan to the filter and thus change the concentration.

4.4.4 Light Scattering – DLS and SLS

LS was applied to obtain more information on the behaviour of xanthan in DMSO compared to in aqueous solution. In preparation of LS, all MX samples (MX_1, MX_{10} and acetate- and pyruvate-free MX_1 and MX_{10}) were dried in a desiccator connected to vacuum overnight before dissolved in MQ-water and pure DMSO to a final concentration of 1 mg/mL. The samples were left overnight to allow for complete dissolution. No heating was needed to dissolve the samples in DMSO.

The cylindrical light scattering cuvettes used were washed using 10% deconex, followed by extensive rinsing with water. Further, the cuvettes were washed with acetone under pressure at 79°C for four hours, covered in alumina foil which was washed the same way and dried in vacuum for 30 minutes.

All MX samples were optically cleaned by filtration before analysis. Due to limited availability, 0.8 μm DISMIC-25CS sterilised cellulose acetate syringe filters were used for the MX samples

dissolved in MQ-water, whereas the MX in DMSO samples were filtered using 5 μm Membrane Solution Nylon syringe filters. Pure MQ-water and DMSO were both filtered using 0.22 μm Membrane Solution PTFE syringe filters. Optical cleaning and transfer to light scattering cuvettes were performed in an inert atmosphere.

Simultaneous static and dynamic light scattering (SLS and DLS) measurements were performed using an ALV/SLS/DLS-5000 light scattering instrument equipped with an ALV-5000 multiple τ digital correlator. Vertically polarized light with the wavelength in vacuum λ_0 = 532 nm emitted from an Nd:YAG laser was used as the incident light. Before starting each measurement, the filled cuvette was immersed into the thermostatic xylene bath of the light scattering instrument for approximately five minutes in order to reach the set temperature of the xylene bath.

The light scattering system was calibrated using toluene as the reference substance. Before each MX-sample, the scattering intensity of toluene, i_{tol}, at each θ was measured. The scattering intensity and its time correlation measurements were initiated from low to high scattering angle θ. The measurements were made at θ = 30°-50° with step 5° and θ = 60°-135° with step 15°. The dark current of the light scattering system was also measured in order to correct the scattering intensities of toluene, the solvent water, and solutions. The scattering intensity of the sample solvents, MQ-water and DMSO were also measured at each θ. In total, 11 angles (40°-135°, step 5° and 15°) and four temperatures (20-50°C, step 10) were measured for each MX-sample, solvents and toluene.

Analysis of the SLS measurements was made by applying Equation (3-34) to determine the Rayleigh ratio for each sample. The Rayleigh ratio and refractive index of toluene were set to be $2.715 \cdot 10^{-5}$ cm^{-1} and 1.497 respectively, while the refractive index of DMSO and MQ-water were set to be 1.477 and 0.1335, respectively. Equation (3-32) was further solved by a Berry regression.

DLS measurements were analysed by the computer program CONTIN, providing the field correlation function and thus the final decay rate distribution function. The size distribution was analysed by the function “Regularized Fit Set-up”, using 150 data- and grid points. The minimum and maximum decay time were set to 0.0001 ms and 100 000 ms, respectively.

4.4.5 Differential Refractometry

In order to perform calculations on light scattering data, the refractive index increment, $\frac{\partial n}{\partial c}$, at the light scattering wavelength (532 nm) has to be known. The refractive index increment was measured using a Schulz-Cantow photoelectric differential refractometer. Before analysis, a concentration series of both MX_{10} and acetate- and pyruvate-free MX_{10} in MQ-water and DMSO were prepared and dissolved overnight. The MX_1 samples were not measured, based on discussions with prof. Sato, who stated that $\frac{\partial n}{\partial c}$ is not so dependent on molecular weight. Note that the samples were not dialysed against their solvent to obtain a constant chemical potential and thus $\left(\frac{\partial n}{\partial c}\right)_{\mu}$, in order to prevent absorption of water into DMSO [75].

The MX concentrations in MQ-water was 3, 5 and 10 mg/mL, whereas DMSO solutions were prepared to 1, 3 and 5 mg/mL. Before measurement, the samples and their solvent were optically cleaned using syringe filters of the same type as for light scattering experiments. Measurements were performed at 436, 488 and 546 nm at both 20°C and 50°C, six measurements at each wavelength and on both left and right side on the sample cell, as described in section 3.4.6 and Figure 3.18. Between each sample, the sample cell was washed thoroughly with distilled water, followed by acetone and drying in a vacuum.

5 Results and Discussion

The experimental work of this thesis involves a wide range of various samples and experimental pathways. Thus, an overview of the preparation of the samples and analytical methods is provided in Figure 5.1.

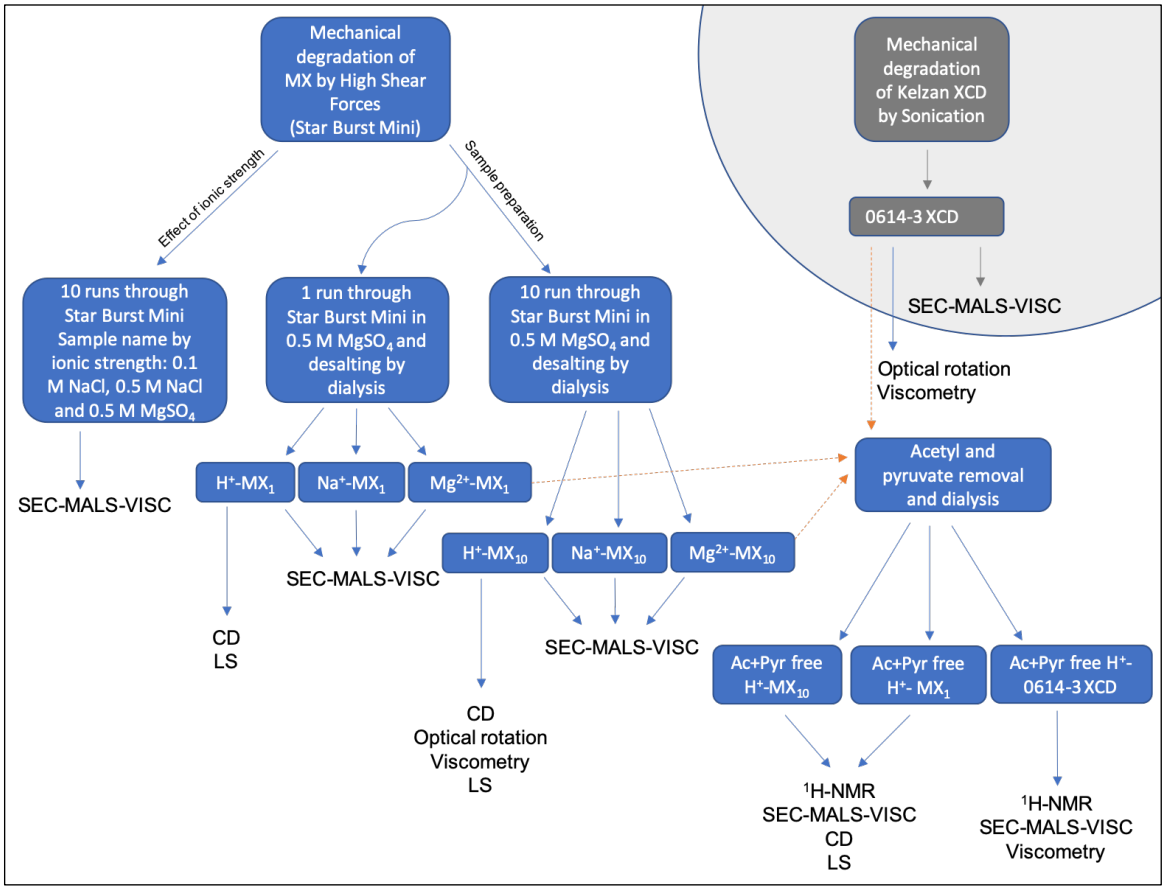

Figure 5.1: Flow-chart of the preparation methods and experimental pathways for the various xanthan samples. The grey colour indicates that the procedure was performed in the master work of Ina Beate Jenssen (IBT, NTNU Trondheim 2013/2014). MX is xanthan purified from fermentation broth, and Kelzan XCD is commercial xanthan from CP Kelco.

5.1 Mechanical Degradation by High Shear Forces

5.1.1 Effect of Ionic Strenght During Degradation

Mechanical degradation in Star Burst Mini is performed at high pressure (220 MPa) which is likely to cause a high, but yet unknown temperature at the site of depolymerisation. The high temperature could drive xanthan to its disordered state, causing random coil behaviour in solution and undesirable properties. When MX was mechanically degraded with 0.1 M NaCl in

the project work, random coil-like conformation was detected by SEC-MALS-VISC. The effect of ionic strength on the conformation during mechanical degradation on the conformation was therefore further investigated. The results are included here to demonstrate the choice of ionic strength in subsequent sample preparations.

MX in different ionic strengths, i.e. 0.1 M (0.1 M NaCl), 0.5 M (0.5 M NaCl) and 2 M (0.5 M $MgSO_4$) were mechanically degraded by ten runs through Star Burst Mini. The number of runs was chosen based on the master thesis of Christian Holmvik (IBT, NTNU Trondheim 2017/2018) [47]. The samples were further analysed directly, without any purification step, by SEC-MALS-VISC. A flow chart of the sample handling and analyses is shown in Figure 5.2.

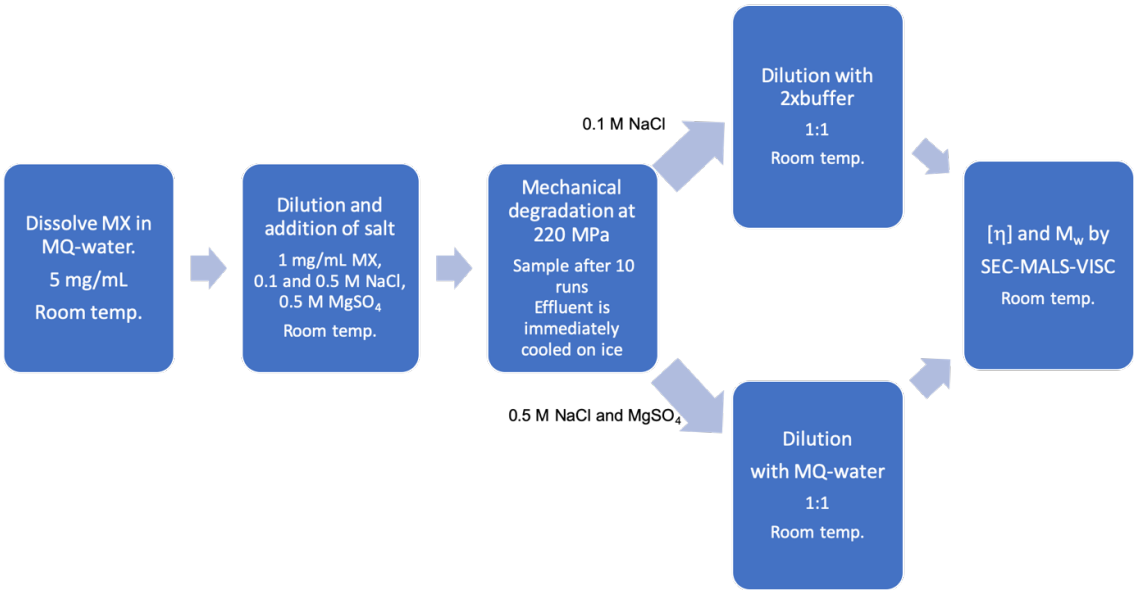

Figure 5.2: Procedure and handling overview for MX samples degraded at different ionic strengths to study of effect of ionic strength during mechanical degradation.

ASTRA 7.1.4 was used to process the data obtained by SEC-MALS-VISC, using Berry to the second power as regression model. The conformation of the degraded samples were evaluated from RMS conformation- and MHS-plots, presented in Figure 5.3 and Figure 5.4, respectively.

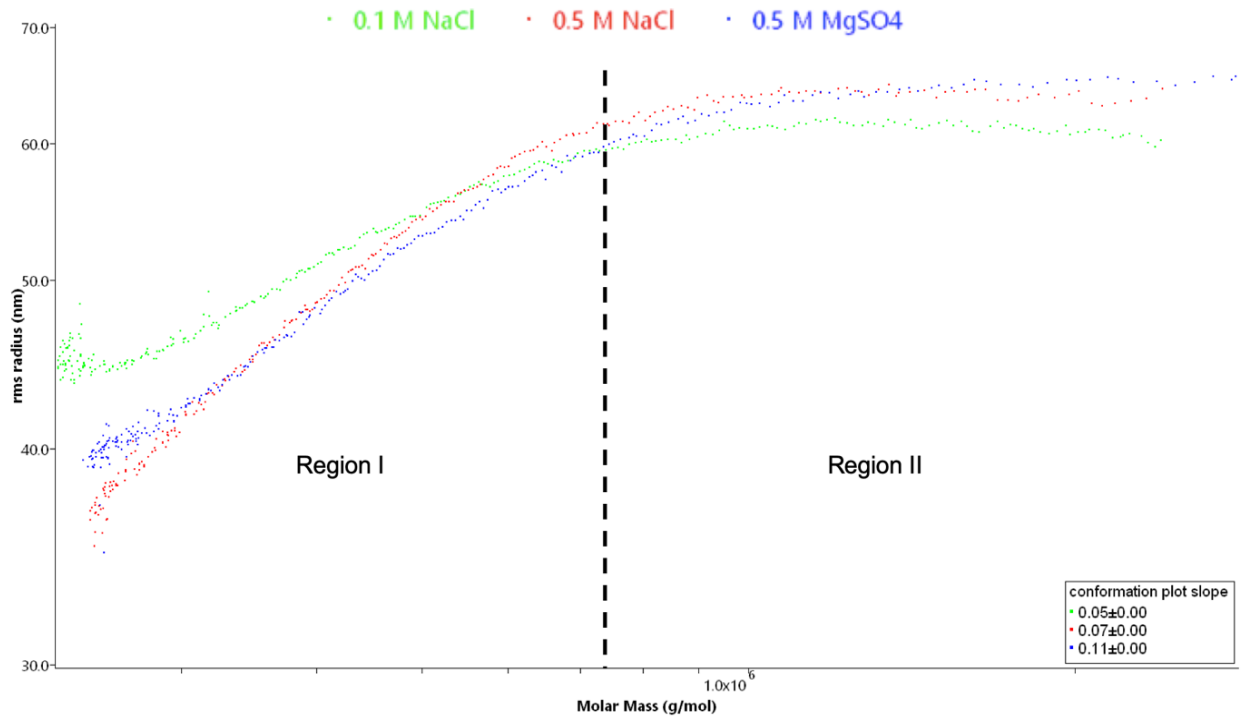

Figure 5.3: RMS conformation plots (R_G as a function of M_w) of MX mechanically degraded at different ionic strengths (10 runs through Star Burst Mini). The box in the lower right corner shows the regression slopes, corresponding to the exponent a in Equation (3-6).

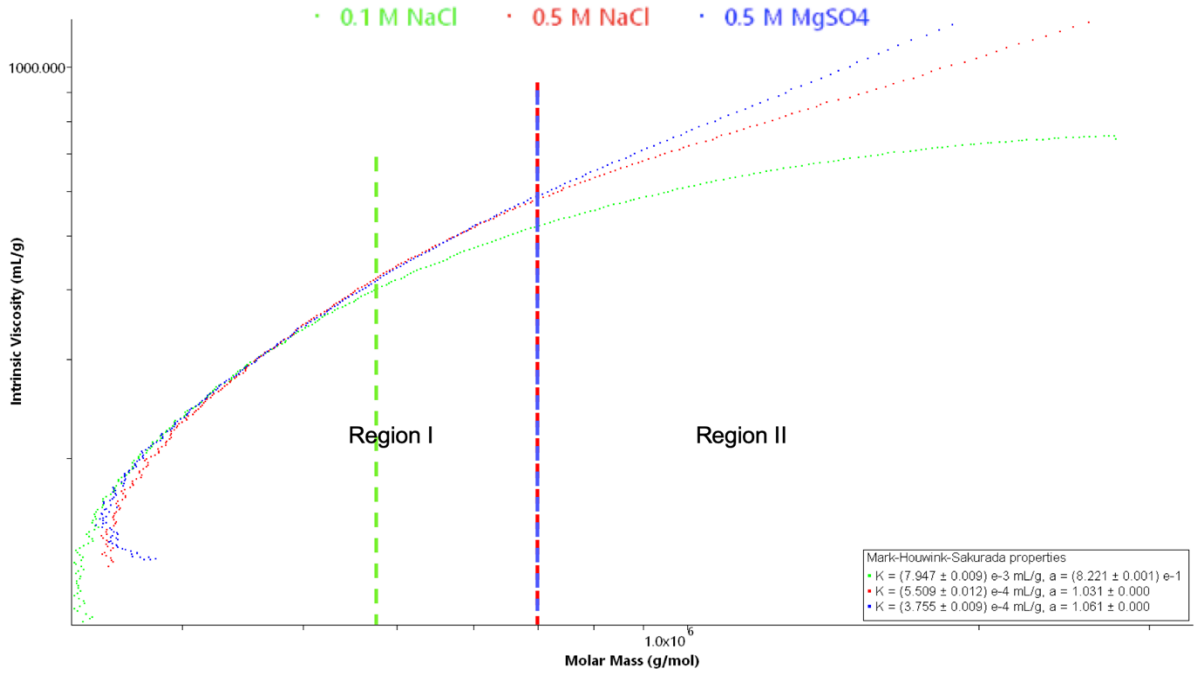

Figure 5.4: MHS-plots (double logarithmic plot of $[\eta]$ as a function of M_w) of MX mechanically degraded at different ionic strengths (10 runs through Star Burst Mini). The box in the lower right corner shows both the MHS constant (K) and the regression slopes (here, a), corresponding to the exponent b in Equation (3-7).

The RMS conformation- and MHS-plot (Figure 5.3 and Figure 5.4, respectively) show different slopes in the low and high regions of molar mass. Different shape parameters are expected depending on the shape of the polymer. Hence, the observation suggests variations in conformation within each sample. This is, however, an expected result, independent of the conformational state of the helix, which reflects the rigidity of shorter chains compared to longer chains, which are more flexible. A vertical line was drawn from the molar mass axis to illustrate the conformational variations for low and high molecular weight. Region I represent the lower molecular weights of the molecular weight distribution, Region II the higher. The shape parameters of the two regions, as well as the overall shape parameters, are presented in Table 5.1.

Table 5.1: Shape parameter (a and b) from the RMS conformation- and MHS-plot of MX mechanically degraded through Star Burst Mini 10 times at different ionic strengths.

		Region I	Region II	Overall
a	0.1 M NaCl	0.2	0.0	0.05
	0.5 M NaCl	0.6	0.1	0.07
	0.5 M $MgSO_4$	0.5	0.1	0.11
b	0.1 M NaCl	1.4	0.3	0.8
	0.5 M NaCl	1.3	0.6	1.03
	0.5 M $MgSO_4$	1.2	0.8	1.06

From both Figure 5.3 and Figure 5.4 (Table 5.1 for shape parameters), the overall shape parameter of 0.1 M NaCl is lower compared to both 0.5 M NaCl and 0.5 M $MgSO_4$, suggesting a less rigid conformation. It can furthermore be seen (Figure 5.4) that 0.1 M NaCl has most narrow Region I, an observation which implies that a smaller fraction of the molecular weight distribution of 0.1 M NaCl is found to have a rigid conformation. The overall MHS shape parameter of the 0.1 M NaCl sample is found to be 0.8, i.e. a slope which is only slightly higher than expected for a random coil (0.6). The findings thus may suggest that the sample has undergone order-disorder transitions during mechanical degradation and that the original

structure is not entirely reformed during renaturation upon cooling, rendering the properties of xanthan.

The sample degraded with 0.5 M $MgSO_4$ shows a broader Region I and a significantly higher shape parameter in Region II compared to both 0.1 M and 0.5 M NaCl, suggesting a more rigid conformation on both sides of the molecular weight distribution. The findings suggest that denaturation has been avoided and thus that the degraded sample is in the native, ordered state. Its overall MHS shape parameter is found to be 1.06, which still is below the ideal shape parameter of 1.8 for rigid rods. However, the results clearly illustrate the importance of performing mechanical degradation at high ionic strength. When it is desired to keep the ordered conformation of xanthan, high ionic strength should be applied.

5.1.2 Preparation of Xanthan Samples

MX was mechanically degraded with 0.5 M $MgSO_4$ by high shear forces and further desalted/purified to produce samples of different molecular weight for subsequent analyses. One and ten runs through Star Burst Mini were performed, producing the samples referred to as native MX_1 and MX_{10}, respectively. Acetate and pyruvate were further removed from a fraction of MX_1, MX_{10} and the sonicated sample 0614-3 XCD, which had been prepared by Ina Beate Jenssen (IBT, NTNU Trondheim 2013/2014). An overview of the preparation procedure of MX_1 and MX_{10}, as well as the procedure for obtaining acetate- and pyruvate-free xanthan samples are presented in Figure 5.5 and Figure 5.6, respectively.

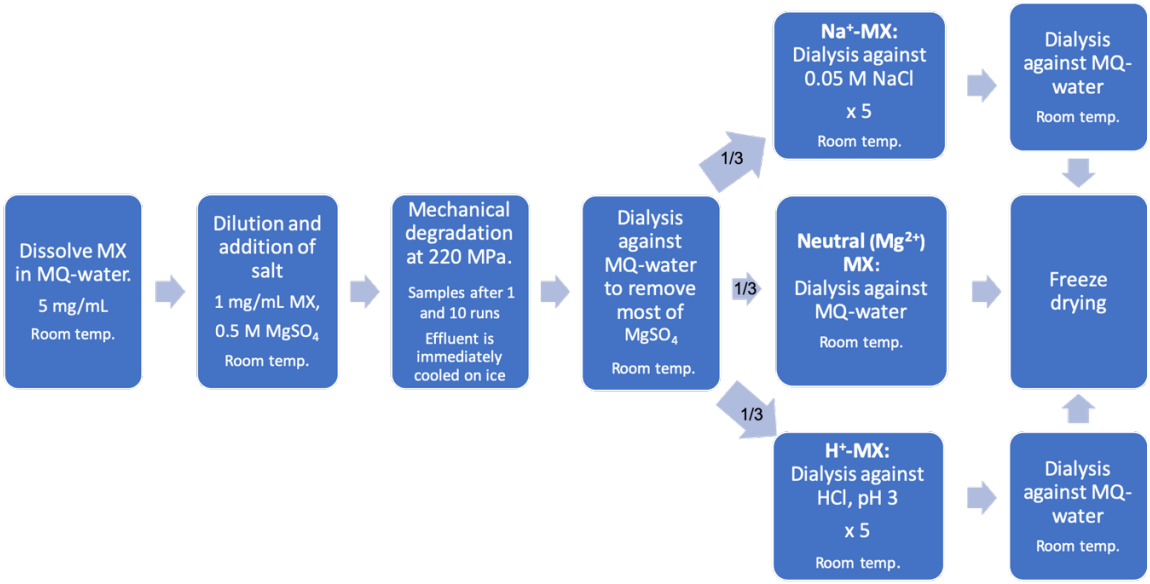

Figure 5.5: Procedure and handling overview of MX-samples mechanically degraded and purified for further analysis.

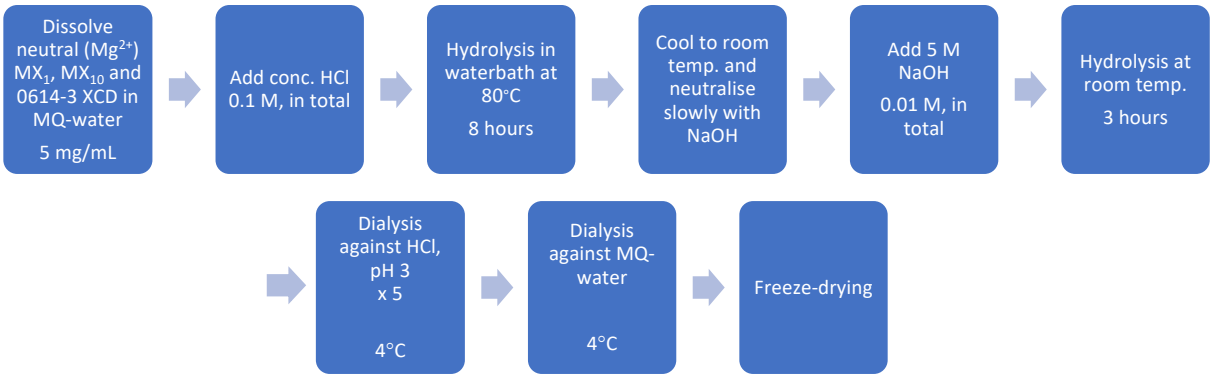

Figure 5.6: Procedure and handling overview of preparation of acetate- and pyruvate-free xanthan.

5.1.3 Characterisation of Samples by ^{1}H-NMR

Acetate and pyruvate were removed from MX_1, MX_{10} and 0614-3 XCD by mild acid- and alkaline hydrolysis to rule out any effect of pyruvate and acetate content on subsequent analyses. It was also desired to investigate a possible effect of structural chemistry on order-disorder transitions. The assumed acetate- and pyruvate-free xanthan samples were analysed by ^{1}H-NMR at 80°C to confirm the removal of substituents. The chemical shifts of the spectra were calibrated relative to the water peak set to 4.25 ppm (at 80°C) The obtained spectra are shown in Figure 5.7, which also includes a reference spectrum of xanthan where both substituents are present.

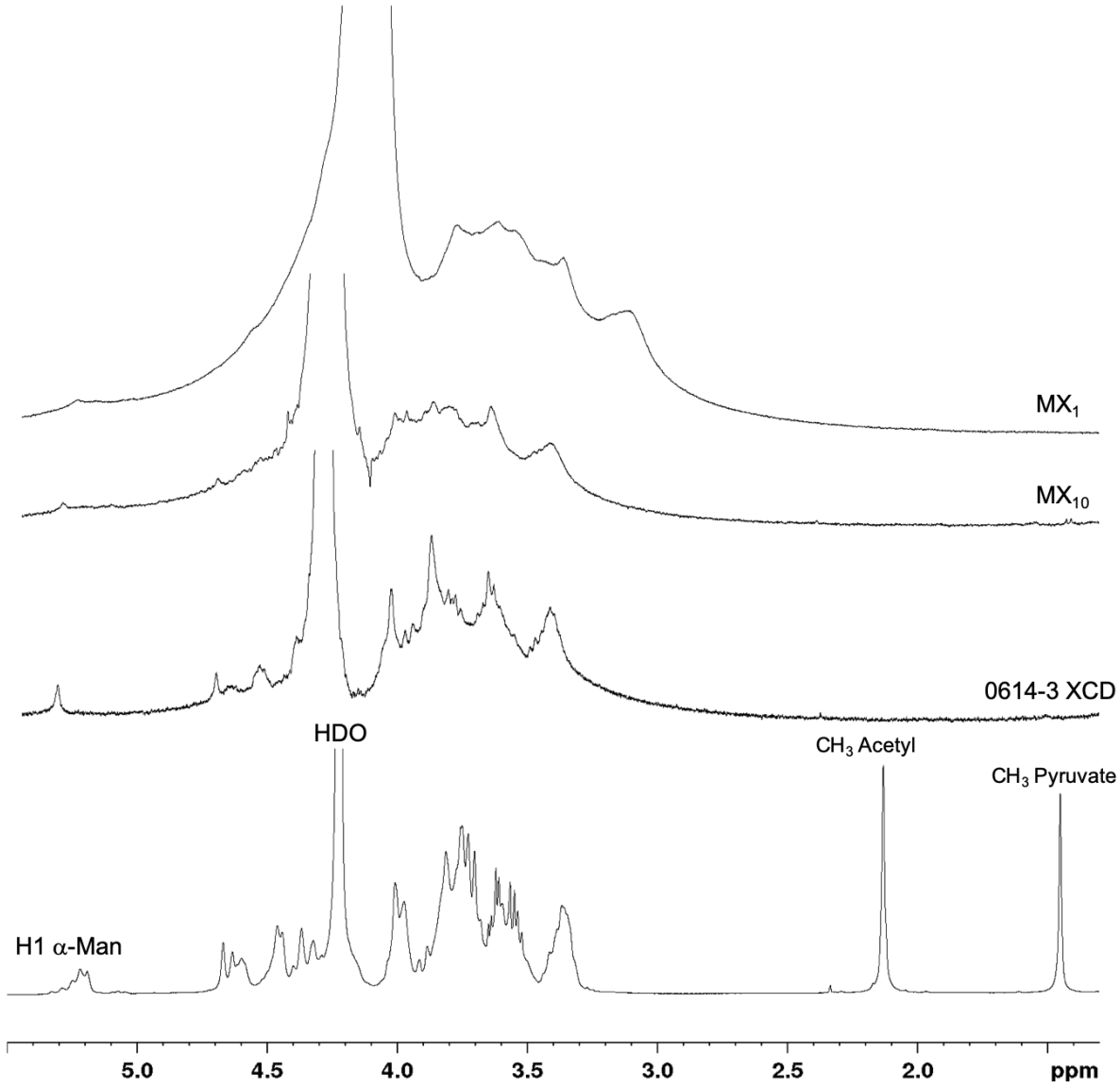

Figure 5.7: ^{1}H-NMR spectra of various xanthan samples obtained at 400 MHz and 80°C in order to confirm the removal of acetate and pyruvate. In the reference spectrum, the peaks of acetyl, pyruvate, H1 α-Man and water are annotated according to the literature [76].

The spectra presented in Figure 5.7 are all in good correlation with the expected reference spectrum. When comparing the upper three spectrums of Figure 5.7 with the annotated reference spectrum, it can readily be observed that the characteristic two peaks of acetate and pyruvate, located around 2.1 and 1.45 ppm, respectively, are missing. Thus, it is confirmed that both substituents successfully have been removed from all three samples.

5.1.4 Characterisation of Samples by SEC-MALS-VISC

Characterisation of mechanically degraded and purified samples were performed using SEC-MALS with on-line viscometry detector. SEC-MALS-VISC has previously analysed MX_1 and MX_{10} degraded in 0.5 M $MgSO_4$ during the project work [21]. However, as new samples were prepared and purification by dialysis was included in the procedure, it was of interest to test the reproducibility of mechanical degradation in terms of M_w, $[\eta]_w$ and $R_{G,w}$, in addition to evaluate the effect of purification on conformation. Acetate- and pyruvate-free xanthan samples (MX_1, MX_{10} and 0614-3 XCD) were also analysed.

ASTRA 7.1.4 was used to process the data obtained by SEC-MALS-VISC, using Berry to the second power as regression model. Each sample was analysed two times, and the average was calculated. In general, the variance between the two measurements was between 1 and 10% for all parameters. The results are presented in Table 5.2 in terms of molecular weight, intrinsic viscosity and radius of gyration. All presented values are weight averages and thus denoted by a subscript w. The elution profiles and molecular weight distributions of each analysis are presented in Appendix B. The salt-form ahead of analysis is indicated by the counterion in parenthesis. Although SEC-MALS-VISC did not determine DS of acetate and pyruvate, these values are also included in Table 5.2 to provide a full overview of the characteristics of each sample.

Table 5.2: Weight average molecular weight (M_w), intrinsic viscosity ($[\eta]_w$) and radius of gyration ($R_{G,w}$) obtained by SEC-MALS-VISC. The eluent used was 0.15 M $NaNO_3$ and 0.01 M EDTA. The presented numbers are calculated as an average of two analyses. Degree of substitution (DS) of acetate and pyruvate are included to provide a full overview of the characteristics of each sample.

Sample name	DS_{Ac}	DS_{Pyr}	M_w [kDa]	$[\eta]_w$ [mL/g]	$R_{G,w}$ [nm]
0614-3 XCD	0.85♦	0.58♦	820*	706*	109*
(H^+)-0614-3 XCD, Ac+Pyr free	-	-	633	872	95
(Mg^{2+}) MX_1			909	763	101
(H^+) MX_1	0.70×	0.52×	938	761	106
(Na^+) MX_1			1021	525	98
(H^+) MX_1, Ac+Pyr free	-	-	688	832	96
(Mg^{2+}) MX_{10}			416	320	46
(H^+) MX_{10}	0.70×	0.52×	507	322	49
(Na^+) MX_{10}			641	364	63
(H^+) MX_{10}, Ac+Pyr free	-	-	230	279	38

The general variance between the two measurements was between 1 and 10% for all parameters.

* Analysis performed by Ina Beate Jenssen (IBT, NTNU Trondheim, 2013/2014) [12].

♦ Determined by Christian Holmvik (IBT, NTNU Trondheim, 2017/2018) [47].

× Determined in the project thesis [21].

From Table 5.2, it can be observed a significant difference between MX_1 and MX_{10}. In general, all the values presented for MX_{10}, i.e. M_w, $[\eta]_w$ and $R_{G,w}$, are roughly half of the values presented for MX_1, which is similar to what was found during the project work and in Christian Holmvik's (IBT NTNU Trondheim 2017/2018) master thesis [21, 47]. This serves as a clear indication of mechanical degradation being successful and reproducible in terms of reducing molecular weight, the radius of gyration and intrinsic viscosity.

5.1.4.1 Effect of Acetate and Pyruvate Removal

Removal of acetate and pyruvate causes the molecular weight of both MX_1, MX_{10} and 0614-3 XCD to drop, which could be explained by the removal of substituents. The most substantial percent-wise in M_w is found in MX_{10} (H^+-form), decreasing from 507 kDa to 230

kDa, which might be explained by MX_{10} having the lowest initial molecular weight, compared to both MX_1 and 0614-3 XCD. Xanthan samples of lower molecular weights have previously been found to be more susceptible to order-disorder transitions [5]. This may have caused MX_{10} to be in the disordered state ahead of and/or during acetate and pyruvate removal, which further could have made the sample more susceptible towards acid- and/or alkaline hydrolysis of the glucosidic bonds under the conditions required to remove the substituents. However, to confirm this hypothesis and evaluate which step that potentially causes the decrease in molecular weight, acetate and pyruvate should be removed in two steps, including a SEC-MALS-VISC analysis in-between, which would provide valuable information on the direct effect of each step.

The intrinsic viscosity and radius of gyration of the different samples are also shown to be influenced by the removal of acetate and pyruvate. Both MX_1 and 0614-3 XCD show increased $[\eta]_w$ when the substituents are removed, which is expected as long as the hydrodynamic radius is kept constant, i.e. the backbone conformation. The observed increase thus suggests that the conformation of MX_1 and 0614-3 XCD is little or not at all affected by the acidic and alkaline conditions when removing acetate and pyruvate. It could also explain why the radius of gyration of the two samples remains almost unchanged when the substituents are removed

The $[\eta]_w$ and $R_{G,w}$ of MX_{10} does, on the other hand, decrease when acetate and pyruvate are removed. Similar results have also been published for other xanthan samples [77]. The reduction in $[\eta]_w$ may suggest that the conformation of MX_{10} is affected by the removal of acetate and pyruvate and might be linked to the substantial reduction in M_w observed for the same sample. As lower molecular weight xanthan samples are more susceptible for denaturation and renaturation to occur, the decreased $[\eta]_w$ and $R_{G,w}$ could be explained by intra-dimer renaturation taking place, e.g. by a hairpin formation [5, 31]. Formation of a hairpin structure would leave the renatured molecules more compact compared to the original molecule and thus the intrinsic viscosity and radius of gyration decreases.

5.1.4.2 Effect of Salt-Form

The different salt-forms of the MX_1 and MX_{10} samples, obtained through dialysis, are converted to the sodium form after analysis due to the sodium containing SEC-MALS-VISC eluent. Thus, all samples should theoretically give similar macromolecular properties as they were prepared in the same way. The obtained SEC-MALS-VISC results in Table 5.2 do, however, suggest

otherwise, as M_w, $[\eta]_w$ and $R_{G,w}$ MX_{10} show to be dependent on the initial salt-form. For MX_{10}, the sample whose counterions were Mg^{2+}, has the lowest molecular weight, while H^+-MX_{10} and Na^+-MX_{10} show increasing values for M_w, respectively. A similar trend can be observed for both $[\eta]_w$ and $R_{G,w}$. Xanthan in acidic solution is known to have reduced $[\eta]_w$ and $R_{G,w}$ compared to sodium xanthan in neutral, aqueous solution at approximately similar M_w, and might explain the lower characteristics of H^+-MX_{10} compared to Na^+-MX_{10} [33]. The findings does, however, suggest that the double helical structure becomes more flexible rather than denaturated.

The macromolecular properties of MX_1 are also dependent on the salt-form. The trend of the molecular weight is similar as for MX_{10}, whereas the trend of both $[\eta]_w$ and $R_{G,w}$ is opposite, leaving Na^+-MX_1 with the lowest $[\eta]_w$ and $R_{G,w}$, Mg^{2+}-MX_1 with the highest. The different trends for MX_1 and MX_{10} may suggest that the conformation of the samples is dependent on the salt-form.

5.1.4.3 Effect of Salt-Form and Structural Chemistry on Conformation

To evaluate the effect of the salt-form and acetate and pyruvate removal on conformation, RMS conformation- and MHS-plots were generated from the M_w, $[\eta]_w$ and $R_{G,w}$ presented in Table 5.2. Data from Sato *et al.* for xanthan in aqueous sodium solution as a reference for optimal conformation over a wide range of molecular weights [11]. Its data are presented in Appendix C. Note that the reference data are the z-averages. However, as the reference sample is almost monodisperse, i.e. has $\frac{M_w}{M_n} = 1.1$, the z-average equals the number- and weight average, making it possible to compare the data [41]. The RMS conformation- and MHS plots are presented in Figure 5.8 and Figure 5.9, respectively. The different samples are annotated according to their counterion before analysis by SEC-MALS-VISC or lack of acetate and pyruvate.

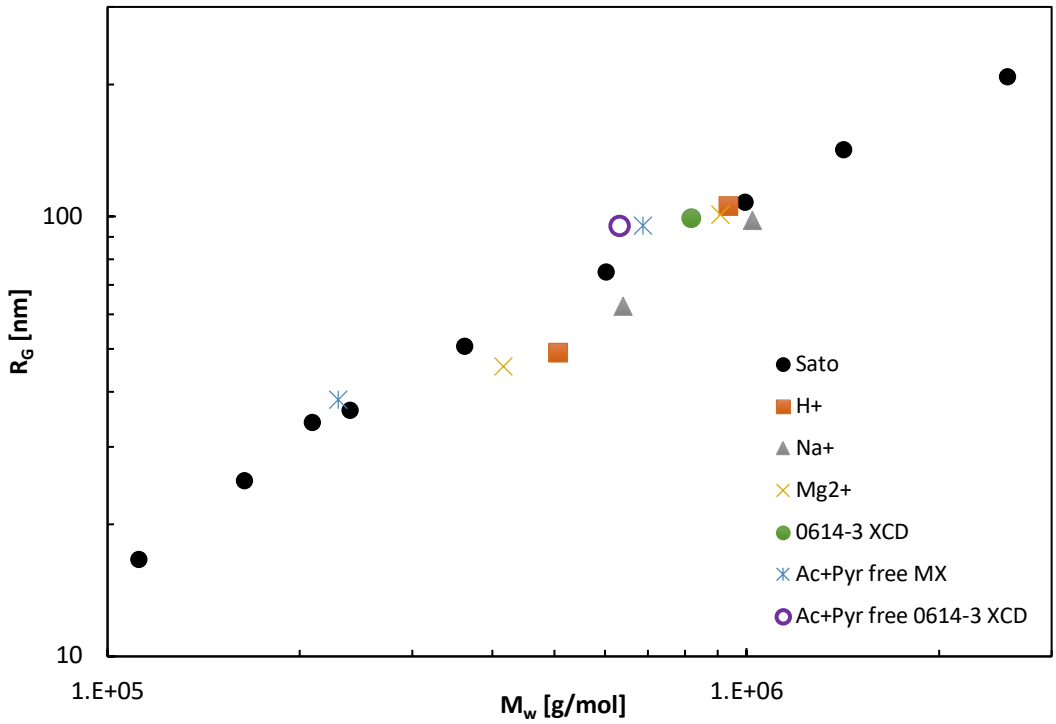

Figure 5.8: RMS-conformation plot of the xanthan samples analysed by SEC-MALS-VISC compared to reference data for xanthan in aqueous sodium solution published by Sato *et al* [11].

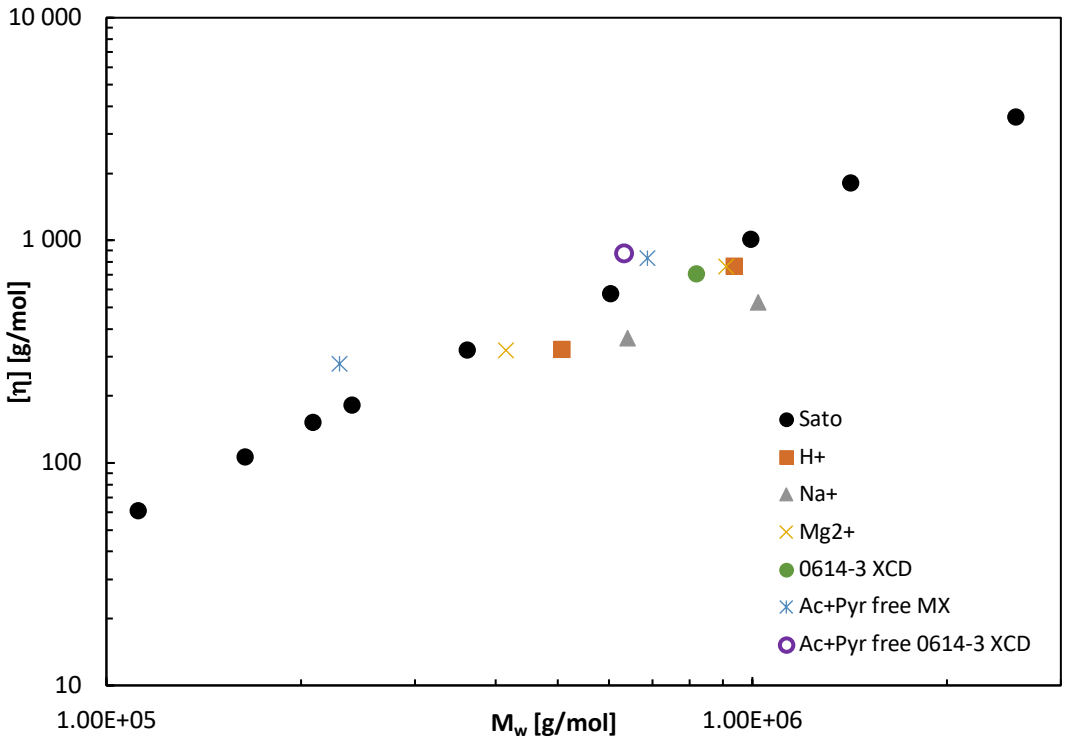

Figure 5.9: MHS plot of the xanthan samples analysed by SEC-MALS-VISC compared to reference data for xanthan in aqueous sodium solution published by Sato *et al* [11].

From Figure 5.8 and Figure 5.9, it can be observed that the sonicated sample, 0614-3 XCD, is in good accordance with the reference data from Sato *et al*. Thus, it is confirmed to be an ideal reference sample for mechanically degraded MX. Evaluating the conformation of the mechanically degraded MX samples, both Na^+-MX and H^+-MX have lower $R_{G,w}$ and $[\eta]_w$, compared to the Sato reference sample at similar molecular weight, which may suggest a less ideal and looser helical conformation. A looser conformation is expected for H^+-xanthan but not for Na^+-xanthan, which further may suggest that denaturation has occurred in the latter sample [33]. Another explanation could be the formation of aggregates during desalting by dialysis, which may not be entirely solved by the shear forces in the SEC-column. $R_{G,w}$ and $[\eta]_w$ of Mg^{2+}-MX are closer to the Sato reference sample at similar molecular weight, suggesting that presence of Mg^{2+} as a counterion results in more ideal and rigid double helical conformation compared to the presence of Na^+ and H^+.

Both $R_{G,w}$ and $[\eta]_w$ of the acetate- and pyruvate-free xanthan samples are higher than the values of the Sato reference sample at similar molecular weight, which suggests an even more rigid conformation of these samples. Hence, removal of acetate and pyruvate, which is performed after mechanical degradation, seems to recover a more favourable conformation. The improved conformation might be explained by the mild acid- and/or alkaline conditions in the preparation procedure of acetate- and pyruvate-free xanthan, dissolving potential aggregates.

5.1.4.4 Effect of Purification on Conformation

In the project work, MX degraded with 0.5 M $MgSO_4$ were analysed directly by SEC-MALS-VISC without any purification step. However, to obtain mechanically degraded samples of lower molecular weight suitable for other analyses, desalting by dialysis followed by freeze-drying was performed. To evaluate the effect of the purification procedure on conformation, the SEC-MALS-VISC data obtained for the non-purified MX degraded with 0.5 M $MgSO_4$ (10 runs through Star Burst Mini) during the project work were plotted in RMS conformation- and MHS-plots together with the data of purified (Mg^{2+})-MX_{10}. The resulting plots are presented in Figure 5.10 and Figure 5.11, respectively.

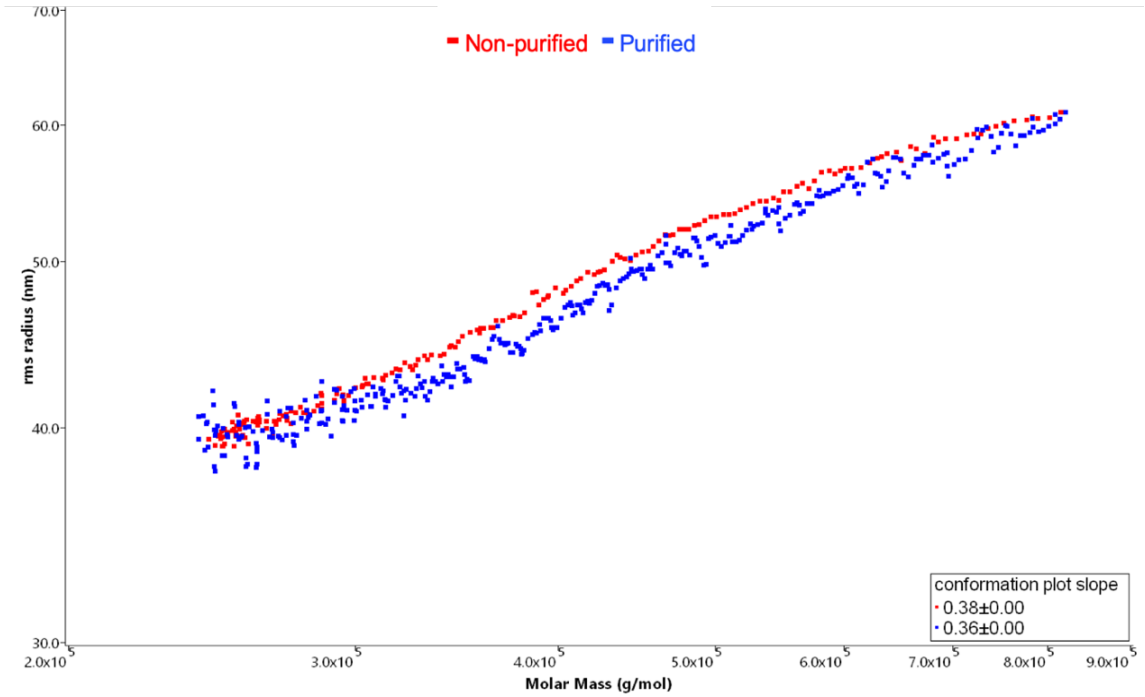

Figure 5.10: Conformation plots (R_G as a function of M_w) of MX_{10}, mechanically degraded with 0.5 M $MgSO_4$, before and after purification. The box in the lower right corner shows the regression slopes, corresponding to exponent a in Equation (3-6).

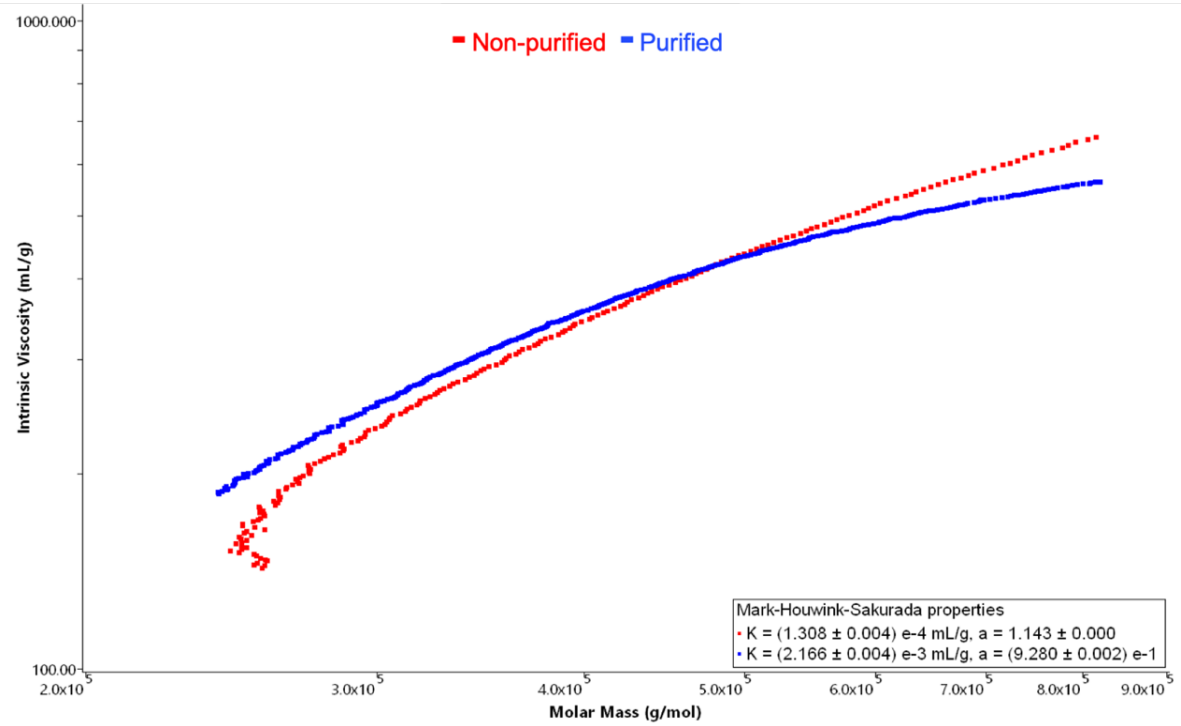

Figure 5.11: MHS-plots (double logarithmic plot of $[\eta]$ as a function of M_w) of MX_{10}, mechanically degraded with 0.5 M $MgSO_4$, before and after purification. The box in the lower right corner shows MHS constant (K) and the regression slopes (here, a), corresponding to exponent b in Equation (3-7).

From the RMS conformation- and MHS-plots it can readily be observed that the conformation of purified and non-purified MX_{10} are similar, as their plots are closely associated and have similar regression slopes, especially in the RMS conformation-plot. In the MHS-plot, the purified sample is found to have a shape parameter of 0.982, while the non-purified sample shows a shape parameter of 1.14. The slightly higher shape parameter of the non-purified sample might be explained by the low amount of handling taking place before analysis compared to the purified samples. The latter sample has undergone dialysis to remove the excess of $MgSO_4$. Hence, a reduction in ionic strength occurs, lowering T_m. As dialysis was performed at room temperature, the purified MX_{10} samples may have started some transition towards disorder, making the molecules more flexible. Nevertheless, dialysis seems to be an appropriate method to remove excess salt after mechanical degradation without introducing substantial changes in conformation. However, dialysis at lower temperatures might be considered to further optimise the complete procedure for obtaining mechanically degraded and purified xanthan.

5.2 Conformation of Acidic Xanthan in Water and DMSO

It has previously been reported by Fantou *et al*. that acidic xanthan needs to be heated to be fully dissolved in DMSO [19]. However, all xanthan samples, i.e. both native and acetate- and pyruvate-free MX_1, MX_{10} and 0614-3 XCD, were found to be completely dissolved in DMSO after one night at stirring. Thus, it was found that heating is needed to dissolve acidic xanthan in DMSO.

5.2.1 Conformational Study by Circular Dichroism

The conformational state of H^+-MX_1 and MX_{10}, both native and acetate- and pyruvate-free, were studied by CD in order to confirm the results published by Fantou *et al.*, claiming xanthan to be disordered in DMSO when on its acid form [19]. Another objective was to determine the T_m of the different samples in both water and DMSO by increasing the temperature.

5.2.1.1 MQ-Water as Solvent

CD was performed at wavelengths from 210 to 270 nm at both 20 and 90°C in a 5 mm cell. Each spectrum was determined as an average of 10 spectra, baseline-corrected and further normalised by applying Equation (3-24). The resulting spectra are shown in Figure 5.12.

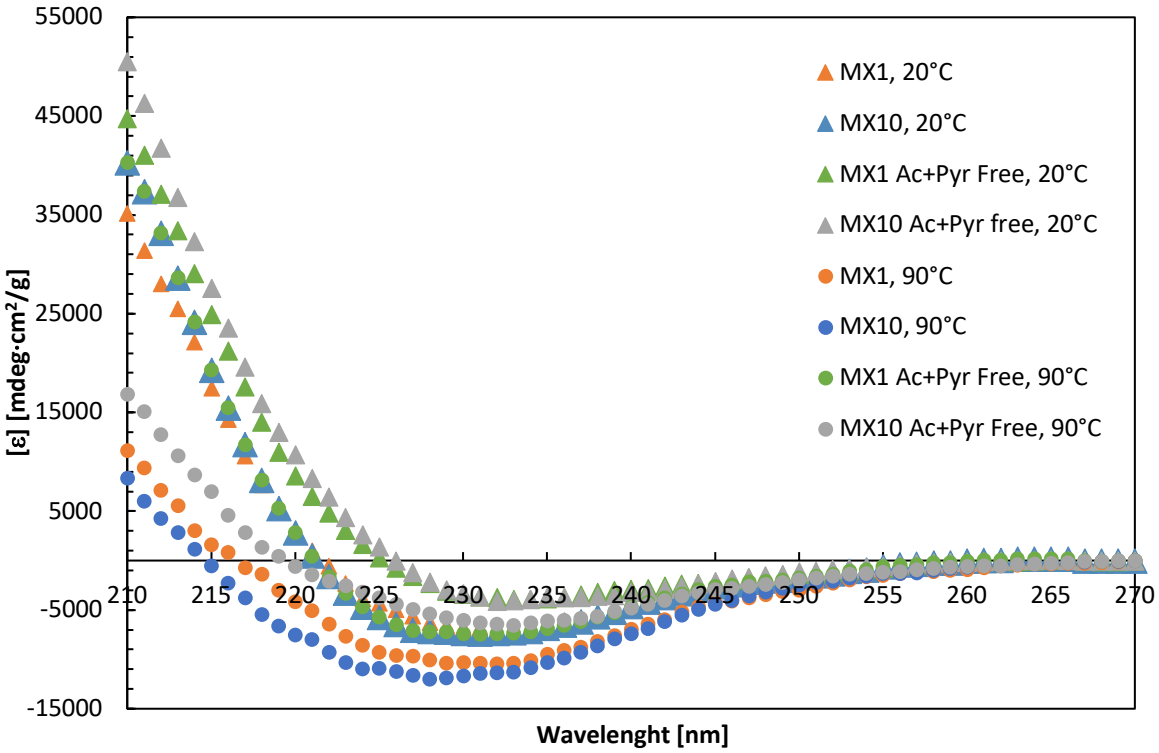

Figure 5.12: Circular dichroism spectra of native and acetate- and pyruvate-free H^+-MX_1 and MX_{10} in MQ-water at both 20 and 90°C.

The CD spectra presented in Figure 5.12 resembles CD spectra of xanthan previously published, by having two main absorption band: A positive peak at 205 nm and a negative, defined as a trough from literature, located around 220 nm [45]. The peak represents the ordered state of xanthan, whereas the trough represents the disordered state [31, 78].

Both absorption bands of native MX_1 and MX_{10} are found to change when the temperature is risen from 20 to 90°C, indicating changes in structural conformation. The peaks at 205 nm show a linear decrease in ellipticity with increasing temperature, suggesting that a non-cooperative transition takes place, lowering the fraction of ordered structure. In contrast, the amplitude of the trough increases cooperatively when the temperature rises, suggesting that xanthan becomes more disordered, as such behaviour would not be expected if increasing temperature only caused the levelling of vibrational and rotational energy states [45]. Similar behaviour of the peak and trough with increased temperature has also been shown by Morris *et al.*, illustrated in Figure 5.13.

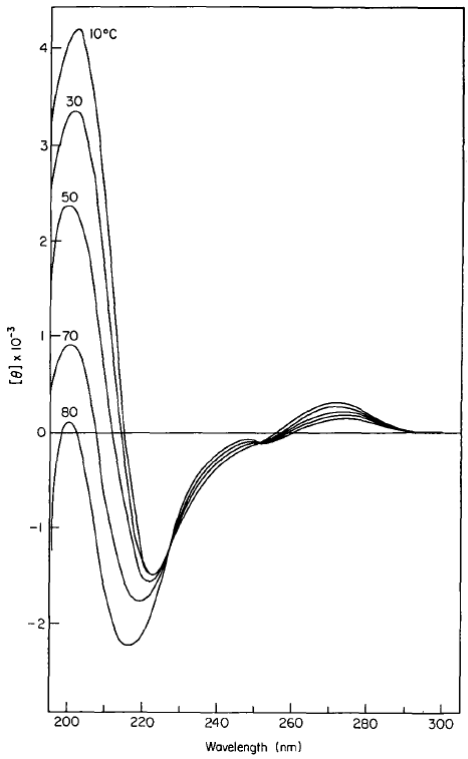

Figure 5.13: Circular dichroism spectra showing the temperature dependence of xanthan [45]. The number on top of each positive peak corresponds to the temperature the spectrum was obtained.

The 205 nm peak of acetate- and pyruvate-free MX_{10} behave similarly (and non-co-operatively) to that of native MX_{10}, suggesting that the ordered conformation becomes less abundant at 90°C. The ellipticity of the 220 nm trough, on the other hand, seems less temperature dependent. For acetate- and pyruvate-free MX_1, both absorption bands, are almost independent of temperature, which may imply that the conformation is unaffected by increasing temperature. The observations may suggest that removal of both acetate and pyruvate stabilises the ordered structure of xanthan, preventing order-disorder transitions.

To further study the effect of temperature, temperature scans from 20 to 90°C at a fixed wavelength of 215 nm, were performed. Measurements at this wavelength allows for investigation of changes in the absorption band of the ordered state of xanthan. The CD spectra of each sample were baseline-corrected and further normalised by applying Equation (3-24). The results are presented in Figure 5.14.

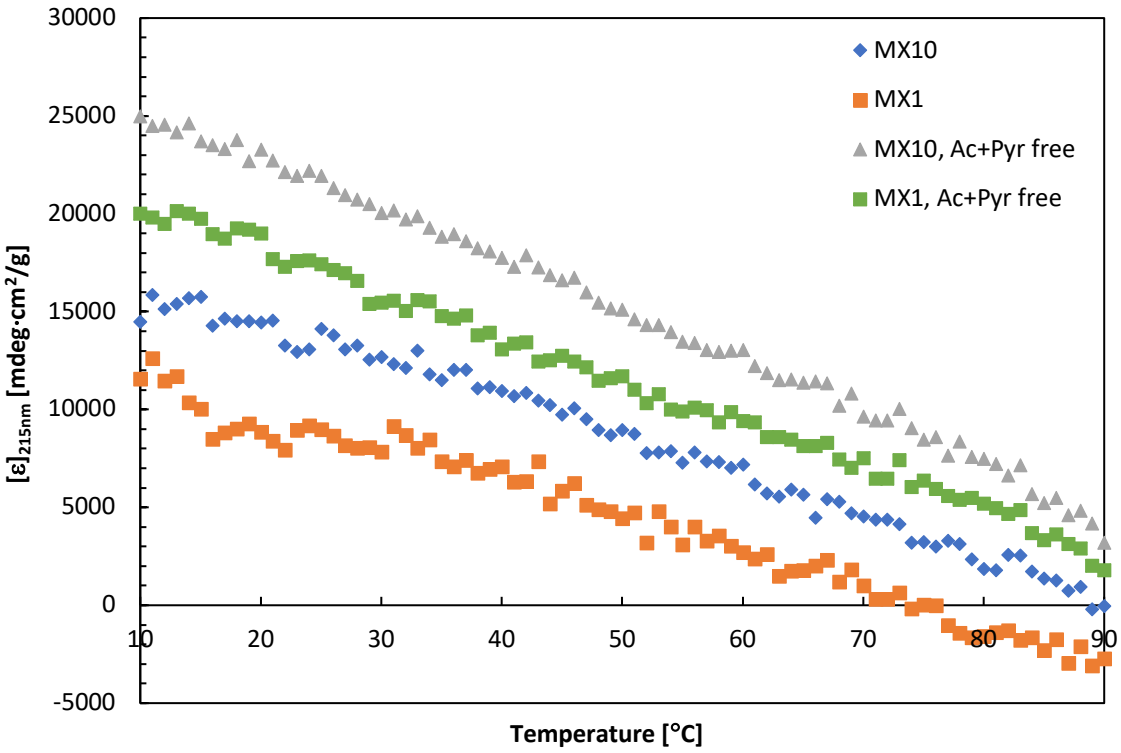

Figure 5.14: The temperature dependency of native and acetate- and pyruvate-free H^+-MX_1 and MX_{10} in MQ-water at 215 nm.

From Figure 5.14, all samples have a linear decrease in ellipticity with increasing temperature, independent of molecular weight and presence substituents. Nevertheless, the acetate- and pyruvate-free MX_1 and MX_{10} provide higher ellipticity throughout the temperature range, suggesting that these samples have a more ordered, rigid conformation, even from the beginning. Similar observations were also found when analysing the characteristics of the samples by SEC-MALS-VISC. If an order-disorder transition took place in the given temperature interval, a sigmoidal shaped curve with a negative slope are expected. The results therefore imply that no complete order-disorder transition in the given temperature interval and that the ordered state is obtained for all temperatures measured. The lack of an observed transition might be explained by the increased stability of H^+-xanthan at higher temperatures compared to Na^+-xanthan [34]. However, a similar, linear decrease in ellipticity at 215 nm with increasing temperature has, also been found by Morris *et al.* for deacetylated, sodium xanthan (Figure 5.15).

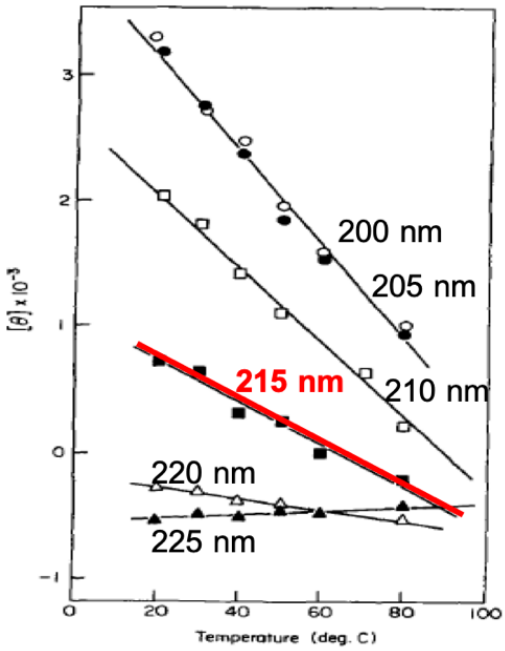

Figure 5.15: Wavelength dependence of circular dichroism of deacetylated xanthan in water, obtained by Morris *et al* [45]. The red, bold line corresponds to the same wavelength, 215 nm, used for the temperature scan of H^+-MX in MQ-water.

As no order-disorder transition was observed in the measured temperature interval, T_m could not be determined for any of the mechanically degraded MX samples analysed, but is suggested to be > 90°C.

5.2.1.2 DMSO as Solvent

Fantou *et al.* have previously studied xanthan in DMSO and water by CD spectroscopy and performed a wavelength scan from 200 to 270 nm [19]. However, when attempting to reproduce the spectrum in a 0.5 cm quartz cell, voltage > 1000 V was observed, indicating that light is not able to pass through the sample, causing no signal to be obtained. In an attempt to overcome this, quartz cells of shorter optical wavelengths, i.e. 0.2 cm, 0.1 cm and 0.1 mm were tested. However, the high voltage was still observed. The high voltage might be caused by the absorbance of DMSO, which increases for wavelengths below 250 nm, i.e. the range where the peaks of xanthan are visible [79]. The CD spectra of xanthan in DMSO was thus not possible to reproduce, which of course raises a question to the CD spectrum of xanthan in DMSO obtained by Fantou *et al.* (Figure 1.1).

5.2.2 Order-Disorder Transitions in Water/DMSO Mixtures

As CD provided little information on the state of acidic xanthan in DMSO, optical rotation was considered, which contrary to CD, provide a signal at a wide range of wavelengths. A Photophysics Chirascan Series with optical rotatory dispersion accessory was considered for the measurements due to its ability to include temperature scans, allowing for detection of thermal order-disorder transition and determination of T_m. However, the Photophysics Chirascan optical rotation failed to be adequately calibrated, and thus, initial test results were off limits. Time was put into trial and error, making the calibration right, however without any success. The trial and error attempts are further elaborated in Appendix D.

Given the issues with both CD spectroscopy in DMSO and optical rotation with temperature scans, it was decided to study whether a (cooperative) change in optical rotation and/or solution viscosity could be observed when the concentration of DMSO was gradually increased from 0 to 100%. The aim was to detect a possible conformational transition at a critical fraction of DMSO, f_{DMSO}. Similar studies have previously been done on the polysaccharide Schizophyllan [54, 80].

5.2.2.1 Optical Rotation

Optical rotation was performed in a 10 cm quartz cell at a fixed temperature of 25°C on acidic xanthan samples (native MX_{10} and 0614-3 XCD) in water containing different weight fractions of DMSO. The optical rotation of each sample was corrected for the cell length and concentration by applying Equation (3-24). The specific optical rotation is presented as a function of w/w% DMSO in Figure 5.16.

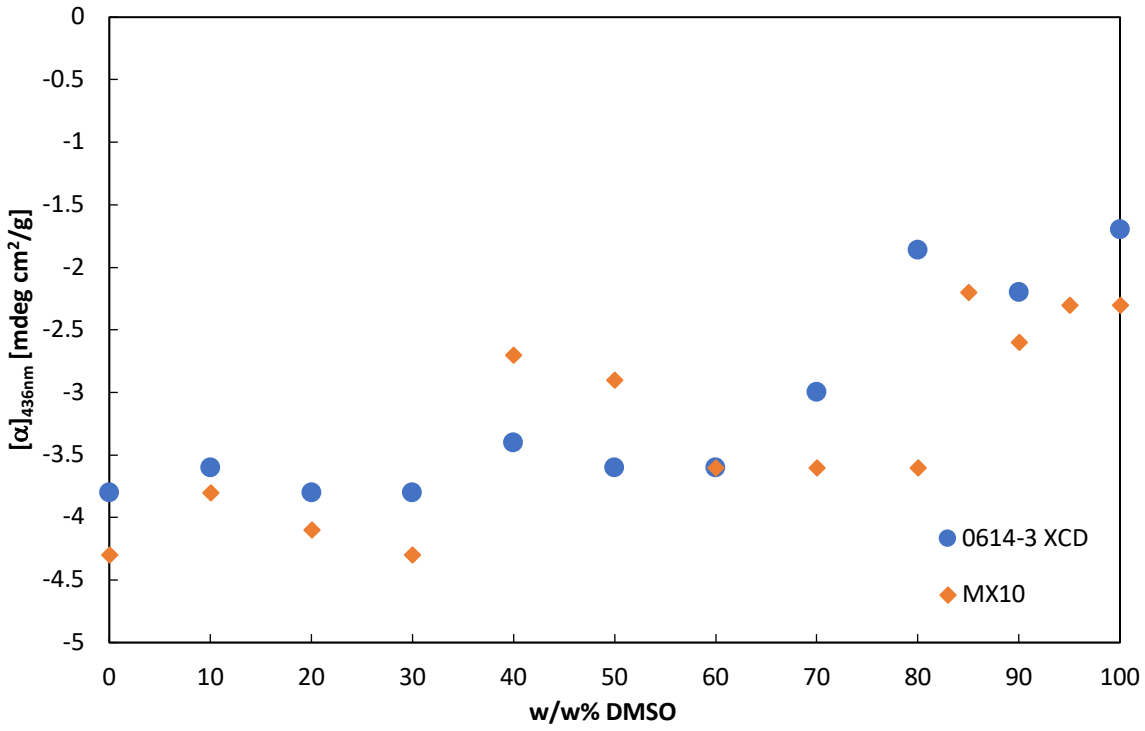

Figure 5.16: Specific optical rotation ($[\alpha]_{436}$) of H^+-xanthan at 25°C as a function of w/w% DMSO.

Figure 5.16 shows that 0614-3 XCD and MX_{10} follow the same trend; the optical rotation is stable around -4 mdeg cm^2/g for low weight fractions of DMSO, before an increase can be observed between 70 and 80 w/w% DMSO. From 80 to 100 w/w% DMSO, the optical rotation is stable at around -2 mdeg cm^2/g. The increase in optical rotation may suggest structural changes around 80 w/w% DMSO, possibly caused by an order-disorder transition.

An increase in optical rotation can also be observed around 40 and 50 w/w% DMSO, especially for H^+-MX_{10}. However, as the optical rotation drops back to approximately the initial values when measured at 60 w/w% DMSO. This may suggest that the observed increase is a result of noise in the measurements.

5.2.2.2 Capillary Viscometry

Due to the observed scattering of data from optical rotation, capillary viscometry was applied to confirm the anticipation of an order-disorder transition taking place around 70 and 80 w/w% DMSO. Capillary viscometry was performed at 25°C on H^+-xanthan samples (native MX_{10} and 0614-3 XCD, both native and acetate- and pyruvate-free) in water containing different weight fractions of DMSO. The flow-through times was measured five to six times and corrected by

Hagenbach Correction Time by applying Equation (3-18). The measured flow-through times, calculated averages and Hagenbach Correction Times are presented in Appendix E. The η_r and η_{sp} was calculated by applying Equation (3-20) and Equation (3-21), respectively. Appendix E also includes an example calculation for obtaining the reduced viscosity. The reduced viscosity $\left(\frac{\eta_{sp}}{c}\right)$ was then plotted as a function of w/w% DMSO, as shown in Figure 5.17.

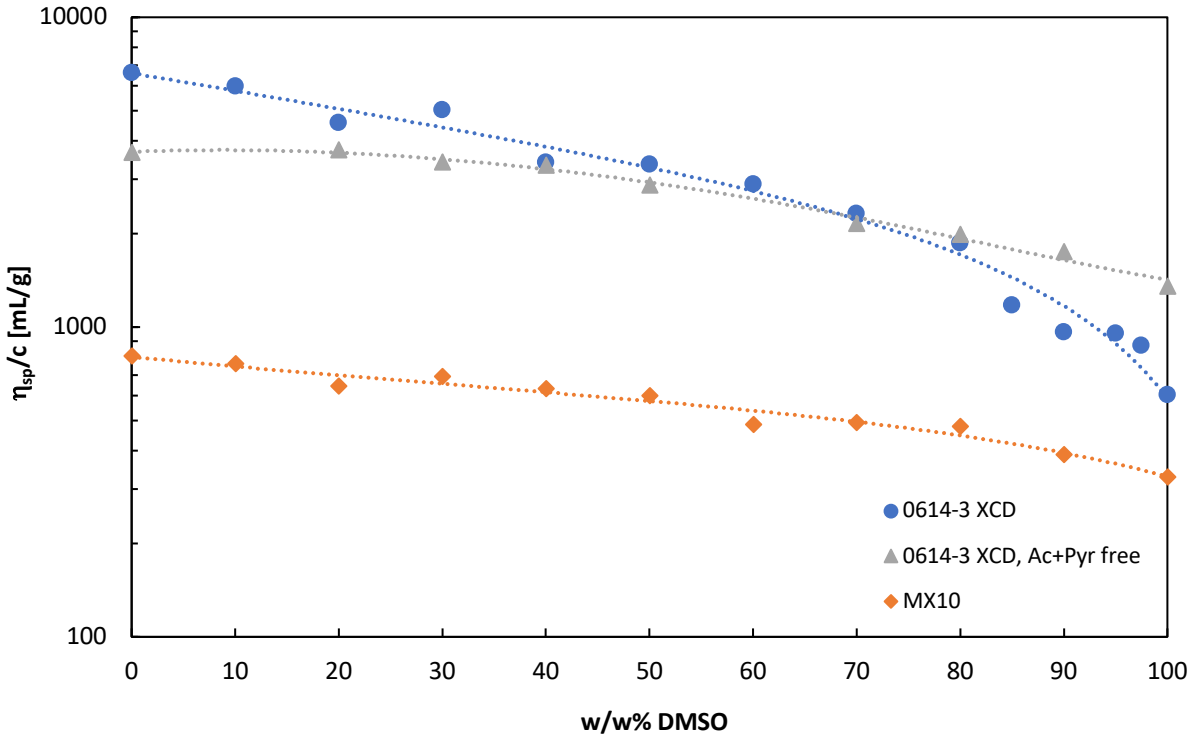

Figure 5.17: Reduced viscosity $\left(\frac{\eta_{sp}}{c}\right)$ of H^+-xanthan in water/DMSO mixtures as a function of w/w% DMSO. Measurements were made in a water bath at 25±0.01°C

In Figure 5.17, native 0614-3 XCD show a gradually and linear decrease in reduced viscosity until about 80 w/w% DMSO, where a sudden drop is observed. A reduced solution viscosity is known to be characteristic for the disordered state of xanthan. Hence, the drop at around 80 w/w% DMSO suggests that an order-disorder transition occurs around this fraction of DMSO. The observation, connected to the results obtained by optical rotation, suggests that $f_{DMSO} = 0.8$.

The gradual decrease in reduced viscosity is also seen for acetate- and pyruvate-free 0614-3 XCD, however, with a flatter slope, and no apparent drop. Removal of substituents thus seems to make xanthan less dependent of the DMSO content. A linear decrease can also be observed of lower molecular weight xanthan, i.e. MX_{10}, however at lower values of reduced viscosity. The lack of a defined drop in reduced viscosity of acetate- and pyruvate-free 0614-3 XCD and

MX_{10} suggests that f_{DMSO} and thus the ability of order-disorder transitions taking place when DMSO is introduced, is dependent of both the acetate and pyruvate content, as well as the molecular weight of the sample.

From Figure 5.17, it can also be observed that the viscosities obtained for 0 w/w% DMSO by capillary viscometry are significantly higher than those obtained by SEC-MALS-VISC (Table 5.2). The difference could be explained by the lack of correction of $\frac{\eta_{sp}}{c}$ by Huggin's constant (Equation (3-23)), as only one concentration was analysed by capillary viscometry. Thus, exact extrapolation towards zero concentration (Equation (3-22)) was not possible. Another explanation could be the difference in shear forces between the two analytical tools, which could have impacted the viscosity as xanthan is known to have shear-thinning behaviour.

5.2.3 Characterisation by Light Scattering

As a last attempt to possibly obtain a better understanding of xanthan in DMSO, acidic native and acetate- and pyruvate-free MX_1 and MX_{10} was analysed in pure DMSO and MQ-water by light scattering. The effect of temperature was also investigated, analysing temperatures from 20 to 50°C, to evaluate possible thermal order-disorder transitions. Only one concentration was analysed due to time limitations connected to the availability of the equipment and data analysis. As a consequence of analysing only one concentration, A_2 was not determined. Hence, the parameters obtained by SLS and DLS are apparent values, denoted by the subscript "app".

5.2.3.1 Refractive Index Increment

To analyse light scattering data, $\left(\frac{\partial n}{\partial c}\right)_{\mu}$ of each sample at the light scattering wavelength has to be known and were consequently determined at 532 nm. Note that the samples were not dialysed against their solvent to obtain a constant chemical potential in order to prevent absorption of water into DMSO [75]. Thus, the refractive index increments presented are referred to as $\frac{\partial n}{\partial c}$, to signify the lack of constant chemical potential.

$\frac{\partial n}{\partial c}$ was measured at both 20 and 50°C, whereas a linear regression model was used to calculate $\frac{\partial n}{\partial c}$ for 30 and 40°C. $\frac{\partial n}{\partial c}$ of samples in DMSO were measured at 20°C and attempted measured at 50°C, however without success due to rapid absorption of water to DMSO when exposed to

air [75]. For these samples, $\frac{\partial n}{\partial c}$ at elevated temperatures were therefore determined by regression models, using the same slope as for the respective sample in MQ-water. The regression models and calculations are presented in Appendix F.

The values of $\frac{\partial n}{\partial c}$ are presented in Table 5.3. Note that $\frac{\partial n}{\partial c}$ were determined for H^+-MX_{10} samples only, due to discussions with prof. Sato, stating independency of molecular weight on $\frac{\partial n}{\partial c}$. Thus, $\frac{\partial n}{\partial c}$ measured for any sample of MX_{10} should also apply for MX_1 with the same chemistry in the same solvent.

Table 5.3: The refractive index increment ($\frac{\partial n}{\partial c}$) of native and acetate- and pyruvate-free H^+-MX_{10} in MQ-water and DMSO at different temperatures at wavelength 532 nm in vacuum.

	$\frac{\partial n}{\partial c}$ [mL/g]			
	20°C	**30°C**	**40°C**	**50°C**
MX_{10} in MQ-water	0.135	0.136*	0.136*	0.136
Ac+Pyr Free MX_{10} in MQ-water	0.137	0.136*	0.135*	0.134
MX_{10} in DMSO	0.034	0.034♦	0.034♦	0.034♦
Ac+Pyr Free MX_{10} in DMSO	0.022	0.021♦	0.019♦	0.018♦

* Obtained from regression model between 20 and 50°C
♦Obtained from regression model using the same slope as the respective MX sample in MQ-water.

From Table 5.3 it can be observed that $\frac{\partial n}{\partial c}$ of native H^+-MX_{10} in MQ-water increases marginally with increasing temperature, whereas $\frac{\partial n}{\partial c}$ of acetate- and pyruvate-free H^+-MX_{10} show a slightly decreasing trend. The obtained values for both native and acetate- and pyruvate-free H^+-MX_{10} in MQ-water are in good accordance with other reported values for xanthan samples in dilute salt solutions: Stahl and Schultz determined $\frac{\partial n}{\partial c}$ to be 0.129 mL/g, although Christensen has reported 0.150 mL/g [1, 81].

Native and acetate- and pyruvate-free H^+-MX_{10} in DMSO show similar trends with increasing temperature as the samples in MQ-water because the same slopes were used to calculate $\frac{\partial n}{\partial c}$.

The values are, however, significantly lower in DMSO. To the best of knowledge, $\frac{\partial n}{\partial c}$ of xanthan in DMSO has not been studied and published previously. Thus, the values in Table 5.3 cannot be compared directly to a specific number. However, Tao and Zhang reported $\frac{\partial n}{\partial c}$ of the polysaccharide (1→6),(1→4),(1→3)-β-D-glucan in DMSO to be 0.03 mL/g, while $\frac{\partial n}{\partial c}$ of the polysaccharide curdlan was reported to be 0.043 mL/g by Tada *et al.* [82, 83]. The obtained values of $\frac{\partial n}{\partial c}$ in DMSO are thus in the same range of what has been reported previously for other polymers in DMSO, and it is, therefore, reasonable to apply them in further light scattering calculations.

5.2.3.2 Static Light Scattering

To determine $M_{w,app}$ and $R_{G,app}$, $\sqrt{\frac{K^*c}{R_\theta}}$ obtained from SLS data were plotted against $\sin\left(\frac{\theta}{2}\right)$ and the slope and intercept were determined. Note that the two lower and the two higher angles were neglected in the Berry plot due to deviation from linearity. The $M_{w,app}$s obtained for native and acetate- and pyruvate-free mechanically degraded MX samples are presented as a function of temperature in Figure 5.18A and B, respectively.

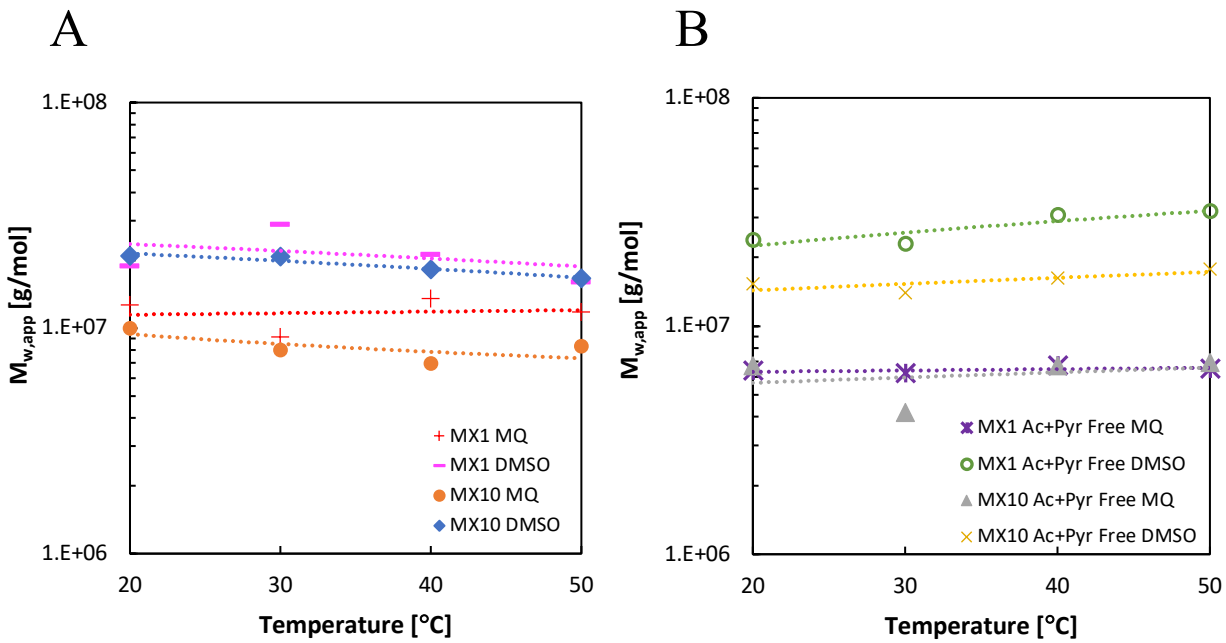

Figure 5.18: Apparent molecular weight ($M_{w,app}$) determined by light scattering as a function of temperature for native (A) and acetate- and pyruvate-free (B) mechanically degraded MX samples.

From Figure 5.18A and B it can readily be seen that the apparent molecular weights obtained by LS are far more extensive than the molecular weights obtained by SEC-MALS, an issue which will be discussed in section 5.2.4. Further, it can be observed that the molecular weights of all samples are almost independent of temperature in the measured temperature range, independent of the solvent. This may suggest that a thermal order-disorder transition has not occurred in the measured temperature range, as lower molecular weights thus would be observed.

Comparing the effect of the two solvents in general; dissolution in DMSO provides a higher $M_{w,app}$ compared to the same sample dissolved in MQ-water, indifferent of the acetate- and pyruvate-content. If xanthan was disordered in DMSO, a lower, rather than a higher molecular weight would be expected. Thus, xanthan does not seem to be disordered in DMSO. DMSO does, however, seems to increase the tendency of aggregation, causing the molecular weight of xanthan to be larger compared to dissolution in MQ-water. The tendency of aggregation in DMSO seems to be more significant for acetate-and pyruvate-free xanthan samples.

Similar observations are also made from the apparent radii of gyration of all samples, presented in Figure 5.19A and B as a function of temperature for native and acetate-and pyruvate-free samples.

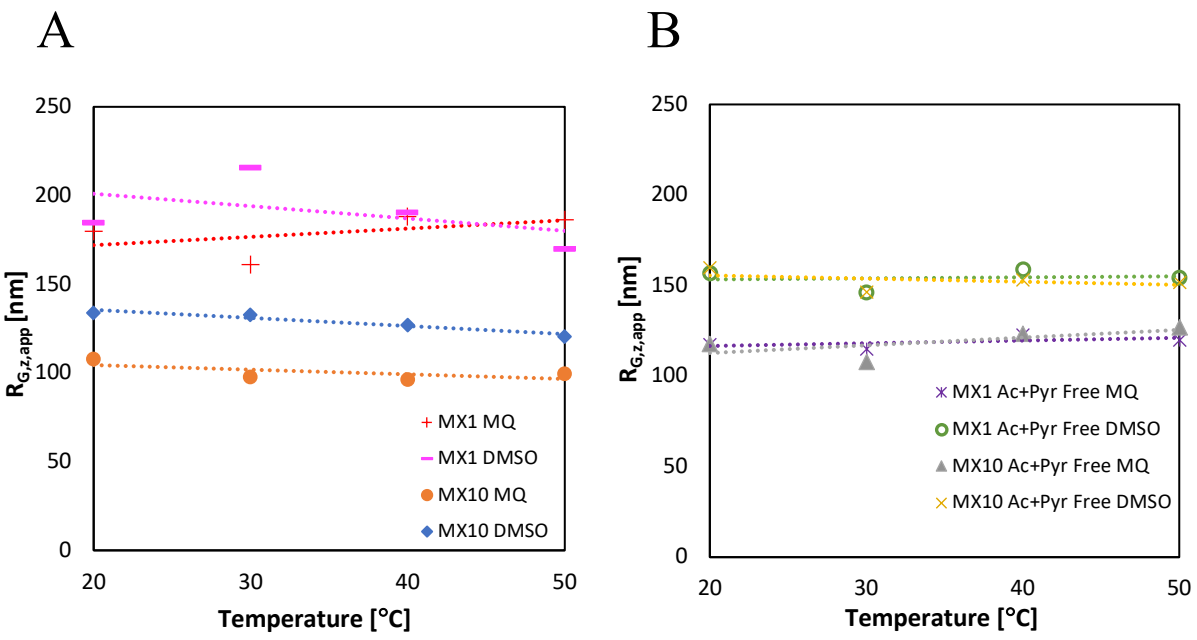

Figure 5.19: The apparent z-average radius of gyration ($R_{G,z,app}$) determined by light scattering as a function of temperature for native (A) and acetate- and pyruvate- free (B) mechanically degraded MX samples.

From Figure 5.19A and B, the apparent molecular weight, the $R_{G,z,app}$ of all samples seems to be independent of temperature, similar to what was seen for the apparent molecular weight. This observation strengthens the anticipation that no thermal order-disorder transition takes place in the measured temperature range, despite no presence of additional salt in the sample. T_m of sodium xanthan in pure aqueous solution has previously been shown to be around 36°C [84] Thus, order-disorder was expected to take place in the measured temperature range. However, thermal order-disorder transition could have been prevented by the ionic strength of xanthan itself, which is known to influence T_m for high xanthan concentrations [31]. The increased stability of H^+-xanthan towards higher temperatures compared to Na^+-xanthan could also explain the lack of an order-disorder transition [34].

Figure 5.19A furthermore shows that dissolution in DMSO results in larger $R_{G,z,app}$ compared to dissolution in MQ-water, indicating larger molecules. These findings show no sign of xanthan being in its disordered state in DMSO as lower radii would be expected due to more compact molecules. The sizable values of $R_{G,z,app}$ suggest that aggregation taking place in the samples. As an attempt to overcome the potential formation of aggregates, SLS could be performed at a lower concentration.

5.2.3.3 Dynamic Light Scattering

The hydrodynamic radii were determined by applying Equation (3-29) on data obtained from CONTIN. The results are presented in Figure 5.20 as a function of temperature.

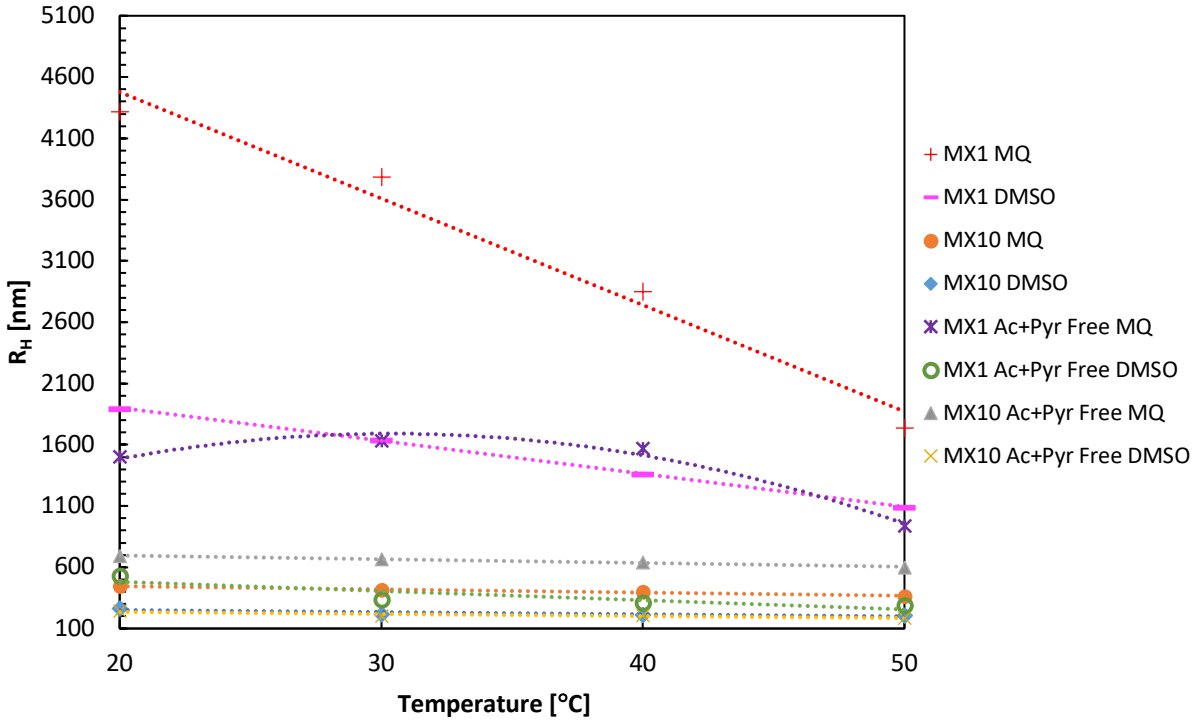

Figure 5.20: The hydrodynamic radius (R_H) for all samples analysed by light scattering, presented as a function of temperature.

From Figure 5.20, the hydrodynamic radius of both native MX_1 dissolved in MQ-water and DMSO show a temperature dependency, decreasing linearly with increasing temperature. R_H of acetate- and pyruvate-free MX_1 in MQ-water, also shows a temperature dependency. However, it decreases first after 40°C. The decreasing hydrodynamic volume may suggest that a thermal order-disorder transition occur. This anticipation is, however, rather unlikely given the SLS results. The temperature dependency might be explained by the formation of aggregates, which are known to resolve as temperature increases. Hence, a decrease in R_H is observed. Another explanation for the temperature dependency might be the delimitation of DLS, which is a recommended method if R_H is found to be between 1 and 1000 nm [65]. The high values obtained for MX_1 could thus be overestimated with a significant error, which might introduce the observed temperature dependency. Thus, DLS might not be suitable for analysing R_H for higher molecular weight samples such as MX_1.

The R_H obtained for the remaining samples, show no sign of temperature dependency throughout the measured temperature range, suggesting that no order-disorder transition occur. The obtained values of R_H for these samples are also significantly lower, i.e. between 200 and 700 nm, compared to the $R_{H,app}$ of the MX_1 samples showing temperature dependency, which

have values ranging from 1100 to 4500 nm. This observation also strengthens the suggestion that the temperature dependency is caused by an overestimation of the R_H of the MX_1.

5.2.3.4 Evaluation of Conformation

In order to get a better understanding of the conformation of the MX samples analysed by LS, a RMS conformation-plot were constructed from the apparent $R_{G,z}$ and M_w values. LS data for xanthan in aqueous sodium solution obtained by Sato *et al.* were included as a reference for optimal conformation [11]. The RMS conformation-plot is presented in Figure 5.21.

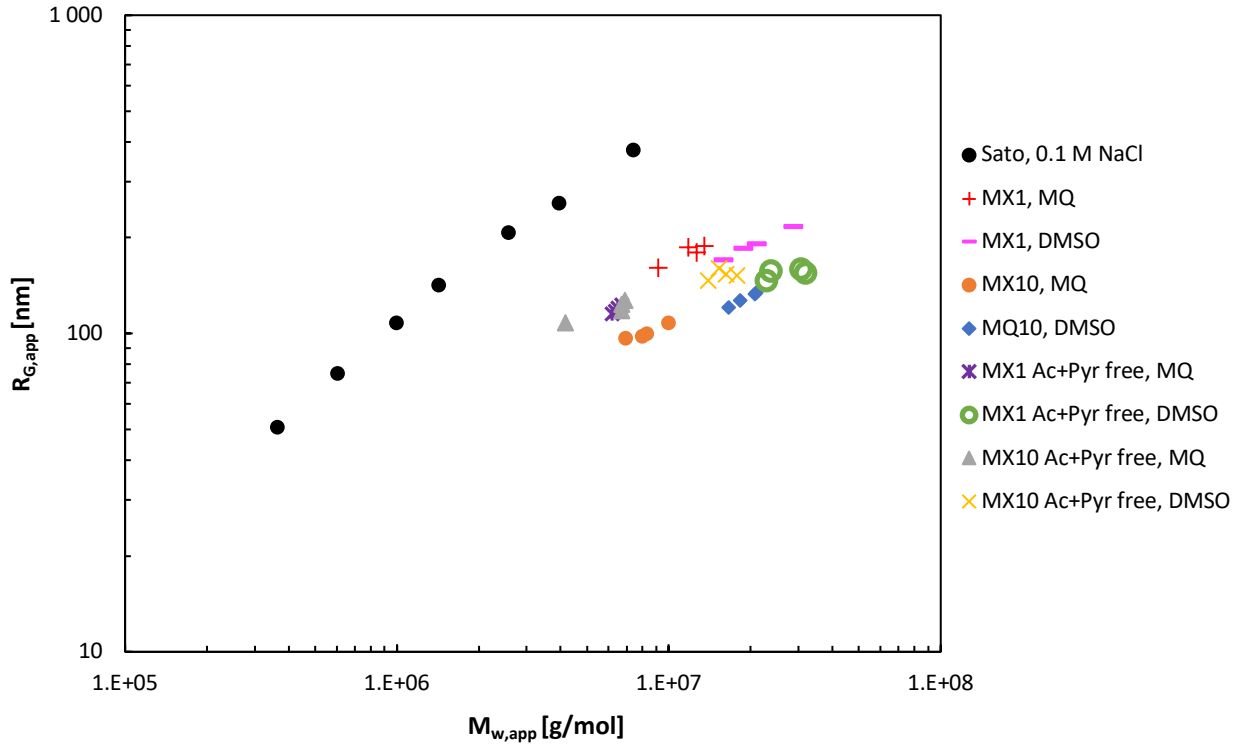

Figure 5.21: RMS-conformation-plot of the data obtained for the different mechanically degraded MX samples by light scattering (LS). Data published for xanthan in 0.1 M NaCl by Sato *et al* is included as a reference for optimal conformation [11].

From Figure 5.21 it can readily be observed that all mechanically degraded MX samples have a lower radius of gyration compared to the corresponding molecular weight of the reference sample, suggesting that they obtain a more flexible conformation compared to rigid rods in both water and DMSO. However, due to the high molecular weight independent of the solvent used, the samples are likely not to be disordered. Instead, aggregation might be the cause of the high molecular weights.

5.2.4 Comparison of Light Scattering- and SEC-MALS Data

Analysis of M_w and $R_{G,z}$ by LS showed values significantly different from M_w and $R_{G,w}$ obtained by SEC-MALS. The molecular characteristics obtained by the two analytical methods are summarised in Table 5.4 to provide an overview for comparison. The LS data presented were extracted from measurements performed in MQ-water at 20°C. Note that these values also are apparent values as only one concentration was analysed.

Table 5.4: Comparison of the molecular characteristics obtained by SEC-MALS and light scattering (LS). Both methods provide the weight average molecular weight, M_w, while SEC-MALS and LS provide the weight average and the z-average radius of gyration, $R_{G,w}$ and $R_{G,z}$, respectively. The SEC-MALS eluent used was 0.15 M $NaNO_3$ and 0.01 M EDTA, pH 6, and measurements were performed at room temperature. The presents LS data is extracted from measurements performed in MQ-water at 20°C and are apparent values as only one concentration was analysed.

	SEC-MALS		Light Scattering	
Sample name	**M_w [kDa]**	**$R_{G,w}$ [nm]**	**$M_{w,app}$ [kDa]**	**$R_{G,z,app}$ [nm]**
H^+-MX_1	938	106	12 600	180
H^+-MX_1, Ac+Pyr free	688	96	6 400	118
H^+-MX_{10}	507	49	9 900	108
H^+-MX_{10}, Ac+Pyr free	230	38	6 700	117

From Table 5.4 it can be observed that the molecular weights obtained by LS are, in most cases, ten times larger than M_w obtained by SEC-MALS, while $R_{G,z,app}$ is almost twice the values presented for $R_{G,w}$. The values from LS are apparent; however, the significant difference is likely not caused by this, as extrapolation towards zero concentration, i.e. inclusion of A_2, would cause both $R_{G,z}$ and M_w to become even greater. The vast difference in the values obtained by LS and SEC-MALS may suggest that aggregation occurs during light scattering, an issue that might be overcome by reducing the polymer concentration analysed. Aggregation may not occur to the same degree during SEC-MALS due to the high shear forces of the SEC-column. Thus, the values obtained by SEC-MALS most certain represent the correct molecular weight and radius of gyration of each sample.

The difference in the radius of gyration could also be explained by the average they represent. LS provides the z-average radius of gyration, which is known to be more affected by larger molecules, compared to the weight average radius of gyration obtained by SEC-MALS [40]. Thus, if aggregation occurs, $R_{G,z}$ would increase to a greater extent than $R_{G,w}$.

6 Conclusion

In this work, MX, mechanically degraded by high shear forces, were characterised to establish a protocol of mechanical degradation that prevents order-disorder transitions during degradation from taking place. Characterisation of the mechanically degraded samples by SEC-MALS-VISC indicated a higher shape parameter for samples degraded with 0.5 M $MgSO_4$ compared to samples degraded with 0.1 M NaCl and 0.5 M NaCl and thus lower ionic strength, which implies a more rigid conformation of the 0.5 M $MgSO_4$ sample. Hence, when it is desired to keep the ordered conformation of xanthan intact during mechanical degradation by high shear forces, high ionic strength should be applied.

Given the findings of the effect of ionic strength on conformation during mechanical degradation by high shear forces, new samples were prepared, and desalting by dialysis was initiated to purify the samples. Different salt-forms were prepared, depending on the dialysis media, i.e. pure water, aqueous sodium solution and acidic water. By SEC-MALS-VISC analysis, it was found that mechanical degradation by high shear forces is reproducible in terms of reducing molecular weight, the radius of gyration and intrinsic viscosity, as the results were similar to previously obtained values. The SEC-MALS-VISC analysis also indicated that the different salt-forms obtained by dialysis influences the conformation of the samples: Mg^{2+} as counterions give a more ideal, rigid conformation compared to Na^+ and H^+. Comparison of the characteristic of purified Mg^{2+}-xanthan with the non-purified sample degraded with 0.5 M $MgSO_4$ implies a slightly less rigid conformation after desalting. The conformation is, however, not substantially changed, i.e. full order-disorder transitions are not introduced, suggesting dialysis to be an appropriate method for desalting.

Acetate and pyruvate were removed form a fraction of the mechanically degraded MX and 0614-3 and ^{1}H-NMR confirmed the removal of substituents. Analysis of their characteristic by SEC-MALS-VISC, implied samples with improved, rigid conformations compared to their native samples. The improvement of conformation might be explained by the mild acid- and/or alkaline hydrolysis step in the preparation procedure of acetate- and pyruvate-free xanthan, dissolving potential aggregates in the sample.

The mechanically degraded samples were further used to study the conformation of acidic xanthan in water, pure DMSO and water/DMSO mixtures, to confirm a possible disorder in

DMSO and determine at which fraction of DMSO the disorder occur. Acidic xanthan (both native and acetate- and pyruvate-free) was found to be directly soluble in DMSO. No heating was needed for dissolution, which previously has been reported.

The ellipticity of both native and acetate- and pyruvate free mechanically degraded MX in MQ-water was found to decrease linearly with increasing temperature, from CD. A negative sigmoidal curve would have been expected for the ellipticity with increasing temperature if order-disorder transitions occurred. Hence, the findings suggest that neither of the samples undergoes full order-disorder transitions in the measured temperature interval, 20 to 90°C and are thus not it the disordered state for any of the temperatures. The increased stability of H^+-xanthan towards higher temperatures compared to Na^+-xanthan, likely explains the lack of order-disorder transitions. CD in DMSO was found to be impossible, likely due to the high absorption of light into DMSO at the analysed wavelength. The issue raises a question to the CD spectra of xanthan in DMSO obtained by Fantou *et al.*, and their conclusion that xanthan is in its disordered state in DMSO.

Nevertheless, structural changes of xanthan were detected 80 w/w%, DMSO by optical rotation and solution viscosity. An order-disorder transition might have caused the detected changes. Hence, f_{DMSO} was determined to be 0.8; however, it might be dependent on both the acetate and pyruvate content, as well as the molecular weight of the sample.

Given the finding of f_{DMSO}, further analysis of xanthan in DMSO was done by light scattering. Neither the molecular weights nor the radii of gyration of the samples analysed were found to be dependent on temperature, indicating that no thermal order-disorder transition takes place in the measured temperature range, 20-50°C. A thermal order-disorder transition might have been prevented by the ionic strength of xanthan itself or by the increased stability of H^+-xanthan compared to Na^+-xanthan. The samples dissolved in DMSO, in general, have higher apparent molecular weights and radii of gyration compared to samples dissolved in MQ-water. As lower molecular weights would be expected for disordered structures, this finding may suggest that xanthan does not become disordered in DMSO.

7 Recommendations

To further optimise the procedure for mechanical degradation, it could be attempted to investigate the effect on conformation of lowering the gauge pressure and increase the number of runs through Star Burst Mini. This may also allow for the ionic strength during mechanical degradation to be reduced, as the temperature at the site of depolymerisation would likely become lower. The effect on conformation of performing purification by dialysis in a cold environment might also be further investigated.

In order to get a better understanding of the behaviour of xanthan in DMSO, light scattering measurements at lower concentration should be initiated. This would likely decrease the tendency of aggregation and thus provide more correct values of the molecular weight and radius of gyration. SEC-MALS-VISC could also be used to evaluate xanthan in DMSO, however, another SEC-column might be needed.

Instead of circular dichroism, optical rotation, which is independent of the absorption wavelength, in DMSO should be applied with temperature scan. This could provide a better understanding of the behaviour of xanthan in DMSO and thus possible order-disorder transitions. Capillary viscometry at elevated temperatures should also be performed, as increased temperature makes xanthan more susceptible for disorder to occur. Measurements at a narrower step length of w/w% DMSO should also be performed to determine f_{DMSO} more specifically.

Bibliography

1. Christensen, B.E., *Biopolymers*. Vol. V. 2018, Trondheim: NTNU.
2. Rellegadla, S., G. Prajapat, and A. Agrawal, *Polymers for enhanced oil recovery: fundamentals and selection criteria.* Applied Microbiology and Biotechnology, 2017. **101**(11): p. 4387 DOI: 10.1007/s00253-017-8307-4.
3. Moffat, J., et al., *Visualisation of xanthan conformation by atomic force microscopy.* Carbohydrate Polymers, 2016. **148**: p. 380-389 DOI: 10.1016/j.carbpol.2016.04.078.
4. Matsuda, Y., et al., *Atomic force microscopy of thermally renatured xanthan with low molar mass.* Polymer Journal, 2015. **47**(3): p. 282-285 DOI: 10.1038/pj.2014.102.
5. Matsuda, Y., et al., *Renaturation behavior of xanthan with high molar mass and wide molar mass distribution.* Polymer Journal, 2016. **48**(5): p. 653-658 DOI: 10.1038/pj.2015.128.
6. Milas, M., M. Rinaudo, and B. Tinland, *Comparative depolymerization of xanthan gum by ultrasonic and enzymic treatments. Rheological and structural properties.* Carbohydrate Polymers, 1986. **6**(2): p. 95-107 DOI: 10.1016/0144-8617(86)90037-8.
7. Holzwarth, G., *Conformation of Extracellular Polysaccharide of Xanthomonas-Campestris.* Biochemistry, 1976. **15**(19): p. 4333-4339 DOI: 10.1021/Bi00664a030.
8. Liu, W., et al., *Thermally Induced Conformational Change of Xanthan in 0.01m Aqueous Sodium-Chloride.* Carbohydrate Research, 1987. **160**: p. 267-281 DOI: 10.1016/0008-6215(87)80317-8.
9. Liu, W. and T. Norisuye, *Order-Disorder Conformation Change of Xanthan in 0.01m Aqueous Sodium-Chloride - Dimensional Behavior.* Biopolymers, 1988. **27**(10): p. 1641-1654 DOI: 10.1002/bip.360271009.
10. Kawakami, K., Y. Okabe, and T. Norisuye, *Dissociation of Dimerized Xanthan in Aqueous-Solution.* Carbohydrate Polymers, 1990. **14**(2): p. 189-203 DOI: 10.1016/0144-8617(90)90030-V.
11. Sato, T., T. Norisuye, and H. Fujita, *Double-Stranded Helix of Xanthan - Dimensional and Hydrodynamic Properties in 0.1-M Aqueous Sodium-Chloride.* Macromolecules, 1984. **17**(12): p. 2696-2700 DOI: 10.1021/ma00142a043.
12. Jenssen, I.B. and B.E. Christensen, *Preparation and Characterisation of Hydrophobically Modified Xanthan*. 2014, Institutt for bioteknologi, NTNU.
13. Kojima, T., et al., *Method for a specific depolymerization of a polysaccharide having a rod-like helical conformation*, U.S. Patent, Editor. 1985, Kaken Pharmaceutical Co. Ltd.; Taito Co., Ltd.,.

14. Sugino. *Wet Milling and Dispersing Device "Star Burst Mini"*. 2019 [cited 2019 06.03.19]; Available from: http://www.sugino.com/site/wet-pulverizing-and-dispersing-equipment-e/sbs-type-mini-e.html.

15. Koshland, D.E. and F. Haurowitz. *Protein Denaturation*. 2019 [cited 2019 13.06]; Available from: https://www.britannica.com/science/protein/Protein-denaturation.

16. Kitagawa, H., et al., *Optical-Rotation Behavior of Xanthan in Mixtures of Water and Cadoxen.* Carbohydrate Polymers, 1985. **5**(6): p. 407-422 DOI: 10.1016/0144-8617(85)90002-5.

17. Sato, T., T. Norisuye, and H. Fujita, *Double-Stranded Helix of Xanthan - Dissociation Behavior in Mixtures of Water and Cadoxen.* Polymer Journal, 1985. **17**(5): p. 729-735 DOI: 10.1295/polymj.17.729.

18. Ladisch, C.M., *Cadoxen solvolysis of cellulose*, in *Methods in Enzymology*. 1988, Academic Press. p. 11-19 DOI: 10.1016/0076-6879(88)60102-9.

19. Fantou, C., et al., *Chemical modification of xanthan in the ordered and disordered states: An open route for tuning the physico-chemical properties.* Carbohydrate Polymers, 2017. **178**: p. 115-122 DOI: 10.1016/j.carbpol.2017.09.039.

20. Milas, M. and B. Tinland, *Behaviour of xanthan in cadoxen.* Carbohydrate Polymers, 1990. **13**(1): p. 47-56 DOI: 10.1016/0144-8617(90)90050-3.

21. Osebakken, K.G., B.E. Christensen, and M.Ø. Dalheim, *Xanthan - structural characterisation and effect of xanthan concentration, ionic strength and dissolution procedure during mechanical degradation*. 2018, NTNU.

22. Cadmus, M.C., et al., *Colonial variation in Xanthomonas campestris NRRL B-1459 and characterization of the polysaccharide from a variant strain.* Canadian Journal of Microbiology, 1976. **22**(7): p. 942-948 DOI: 10.1139/m76-136.

23. Candia, J.L.F. and W.D. Deckwer, *Effect of the Nitrogen Source on Pyruvate Content and Rheological Properties of Xanthan.* Biotechnology Progress, 1999. **15**(3): p. 446-452 DOI: 10.1021/bp990028i.

24. Kool, M.M., et al., *Comparison of xanthans by the relative abundance of its six constituent repeating units.* Carbohydrate Polymers, 2013. **98**(1): p. 914-921 DOI: 10.1016/j.carbpol.2013.07.003.

25. Kool, M.M., et al., *The influence of the primary and secondary xanthan structure on the enzymatic hydrolysis of the xanthan backbone.* Carbohydrate Polymers, 2013. **97**(2): p. 368-375 DOI: 10.1016/j.carbpol.2013.05.045.

26. Stokke, B.T., A. Elgsaeter, and O. Smidsrod, *Electron microscopic study of single-and double-stranded xanthan.* International Journal of Biological Macromolecules, 1986. **8**(4): p. 217-225 DOI: 10.1016/0141-8130(86)90030-9.

27. Dumitriu, S., *Polysaccharides : Structural diversity and functional versatility*. 2nd ed. 2004, New York: Marcel Dekker.

28. Whitcomb, P.J., B.J. Ek, and C.W. Macosko, *Rheology of Xanthan Gum Solutions*, in *Extracellular Microbial Polysaccharides*. 1977, American Chemical Society. p. 160-173 DOI: 10.1122/1.549485.

29. Milas, M. and M. Rinaudo, *Conformational Investigation on the Bacterial Polysaccharide Xanthan.* Carbohydrate Research, 1979. **76**(Nov): p. 189-196 DOI: 10.1016/0008-6215(79)80017-8.

30. Holzwarth, G. and J. Ogletree, *Pyruvate-Free Xanthan.* Carbohydrate Research, 1979. **76**(Nov): p. 277-280 DOI: 10.1016/0008-6215(79)80030-0.

31. Matsuda, Y., Y. Biyajima, and T. Sato, *Thermal Denaturation, Renaturation, and Aggregation of a Double-Helical Polysaccharide Xanthan in Aqueous Solution.* Polymer Journal, 2009. **41**(7): p. 526-532 DOI: 10.1295/Polymj.Pj2008300.

32. Yasuhiro, M., et al., *Renaturation behavior of xanthan with high molar mass and wide molar mass distribution.* Renaturation behavior of xanthan with high molar mass and wide molar mass distribution, 2016. **48**(5): p. 653-658 DOI: 10.1038/pj.2015.128.

33. Zhang, L., et al., *Double-Stranded Helix of Xanthan - Rigidity in 0.01m Aqueous Sodium-Chloride Containing 0.01 N-Hydrochloric Acid.* Biopolymers, 1987. **26**(3): p. 333-341 DOI: 10.1002/bip.360260303.

34. Christensen, B.E. and O. Smidsrød, *Hydrolysis of xanthan in dilute acid: Effects on chemical composition, conformation, and intrinsic viscosity.* Carbohydrate Research, 1991. **214**(1): p. 55-69 DOI: 10.1016/S0008-6215(00)90530-5.

35. Christensen, B.E., M.H. Myhr, and O. Smidsrød, *Degradation of double-stranded xanthan by hydrogen peroxide in the presence of ferrous ions: comparison to acid hydrolysis.* Carbohydrate Research, 1996. **280**(1): p. 85-99 DOI: 10.1016/0008-6215(95)00289-8.

36. Bradshaw, I.J., et al., *Modified xanthan—its preparation and viscosity.* Carbohydrate Polymers, 1983. **3**(1): p. 23-38 DOI: 10.1016/0144-8617(83)90010-3.

37. Christensen, B.E., *Conformation-stability relationships in xanthan gum*. 1996, Norwegian University of Science and Technology: Trondheim.

38. Shrivastava, A., *Polymerization*, in *Introduction to Plastics Engineering*. 2018, William Andrew Publishing. p. 17-48 DOI: 10.1016/B978-0-323-39500-7.00002-2.

39. *Weight-average molecular weight*, in *Encyclopedic Dictionary of Polymers*, J.W. Gooch, Editor. 2007, Springer New York: New York, NY. p. 1063-1063 DOI: 10.1007/978-0-387-30160-0_12520.

40. *Z-Average molecular weight*, in *Encyclopedic Dictionary of Polymers*, J.W. Gooch, Editor. 2007, Springer New York: New York, NY. p. 1083-1083 DOI: 10.1007/978-0-387-30160-0_12733.

41. Stepto Robert, F.T., *Dispersity in polymer science (IUPAC Recommendations 2009)*, in *Pure and Applied Chemistry*. 2009. p. 351.DOI: 10.1351/PAC-REC-08-05-02.

42. Bloomfield, V.A., et al., *Laser light scattering in biochemistry* Special publication (Royal Society of Chemistry (Great Britain)) ; no. 99. 1992, Cambridge, England: Royal Society of Chemistry.

43. Sugino. *Various types of chambers for "Star Burst"*. 2019 [cited 2019 06.03.19]; Available from: http://www.sugino.com/site/qa-e/sbs-techinical-chamber-e.html#ball.

44. Balcıi, M., *Basic 1H- and 13C-NMR spectroscopy*. 2005, Elsevier: Amsterdam ;,Boston.

45. Morris, E.R., et al., *Order-disorder transition for a bacterial polysaccharide in solution. A role for polysaccharide conformation in recognition between Xanthomonas pathogen and its plant host.* Journal of Molecular Biology, 1977. **110**(1): p. 1-16 DOI: 10.1016/S0022-2836(77)80095-8.

46. Rinaudo, M., et al., *1 H and 13 C NMR Investigation of Xanthan Gum.* Macromolecules, 1983. **16**(5): p. 816-819 DOI: 10.1021/ma00239a018.

47. Holmvik, C., B.E. Christensen, and M.Ø. Dalheim, *Depolymerisation and Characterisation of Xanthans - A study of rheological and structural properties for Enhanced Oil Recovery*. 2018, NTNU.

48. Paar, A. *Basics of viscometry*. 2019 [cited 2019 24.05]; Available from: https://wiki.anton-paar.com/en/basic-of-viscometry/#c16584.

49. Katzbauer, B., *Properties and applications of xanthan gum.* Polymer Degradation and Stability, 1998. **59**(1): p. 81-84 DOI: 10.1016/S0141-3910(97)00180-8.

50. Irgens, F., *Rheology and Non-Newtonian Fluids*. 2013: Springer International Publishing.

51. Rudin, A. and P. Choi, *The Elements of Polymer Science and Engineering*. 2013 DOI: 10.1016/C2009-1-64286-6.

52. Wilke, J., et al., *Theory and Praxis of Capillary Viscometry*

53. Huggins, M.L., *The Viscosity of Dilute Solutions of Long-Chain Molecules. IV. Dependence on Concentration.* Journal of the American Chemical Society, 1942. **64**(11): p. 2716-2718 DOI: 10.1021/ja01263a056.

54. Gergely, A., *A review of the application of chiroptical methods to analytical chemistry.* Journal of Pharmaceutical and Biomedical Analysis, 1989. **7**(5): p. 523-541 DOI: 10.1016/0731-7085(89)80218-3.

55. *An introduction to circular dichroism spectroscopy*. 2019 [cited 2019 12.03]; Available from: https://www.chem.uci.edu/~dmitryf/manuals/Fundamentals/CD%20spectroscopy.pdf.

56. Berova, N., et al., *Comprehensive Chiroptical Spectroscopy: Instrumentation, Methodologies, and Theoretical Simulations*. 2011: Wiley.

57. Eliel, E.L. and S.H. Wilen, *Stereochemistry of Organic Compounds*. 2008: Wiley India Pvt. Limited.

58. Paar, A., *Instruction Manual and Safety Information Modular Circular Polarimeter*. 2018.

59. Pecora, R., *Dynamic Light Scattering: Applications of Photon Correlation Spectroscopy*. 2013: Springer US.

60. Schreiber, F. *Static and Dynamic Light Scattering (SLS/DLS)*. 2019 [cited 2019 12.03]; Available from: http://www.soft-matter.uni-tuebingen.de/index.html?dls.html.

61. Instruments, L. *Dynamic Light Scattering*. 2019 [cited 2019 13.03]; Available from: https://lsinstruments.ch/en/technology/dynamic-light-scattering-dls.

62. Borsali, R. and R. Pecora, *Soft-Matter Characterization*. 2008: Springer Netherlands.

63. Scotti, A., et al., *The CONTIN algorithm and its application to determine the size distribution of microgel suspensions.* The Journal of Chemical Physics, 2015. **142**(23) DOI: 10.1063/1.4921686.

64. Instruments, L. *Statical Light Scattering*. 2019 [cited 2019 16.05]; Available from: https://lsinstruments.ch/en/technology/static-light-scattering-sls.

65. Øgendal, L., *Light Scattering a brief introduction*. 2019: University of Copenhagen.

66. Wyatt, P.J., *Light scattering and the absolute characterization of macromolecules.* Analytica Chimica Acta, 1993. **272**(1): p. 1-40 DOI: 10.1016/0003-2670(93)80373-S.

67. Shi, L., et al., *Control over the electrostatic self-assembly of nanoparticle semiflexible biopolyelectrolyte complexes-Supporting Information.* Soft Matter, 2013. **9**(20): p. 5004-5015 DOI: 10.1039/C3SM27138B.

68. Foundation., Y.S.o.M.-W.M.K. *HPLC Size Exclusion Chromatography/Laser Light Scattering Determination of Native Protein Molecular Weights.* 2018; Available from: https://medicine.yale.edu/keck/biophysics/technologies/lightscatter/dataset.aspx.

69. Kuwana, T., *Physical Methods in Modern Chemical Analysis*. 2012: Elsevier Science.

70. Debye, P.P., *A Photoelectric Instrument for Light Scattering Measurements and a Differential Refractometer.* Journal of Applied Physics, 1946. **17**(5): p. 392-398 DOI: 10.1063/1.1707729.

71. Pittz, E.P., et al., *Light scattering and differential refractometry*, in *Methods in Enzymology*. 1973, Academic Press. p. 209-256 DOI: 10.1016/S0076-6879(73)27012-X.

72. Rudin, A. and P. Choi, *Practical Aspects of Molecular Weight Measurements-Chapter 3*. 1999: Elsevier Inc. 73-120 DOI: 10.1016/B978-012601685-7/50003-3.

73. Technology, W. *Polymer characterization: viscosity is intrinsic*. 2019 [cited 2019 28.01]; Available from: https://www.wyatt.com/blogs/polymer-characterization-viscosity-is-intrinsic.html.

74. Elgsæter, A., et al., *Depolymerization of double-stranded xanthan by acid hydrolysis : characterization of partially degraded double strands and single-stranded oligomers released from the ordered structures*. 1993, Washington: American Chemical Society.

75. Brayton, C., *Dimethyl sulfoxide (DMSO): a review.* Cornell Vet., 1986. **76**(1): p. 61-90.

76. Rinaudo, M., et al., *Proton and carbon-13 NMR investigation of xanthan gum.* Macromolecules, 1983. **16**(5): p. 816-819 DOI: 10.1021/ma00239a018.

77. Shatwell, K.P., et al., *The influence of acetyl and pyruvate substituents on the helix-coil transition behaviour of xanthan.* Carbohydrate Research, 1990. **206**(1): p. 87-103 DOI: 10.1016/0008-6215(90)84009-J.

78. Rinaudo, M., et al., *Physical properties of xanthan, galactomannan and their mixtures in aqueous solutions.* Macromolecular Symposia, 1999. **140**: p. 115-124 DOI: 10.1002/masy.19991400113.

79. Marcovicz, C., et al., *Nonlinear optical behavior of two tetrathiafulvalene derivatives in the picosecond regime.* Chemical Physics Letters, 2018. **702**: p. 16-20 DOI: 10.1016/j.cplett.2018.04.053.

80. Kitamura, S. and T. Kuge, *A differential scanning calorimetric study of the conformational transitions of schizophyllan in mixtures of water and dimethylsulfoxide.* Biopolymers, 1989. **28**(2): p. 639-654 DOI: 10.1002/bip.360280208.

81. Stahl, G.A. and D.N. Schulz, *Water-Soluble Polymers for Petroleum Recovery*. 2012: Springer US DOI: 10.1007/978-1-4757-1985-7.

82. Tao, Y. and L. Zhang, *Determination of molecular size and shape of hyperbranched polysaccharide in solution.* Biopolymers, 2006. **83**(4): p. 414-423 DOI: 10.1002/bip.20572.

83. Tada, T., et al., *Network structure of curdlan in DMSO and mixture of DMSO and water.* Biopolymers, 2001. **58**(2): p. 129-137 DOI: 10.1002/1097-0282(200102)58:2<129::AID-BIP20>3.0.CO;2-Z.

84. Brunchi, C.-E., et al., *Some properties of xanthan gum in aqueous solutions: effect of temperature and pH.* Journal of Polymer Research, 2016. **23**(7): p. 123 DOI: 10.1007/s10965-016-1015-4.

Appendices

A Concentration Testing, Circular Dichroism

In order to find the optical concentration for circular dichroism, solutions of 0.1, 0.3, 0.5 and 1 w/w% H^+-MX_{10}/MQ-water was prepared and analysed at a wavelength of 215 nm from 10-90°C using a Jasco J-720WO Spectropolarimeter. Quartz cells of 5 mm were used for 0.1 and 0.3 w/w% samples, whereas the 0.5 and 1 w/w% solutions were measured in 2- and 1-mm quartz cells, respectively, in order to avoid high voltage and thus poor signal. The same quartz cells were used to determine the baseline, i.e. CD of pure solvent. The bandwidth was set to 1 nm and the rate of heating to 2°C/min for all measurements.

The measured ellipticity at each temperature corrected for concentration and optical pathlength by applying Equation (3-24), and plotted as a function of temperature. The baseline was subtracted before the correction. The plot is presented in Figure A.

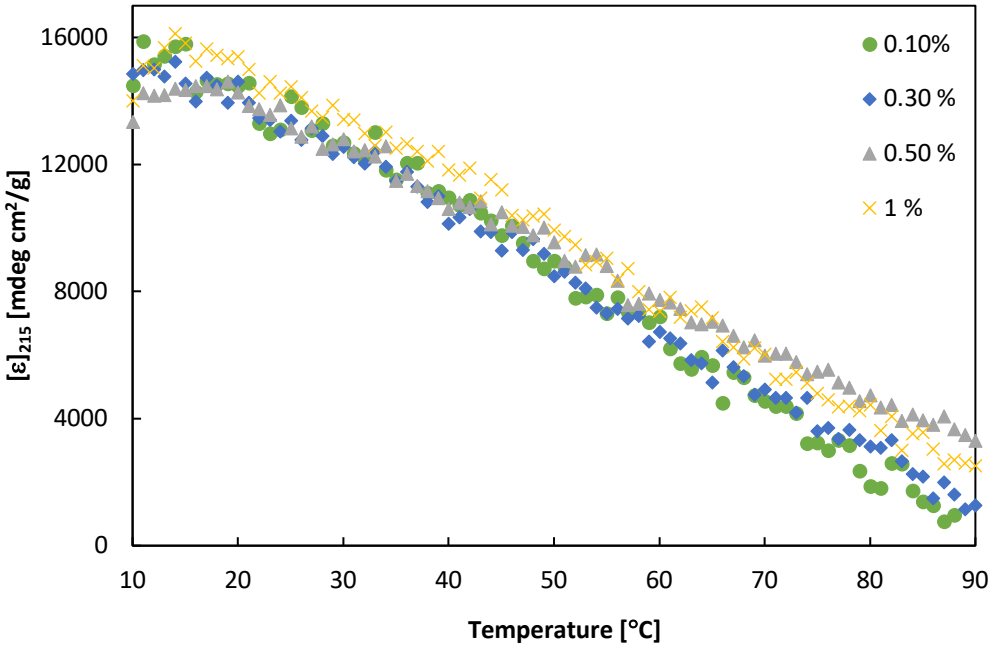

Figure A: Circular dichroism temperature scan of H^+-MX_{10} in MQ-water for determination of optimal concentration for further analysis

From Figure A it can be observed that all concentrations follow approximately the same trend as a function of temperature. Given this observation all further CD measurements were performed at 0.1% xanthan/solvent.

B SEC-MALS-VISC Elution Profiles

To obtain samples of various molecular weight, MX were mechanically degraded by high shear forces at 1 mg/mL MX, 0.5 M $MgSO_4$ by Star Burst Mini one and 10 times. The degraded samples were purified by dialysis, which generated various salt forms, depending on the dialysis media. This appendix presents the elution profiles and molecular weight distribution obtained by SEC-MALS-VISC of the different salt-forms of MX_1 and MX_{10}. The elution profiles and molecular weight distribution of the acetate- and pyruvate-free versions of the samples are also included.

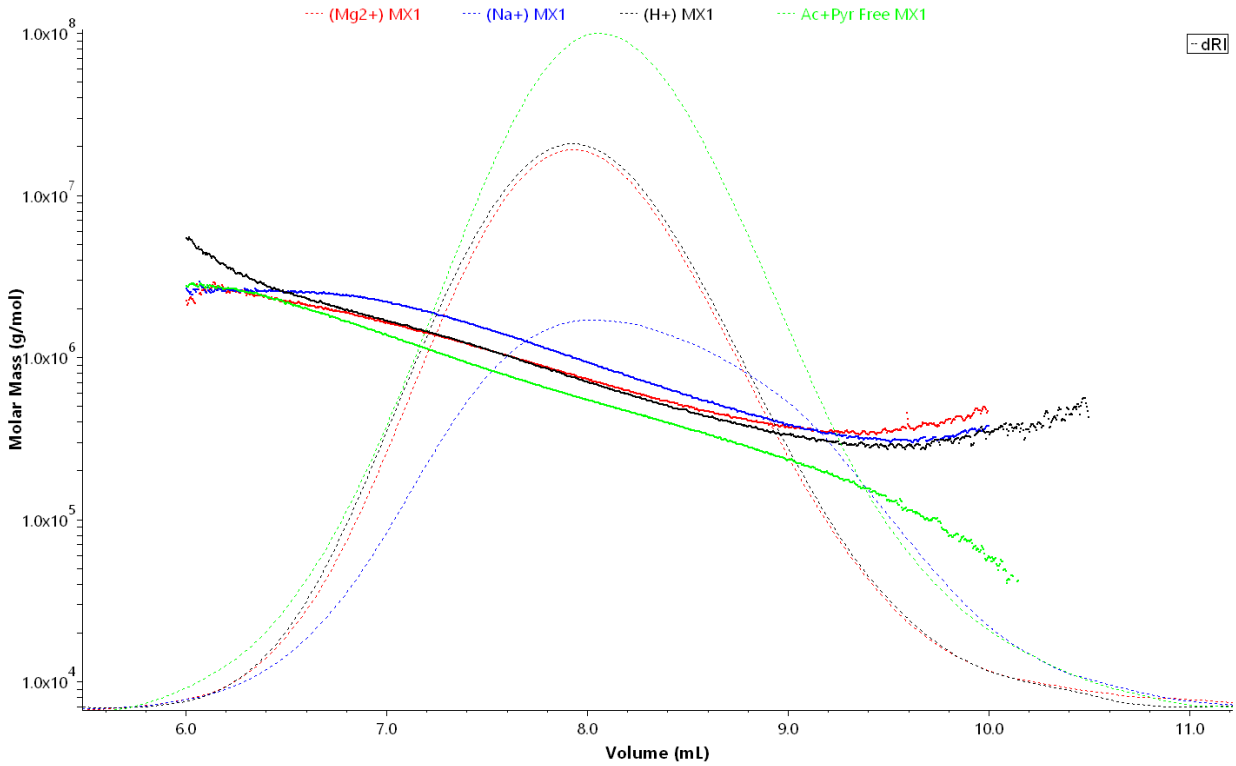

Figure B: Elution profiles and molecular weight distributions of the different salt-forms and acetate- pyruvate-free MX_1. Dashed lines correspond to the differential refractive index signal, scaled relatively against their respective magnitudes. The squared dotted lines represent molecular weight.

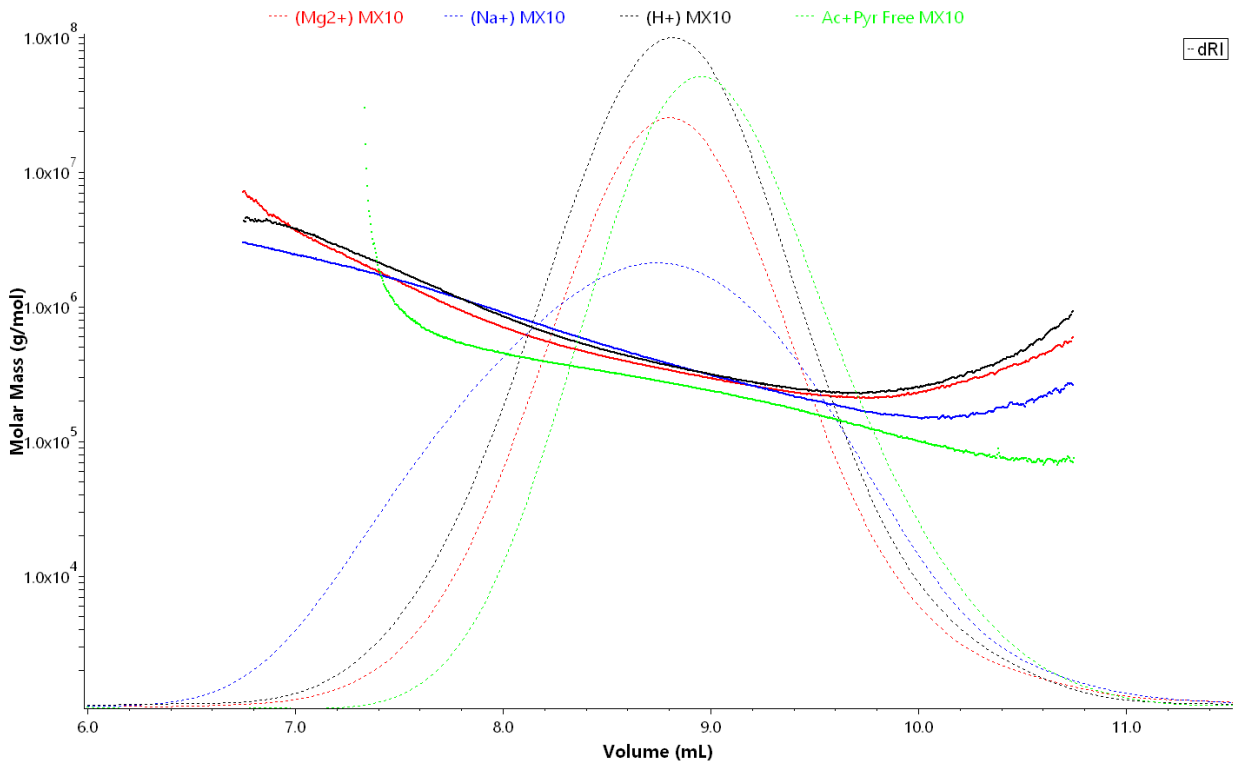

Figure C: Elution profiles and molecular weight distributions of the different salt-forms and acetate- pyruvate-free MX_{10}. Dashed lines correspond to the differential refractive index signal, scaled relatively against their respective magnitudes. The squared dotted lines represent molecular weight.

C Macromolecular Properties From Literature

The macromolecular properties of Na^+-xanthan published by Sato *et al* are presented in Table A [11]. The values were used to evaluate the conformation of MX and 0614-3 XCD studied by SEC-MALS-VISC and light scattering.

Table A: Weight average molecular weight (M_w), intrinsic viscosity ([η]) and z-average radius of gyration $R_{G,z}$ from article by Sato *et al* [11].

Sample name	M_w [Da]	[η] [mL/g]	$R_{G,z}$ [nm]
X4-5	7 400 000	9 000	378
X5-6	3 940 000	5 110	257
X5-8	2 560 000	3 580	208
X-3-5	1 420 000	1 800	142
X9-3	994 000	1 010	108
X7-3h	603 000	575	74.8
C6-3-7	362 000	320	50.8
X6-4-4	240 000	181	36.3
X10-4	209 000	152	34
X6-4-7	164 000	106	25.1
X8-3-5	112 000	61	16.6
X8-3-8	74 000	35	10.8

D Trial and Error - Chirascan Optical Rotation

Originally, a Photophysics Chirascan Series with optical rotatory dispersion accessory was supposed to be used for the optical rotation measurements, due to its ability to include temperature scans and thus detect the melting temperature, T_m. However, the Chirsacan Optical rotation device had not been used in several years and provided a lot of noise in the initial test measurements, giving an indication that something was wrong. Not knowing the exact optical rotation spectrum of the xanthan samples, scans were conducted using a solution of bovine serum albumin (BSA), a protein with a wide known optical rotation spectrum, in order to confirm the noise detected in the xanthan samples. Optical rotation of the BSA solution also proved to have a lot of noise, and the obtained spectra was not as expected, suggesting that calibration was of. The Chirascan device was attempted calibrated using a 100 mg/mL sucrose-water solution at 663°, as described in the Chirascan optical rotation manual, yet without any improvements in the measurements. At last, the support service at Photophysics Chirascan was contacted and provided a new method for zero setting and calibration. Unfortunately, the obtained spectra after calibration were similar to the initial ones, suggesting that there might be something wrong with the optical rotation device. Optical rotation was thus further performed using an Anton Paar Modular Circular Polarimeter fixed at 25°C.

E Capillary Viscometry Raw Data

To determine the reduced viscosity of xanthan samples in mixtures of MQ-water and DMSO, capillary viscometry. Purified H^+-MX_{10} and native and acetate- and pyruvate-free H^+-0614-3 XCD were dissolved directly in solvents containing different fractions of DMSO and stirred overnight. The samples were transferred directly to the capillary viscometer without filtration in order to avoid a possible change in concentration due to absorption of xanthan to the filter.

The flow-through times was measured five to six times for each the xanthan sample and its solvent, before the average was calculated. The flow-through times for the solvents are presented in Table B. The flow-through times of the samples are presented in Table C to Table E. The calculated arithmetic average and Hagenbach Correction Time (t_H) are listed below the measured flow-through times. t_H were calculated by applying Equation (3-19). The correction parameter of the capillary viscometer used (E^*/H^*) were 1000, determined form the operation instruction of the viscometer. MX_{10} were measured at a concentration of 1 mg/mL, while native and acetate- and pyruvate free 0614-3 XCD samples were measured at 0.5 mg/mL.

Table B: Flow-through times for solvents used to determine the reduced viscosity. The arithmetic average and the Hagenbach Correction Time (t_H) are presented in the two lower rows.

	Measured low-through time [s]						
w/w% DMSO	**0**	**10**	**20**	**30**	**40**	**50**	**60**
	82.02	108.04	132.63	153.73	193.75	262.14	291.43
	81.97	108.23	132.79	153.6	193.88	262.4	292.44
	81.99	108.19	132.22	153.55	193.63	262.77	291.77
	82.01	108.63	132.81	153.57	193.55	262.37	292.33
	81.99	108.22	132.93	153.65	193.62	262.31	291.5
	82.03	108.22	132.82	153.55	193.49	261.83	292.38
Average	**82.00**	**108.26**	**132.70**	**153.61**	**193.65**	**262.30**	**291.96**
t_H	0.149	0.085	0.057	0.042	0.027	0.015	0.012

	Measured flow-through time [s]						
w/w% DMSO	**70**	**80**	**85**	**90**	**95**	**97.5**	**100**
	313.2	305.86	253.73	220.91	206.57	177.15	179.17
	313.18	305.98	253.42	220.95	206.57	177.82	179.11
	313.33	305.61	253.41	220.9	206.61	177.36	179.42
	313.16	305.65	253.38	220.91	206.58	177.28	179.47
	313.11	305.79	253.45	220.85	206.59	177.24	179.28
	313.13	305.65		220.81		177.58	179.43
Average	**313.19**	**305.76**	**253.48**	**220.89**	**206.58**	**177.41**	**179.31**
t_H	0.010	0.011	0.016	0.020	0.023	0.032	0.031

Table C: Flow-through times for H^+-MX_{10} in solvents containing various fractions of MQ-water and DMSO. The arithmetic average and the Hagenbach Correction Time (t_H) are presented in the two lower rows. The flow-through times were measured at 1 mg/mL.

	Flow-through time [s]						
w/w% DMSO	**0**	**10**	**20**	**30**	**40**	**50**	**60**
	147.86	190.54	218.5	259.52	316.42	419.58	433.6
	147.21	190.54	218.49	259.54	315.6	419.84	433.38
	147.25	190.35	218.18	259.51	315.14	419.75	433.43
	147.94	190.37	218.08	259.55	316.59	419.4	433.36
	148.12	190.46	218.05	259.54	315.43	419.26	433.26
Average	147.676	190.452	218.26	259.532	315.836	419.566	433.406
t_H	0.046	0.028	0.021	0.015	0.010	0.006	0.005

	Flow-through time [s]			
w/w% DMSO	**70**	**80**	**90**	**100**
	467.74	451.49	306.22	238.1
	467.47	451.57	306.24	237.62
	472.21	451.6	306.25	238.51
	461.79	451.69	306.24	238.18
	463.81	451.55	306.15	237.14
Average	466.604	451.58	306.22	237.91
t_H	0.005	0.005	0.011	0.018

Table D: Flow-through times for H^+-0614-3 XCD in solvents containing various fractions of MQ-water and DMSO. The arithmetic average and the Hagenbach Correction Time (t_H) are presented in the two lower rows. The flow-through times were measured at 0.5 mg/mL.

	Flow-through time [s]						
w/w% DMSO	**0**	**10**	**20**	**30**	**40**	**50**	**60**
	349.34	430.53	352.02	537.06	521.74	700.07	713.24
	349.36	430.74	350.45	538.49	521.9	700.09	713.7
	354.17	430.84	354.32	538.4	521.66	699.51	713.08
	353.32	432.41	360.8	537.71	521.52	699.38	713.12
	352.95	432.49	354.65	538.24	521.29	698.51	712.37
Average	351.83	431.40	354.45	537.98	521.62	699.51	713.03
t_H	0.008	0.005	0.008	0.003	0.004	0.002	0.002

	Flow-through time [s]						
w/w% DMSO	**70**	**80**	**85**	**90**	**95**	**97.5**	**100**
	676.77	590.42	401.81	305.86	304.84	254.12	233.04
	676.24	589.92	402.83	305.83	304.86	256.43	233.24
	676.13	590.5	401.88	305.94	304.47	253.93	233.26
	675.78	590.27	401.8	305.81	305.27	253.78	233.73
	674.16	589.19	401.86	305.73	304.79	253.67	233.53
Average	675.82	590.06	402.04	305.83	304.85	254.39	233.36
t_H	0.002	0.003	0.006	0.011	0.011	0.015	0.018

Table E: Flow-through times for acetate- and pyruvate-free H^+-0614-3 XCD in solvents containing various fractions of MQ-water and DMSO. The arithmetic average and the Hagenbach correction factor (HCF) are presented in the two lower rows. The flow-through times were measured at 0.5 mg/mL.

	Flow-through time [s]				
w/w% DMSO	**0**	**20**	**30**	**40**	**50**
	252.63	371.56	452.27	515.17	669.8
	252.65	381.28	452.68	515.53	668.57
	252.94	381.89	452.53	515.06	668.54
	252.92	381.9	452.45	515.02	669.84
	252.94	381.7	452.39	515.15	668.97
Average	**252.82**	**379.67**	**452.46**	**515.19**	**669.14**
t_H	0.016	0.007	0.005	0.004	0.002

	Flow-through time [s]			
w/w% DMSO	**70**	**80**	**90**	**100**
	649.01	620.11	413.88	329.48
	654.92	622.50	413.53	329.37
	652.88	621.85	413.62	329.95
	649.01	621.88	413.3	329.76
	650.44	621.56	415.48	329.29
Average	**651.25**	**621.58**	**413.96**	**329.57**
t_H	0.002	0.003	0.006	0.009

Calculation of Reduced Viscosity

When the flow-through time of both the sample and the sample solvent is known, the relative viscosity can be calculated by applying Equation (3-20). An example calculation is shown below for H^+-MX_{10} dissolved in 100% DMSO. This sample have an average flow-through time of 237.91 s, while the solvent has an average flow-through time of 179.31 s. The Hagenbach Correction Time of the solvent and sample were determined to be 0.031 s and 0.018 s, respectively. Thus, the relative viscosity with Hagenbach correction becomes

$$\eta_r = \frac{t - t_H}{t_0 - t_H} = \frac{237.91\ \text{s} - 0.018\ \text{s}}{179.31\ \text{s} - 0.031\ \text{s}}$$

$$\eta_r = 1.33$$

With η_r know, the specific viscosity, can be calculated by applying Equation (3-21). For the sample above.

$$\eta_{sp} = \eta_r - 1 = 1.33 - 1$$

$$\eta_{sp} = 0.33$$

The reduced viscosity is found by dividing η_{sp} by the analysis concentration. The unit of the concentration should be g/mL. For the sample above:

$$\frac{\eta_{sp}}{c} = \frac{0.33}{0.001\ \text{g/mL}}$$

$$\frac{\eta_{sp}}{c} = 326.9\ \text{mL/g}$$

F Refractive Index Increment

In order to perform calculations on light scattering data, the refractive index increment ($\frac{\partial n}{\partial c}$) at the light scattering wavelength (532 nm) has to be known. The refractive index increment was determined using a Schulz-Cantow photoelectric differential refractometer, where the difference between the refractive index of the solvent and sample is determined. Measurements should be performed on both left- and right-hand side of the sample cell, covering the opposite side for both the solvent and the sample. The maximum electrical current flowing through the sample were noted and measurements were performed at the half of the maximum voltage ± 10 μA. The electrical current was read of a voltmeter, and had a corresponding number reflecting the amount of light passing through the sample, n. The distance between pure solvent and the sample, both measured at both left- and right-hand side (n_l and n_r respectively) were further determined.

ΔD was multiplied with a constant of the filter of known wavelength to provide the difference in refractive index between the sample and pure solvent (Δn). $\frac{\partial n}{\partial c}$ was obtained as the slope of Δn measurements performed at different concentrations plotted against the respective concentration. These regression models are presented in section F.1, while section F.2 demonstrate the calculation of $\frac{\partial n}{\partial c}$ at the temperatures that were not measured by differential refractometry.

F.1 Regression Models

F.1.1 H^+-MX_{10} in MQ-water, 20°C

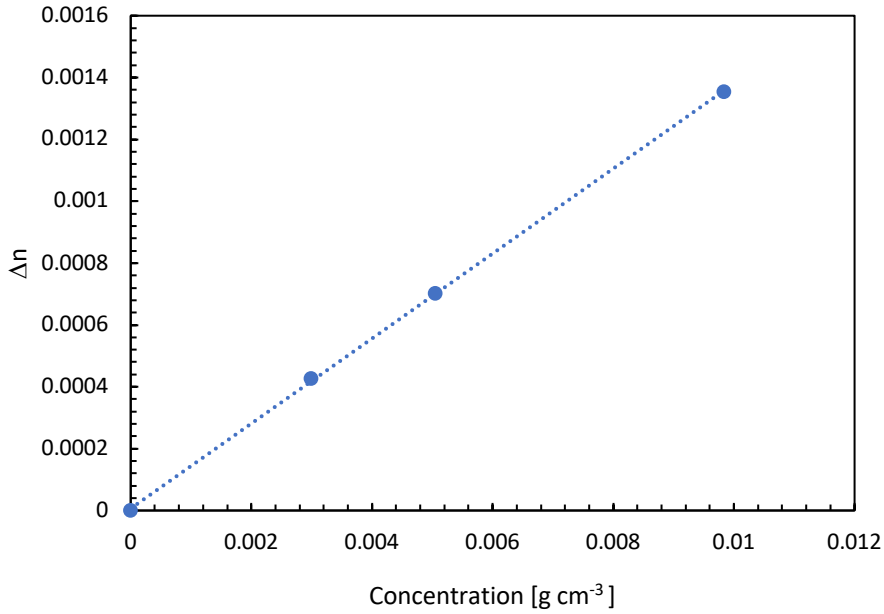

Figure D: The regression model of the difference in refractive index between H^+-MX_{10} in MQ-water and pure MQ-water (Δn) as a function of the MX concentration. Measurements were made at 436 nm and 20°C. The regression equation was determined to be y = 0.1374x + 7E-06, R^2 = 0.9999

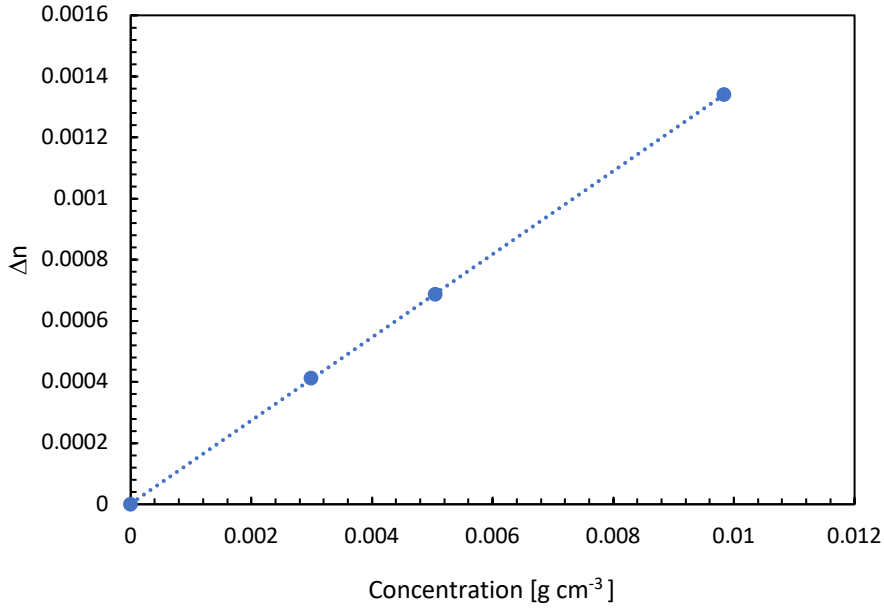

Figure E: The regression model of the difference in refractive index between H^+-MX_{10} in MQ-water and pure MQ-water (Δn) as a function of the MX concentration. Measurements were made at 488 nm and 20°C. The regression equation was determined to be y = 0.1361x + 2E-06, R^2 = 1

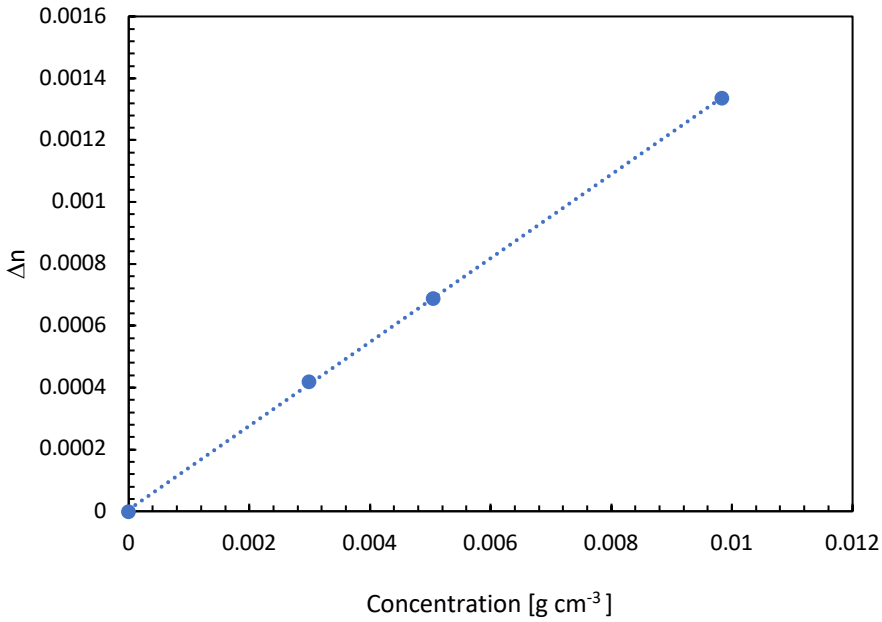

Figure F: The regression model of the difference in refractive index between H^+-MX_{10} in MQ-water and pure MQ-water (Δn) as a function of the MX concentration. Measurements were made at 546 nm and 20°C. The regression equation was determined to be y = 0.1355x + 5E-06, R^2 = 0.9999

F.1.2 H^+-MX_{10} in MQ-water, 50°C

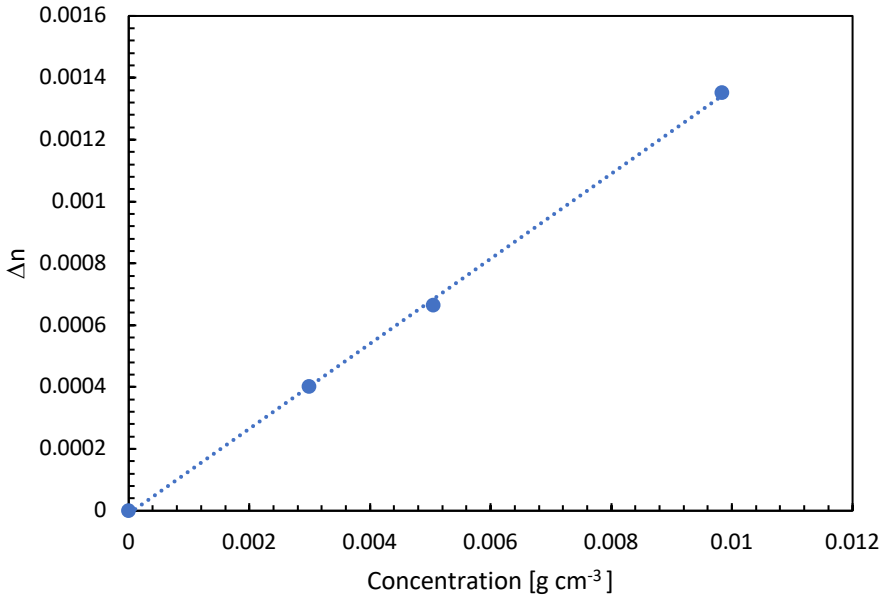

Figure G: The regression model of the difference in refractive index between H^+-MX_{10} in MQ-water and pure MQ-water (Δn) as a function of the MX concentration. Measurements were made at 436 nm and 50°C. The regression equation was determined to be y = 0.1374x - 1E-05, R^2 = 0.9995

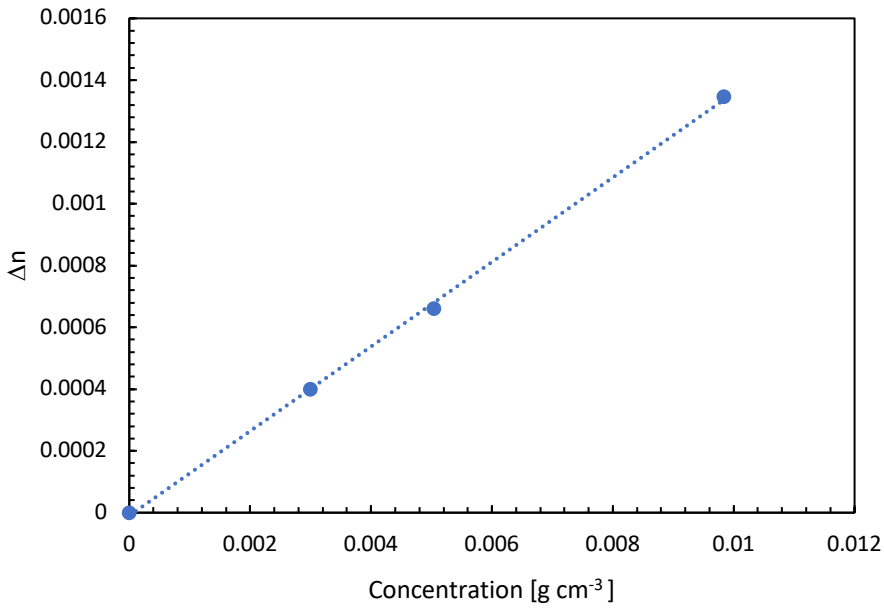

Figure H: The regression model of the difference in refractive index between H^+-MX_{10} in MQ-water and pure MQ-water (Δn) as a function of the MX concentration. Measurements were made at 488 nm and 50°C. The regression equation was determined to be y = 0.1368x - 1E-05, R^2 = 0.9994

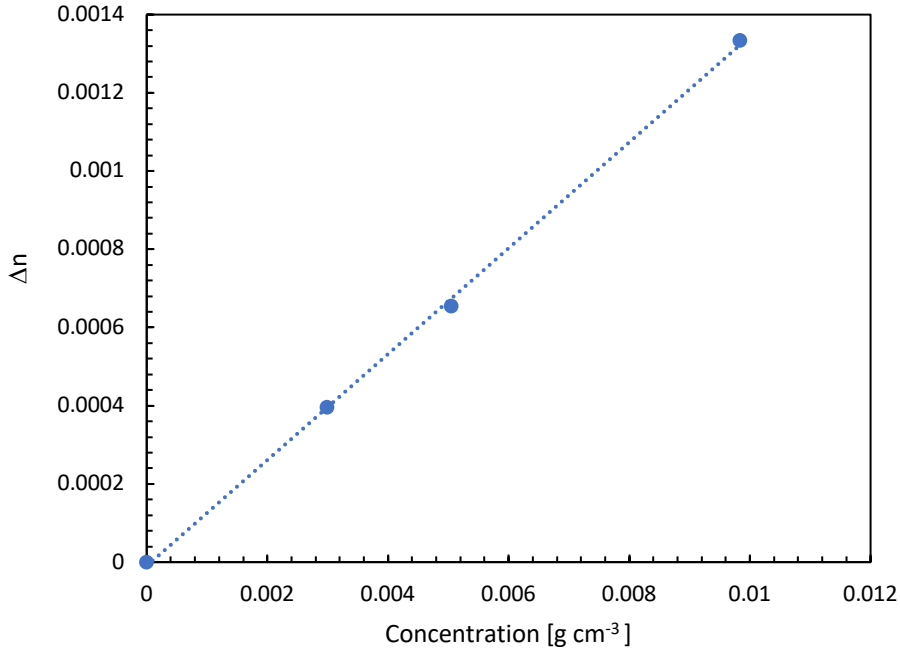

Figure I: The regression model of the difference in refractive index between H^+-MX_{10} in MQ-water and pure MQ-water (Δn) as a function of the MX concentration. Measurements were made at 546 nm and 50°C. The regression equation was determined to be y = 0.1354x - 1E-05, R^2 = 0.9994

F.1.3 Acetate- and Pyruvate-Free H^+-MX_{10} in MQ-water, 20°C

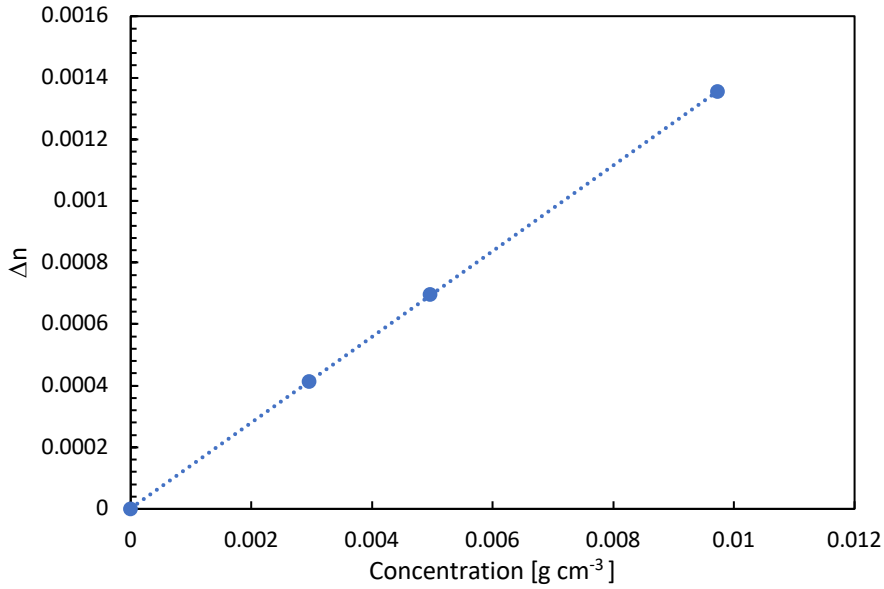

Figure J: The regression model of the difference in refractive index between acetate- and pyruvate-free H^+-MX_{10} in MQ-water and pure MQ-water (Δn) as a function of the MX concentration. Measurements were made at 436 nm and 20°C. The regression equation was determined to be y = 0.1392x + 2E-06, R^2 = 1

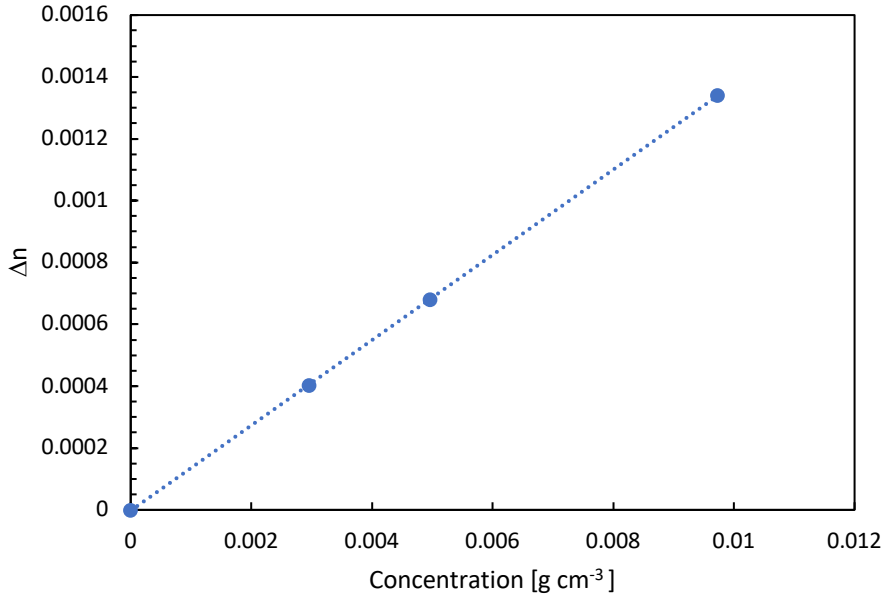

Figure K: The regression model of the difference in refractive index between acetate- and pyruvate-free H^+-MX_{10} in MQ-water and pure MQ-water (Δn) as a function of the MX concentration. Measurements were made at 488 nm and 20°C. The regression equation was determined to be y = 0.1378x + 2E-06, R^2 = 1

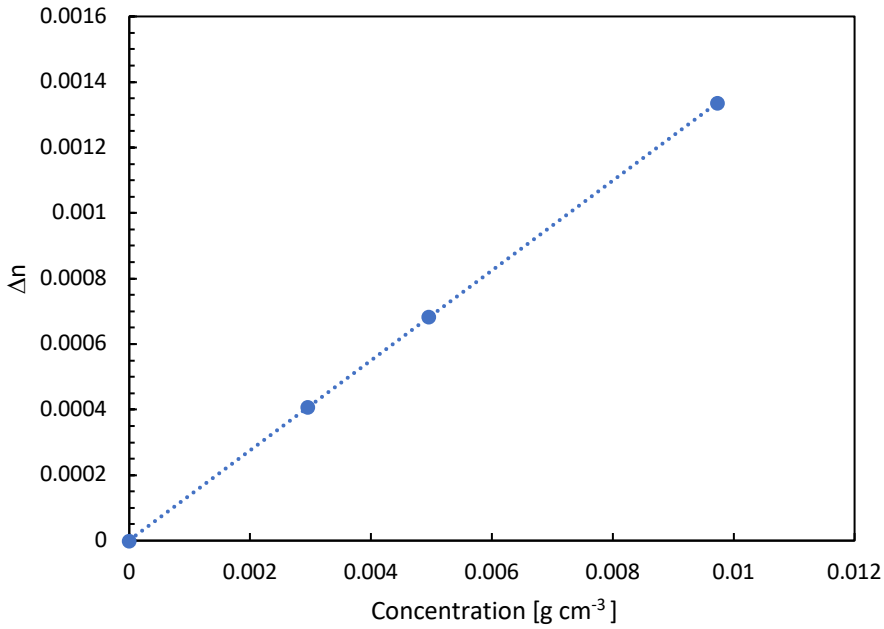

Figure L: The regression model of the difference in refractive index between acetate- and pyruvate-free H^+-MX_{10} in MQ-water and pure MQ-water (Δn) as a function of the MX concentration. Measurements were made at 546 nm and 20°C. The regression equation was determined to be y = 0.1372x + 1E-06, R^2 = 1

F.1.4 Acetate- and Pyruvate-Free H^+-MX_{10} in MQ-water, 50°C

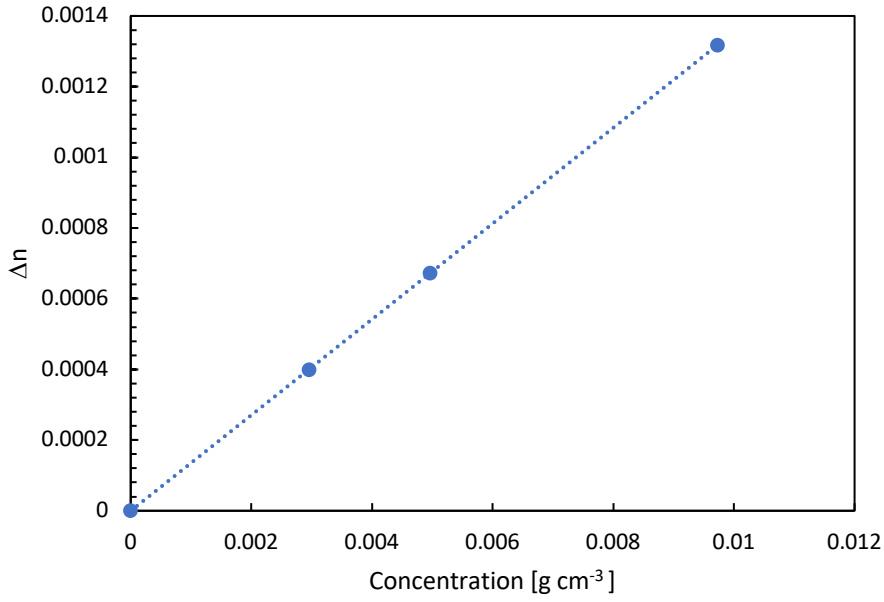

Figure M: The regression model of the difference in refractive index between acetate- and pyruvate-free H^+-MX_{10} in MQ-water and pure MQ-water (Δn) as a function of the MX concentration. Measurements were made at 436 nm and 50°C. The regression equation was determined to be y = 0.1355x + 3E-07, R^2 = 1

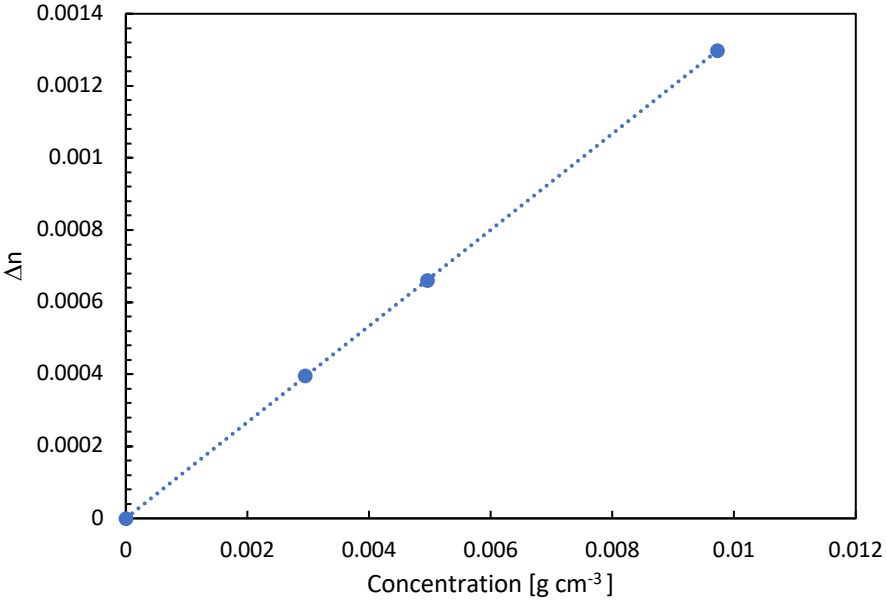

Figure N: The regression model of the difference in refractive index between acetate- and pyruvate-free H^+-MX_{10} in MQ-water and pure MQ-water (Δn) as a function of the MX concentration. Measurements were made at 546 nm and 50°C. The regression equation was determined to be y = 0.1334x + 3E-07, R^2 = 1

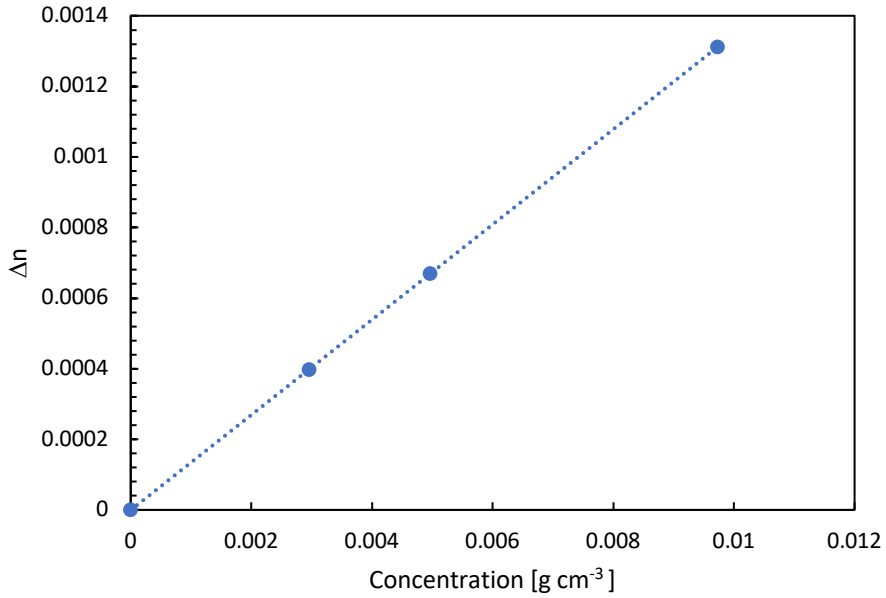

Figure O: The regression model of the difference in refractive index between acetate- and pyruvate-free H^+-MX_{10} in MQ-water and pure MQ-water (Δn) as a function of the MX concentration. Measurements were made at 488 nm and 50°C. The regression equation was determined to be y = 0.1348x - 5E-07, R^2 = 1

F.1.5 H^+-MX_{10} in DMSO, 20°C

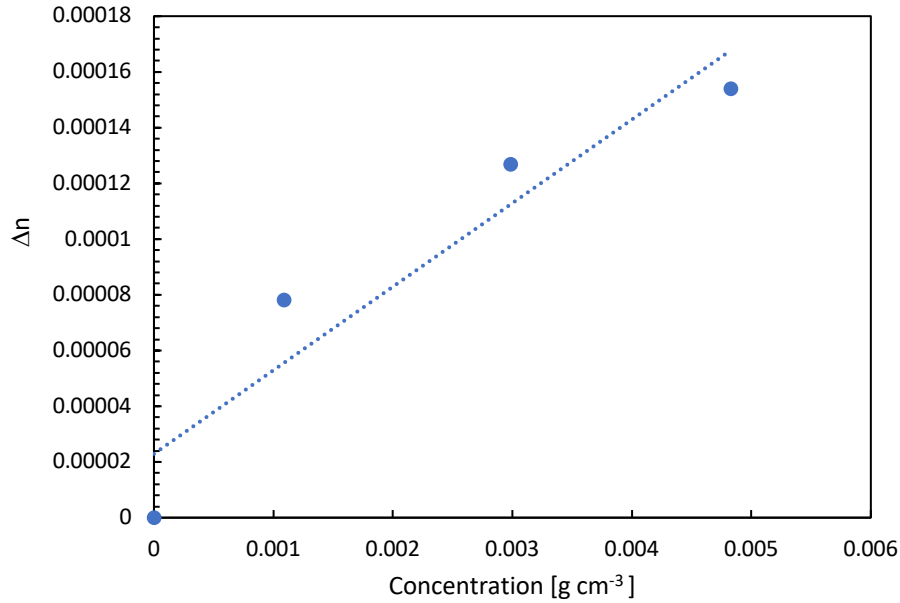

Figure P: The regression model of the difference in refractive index between H^+-MX_{10} in DMSO and pure DMSO (Δn) as a function of the MX concentration. Measurements were made at 436 nm and 20°C. The regression equation was determined to be y = 0.03x + 2E-05, R^2 = 0.8952

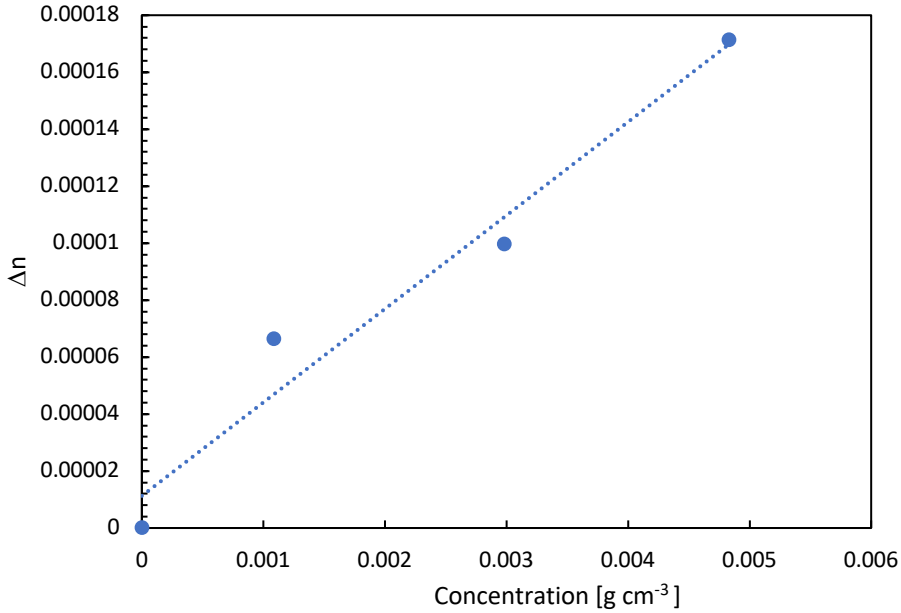

Figure Q: The regression model of the difference in refractive index between H^+-MX_{10} in DMSO and pure DMSO (Δn) as a function of the MX concentration. Measurements were made at 488 nm and 20°C. The regression equation was determined to be y = 0.0328x + 1E-05, R^2 = 0.9611

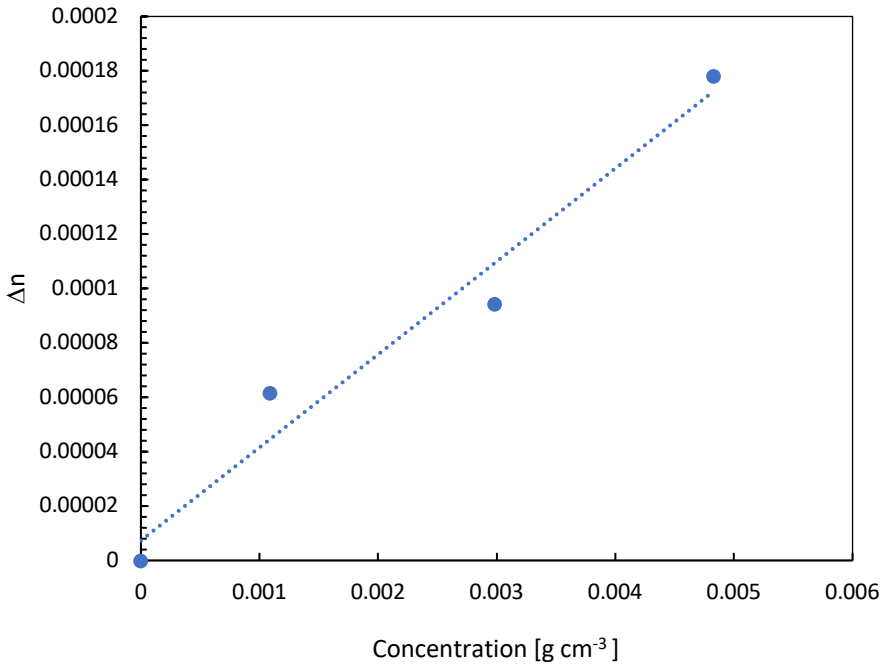

Figure R: The regression model of the difference in refractive index between H^+-MX_{10} in DMSO and pure DMSO (Δn) as a function of the MX concentration. Measurements were made at 488 nm and 20°C. The regression equation was determined to be y = 0.0342x + 7E-06, R^2 = 0.9639

F.1.6 Acetate- and Pyruvate-Free H^+-MX_{10} in DMSO, 20°C

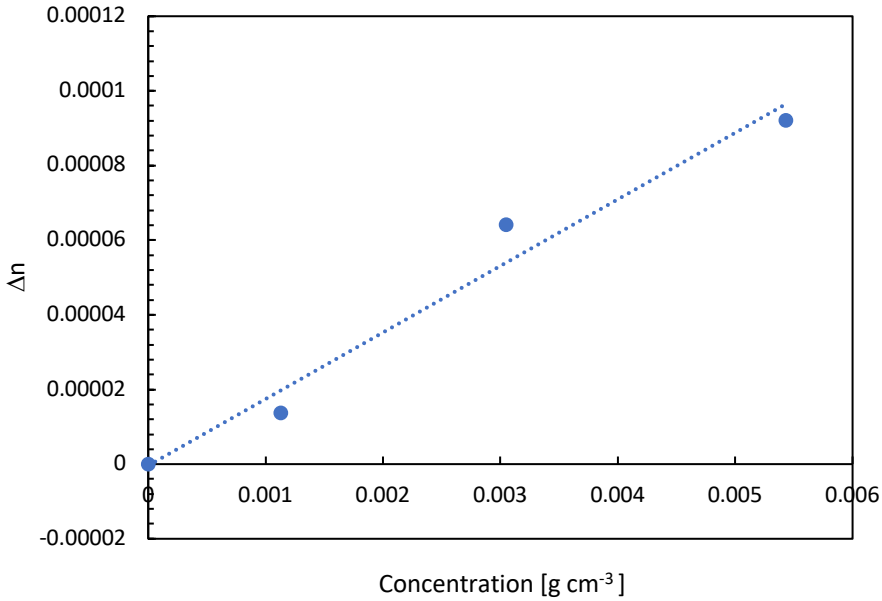

Figure S: The regression model of the difference in refractive index between acetate- and pyruvate-free H^+-MX_{10} in DMSO and pure DMSO (Δn) as a function of the MX concentration. Measurements were made at 436 nm and 20°C. The regression equation was determined to be y = 0.0178x - 4E-07, R^2 = 0.9716

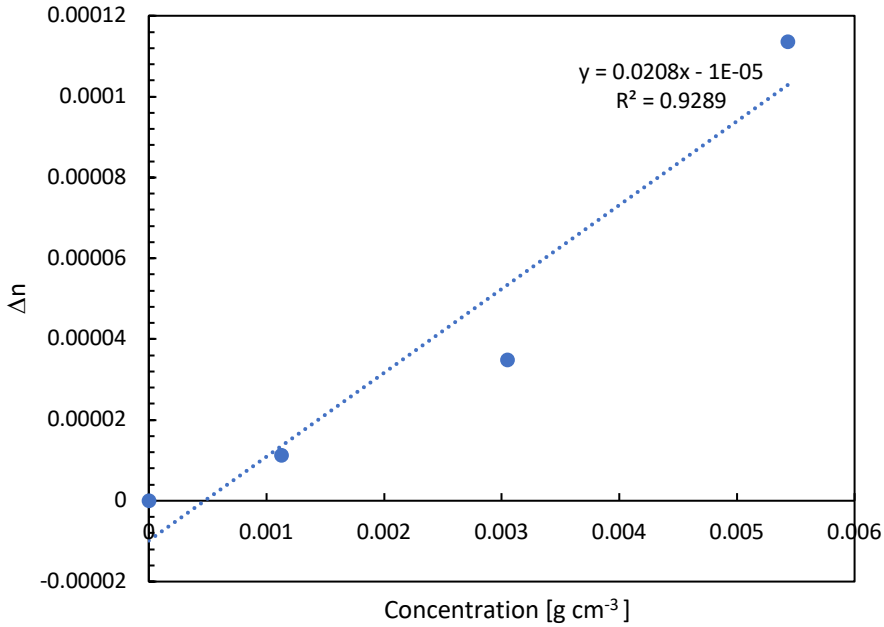

Figure T: The regression model of the difference in refractive index between acetate- and pyruvate-free H^+-MX_{10} in DMSO and pure DMSO (Δn) as a function of the MX concentration. Measurements were made at 488 nm and 20°C. The regression equation was determined to be y = 0.0208x - 1E-05, R^2 = 0.9289

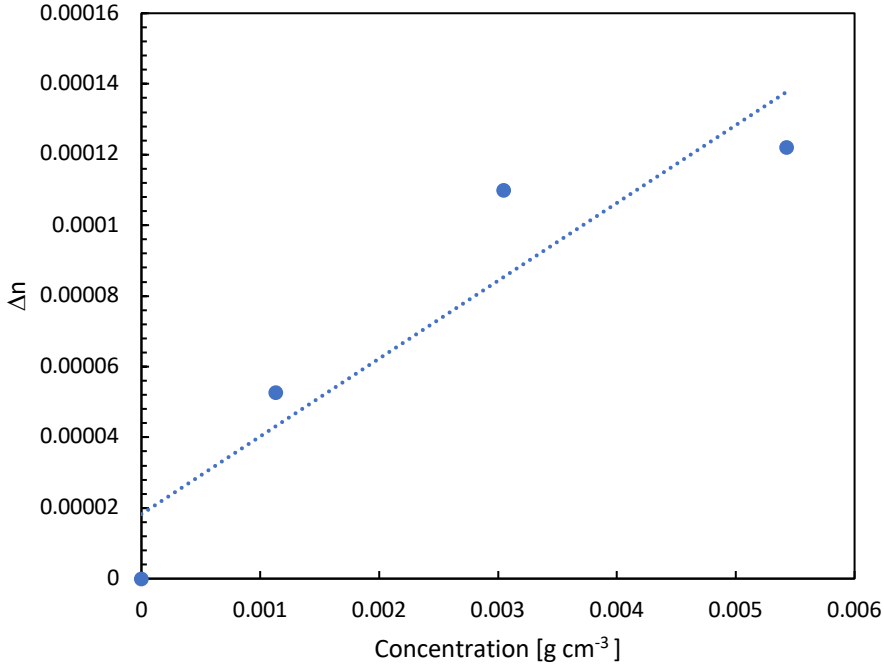

Figure U: The regression model of the difference in refractive index between acetate- and pyruvate-free H^+-MX_{10} in DMSO and pure DMSO (Δn) as a function of the MX concentration. Measurements were made at 546 nm and 20°C. The regression equation was determined to be y = 0.022x + 2E-05, R^2 = 0.8658

F.2 Calculation of Refractive Index Increment

F.2.1 MQ-Water as Solvent

For native and acetate-and pyruvate-free H^+-MX_{10} samples dissolved in MQ-water, the refractive index increments were determined from the regression slope of the difference in refractive index between the sample and pure MQ-water as a function of concentration. As measurements were performed at both 20 and 50°C, $\frac{\partial n}{\partial c}$ were obtained directly for these temperatures. However, to obtain information on $\frac{\partial n}{\partial c}$ at 30 and 40°C, which also were studied by light scattering, a regression model of $\frac{\partial n}{\partial c}$ as a function of temperature was constructed for both native and acetate- and pyruvate-free MX_{10}. From the regression equations, $\frac{\partial n}{\partial c}$ at 30 and 40°C were determined. The regression model of native and acetate- and pyruvate-free MX_{10} are presented in Figure V and Figure W, respectively.

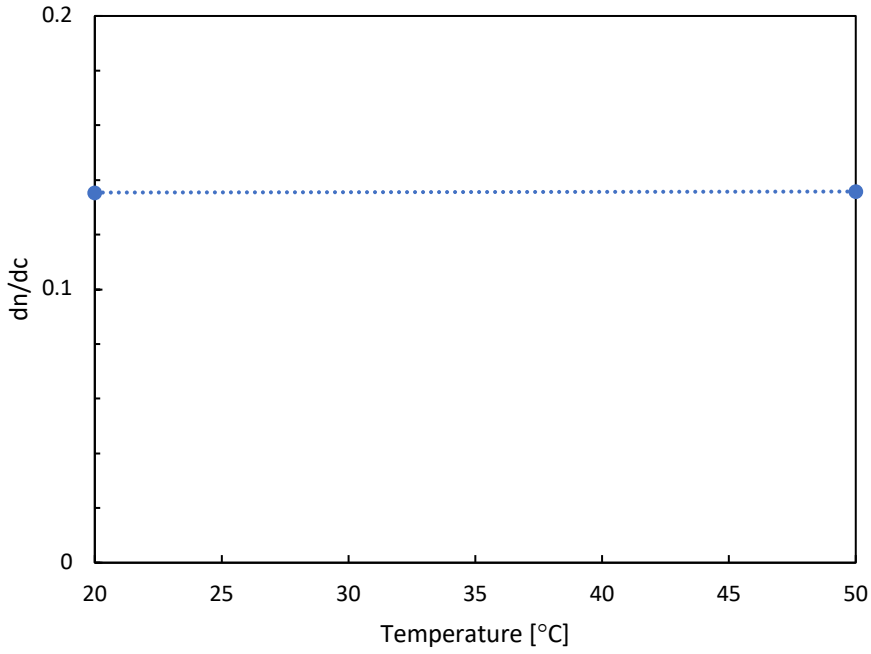

Figure V: The regression model of the refractive index increment ($\frac{\partial n}{\partial c}$)of native MX_{10} as a function of temperature, constructed to determine $\frac{\partial n}{\partial c}$ at 30 and 40°C. The regression equation was determined to be y = 1.23E-05x + 0.1352

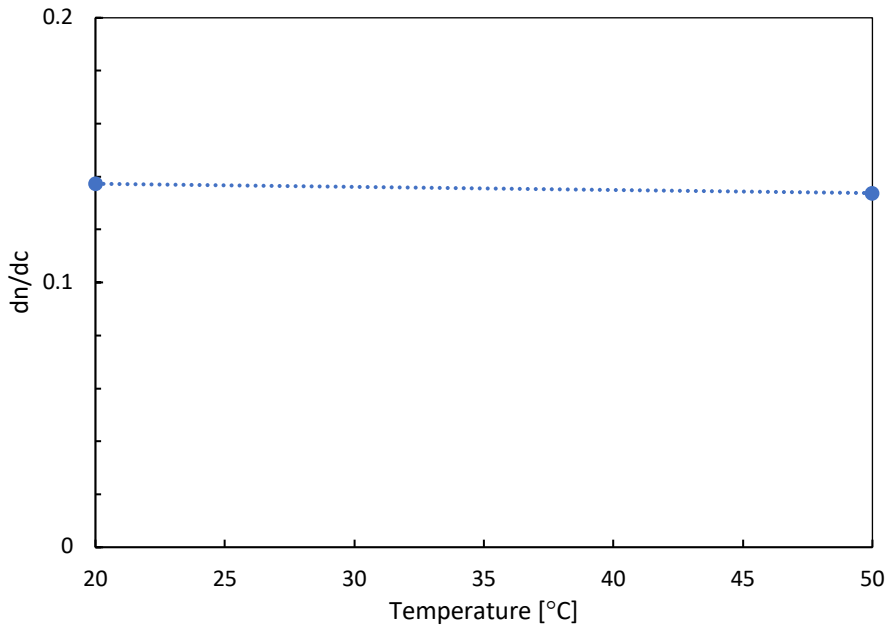

Figure W: The regression model of the refractive index increment ($\frac{\partial n}{\partial c}$)of acetate- and pyruvate free MX_{10} as a function of temperature, constructed to determine $\frac{\partial n}{\partial c}$ at 30 and 40°C. The regression equation was determined to be y = -0.0001x + 0.1397

An example calculation of $\frac{\partial n}{\partial c}$ for native MX_{10} at 30°C is presented below:

The regression model of $\frac{\partial n}{\partial c}$ for native MX_{10} as a function of temperature were determined to be

$$y = 1.23E-05x + 0.1352$$

Inserting 30°C for x results in the following expression

$$y = 1.23E-05 \cdot 30 + 0.1352$$

$$\underline{y = 0.136}$$

F.2.2 DMSO as Solvent

For native and acetate-and pyruvate-free H^+-MX_{10} dissolved in DMSO, $\frac{\partial n}{\partial c}$ were only measured at 20°C due to high absorption of water when temperature was increased. This was observed through a fluctuating electrical current on the voltmeter attached to the refractometer. Thus, was not possible to obtain regression models similar to those presented for MX in MQ-water. To determine $\frac{\partial n}{\partial c}$ at the other temperatures, i.e. 30, 40 and 50°C, regression models were

constructed using the slope of the respective MX sample in MQ-water, assuming that the same MX sample show similar temperature dependency in both MQ-water and DMSO. The intercepts were determined by calculating the difference between the value of $\frac{\partial n}{\partial c}$ at 20°C and the intercept of the MX sample in MQ-water and subtracting this value from the value of $\frac{\partial n}{\partial c}$ obtained at 20°C for the MX sample in DMSO. An example calculation of the procedure is presented below for native MX_{10}:

The $\frac{\partial n}{\partial c}$ at 20°C for native MX_{10} dissolved in DMSO were determined to be 0.03398. The slope to construct the regression model was obtained from the regression equation of native MX_{10} dissolved in MQ-water, i.e. $1.23 \cdot 10^{-5}$ °C^{-1}.

The intercept of the regression model was calculated by difference between the value of $\frac{\partial n}{\partial c}$ at 20°C and the intercept of the MX sample in MQ-water:

$$\Delta = \frac{\partial n}{\partial c}_{MQ-water,20°C} - Intercept_{(MQ-water)}$$

$$\Delta = 0.13541 - 0.13517 = 0.00025$$

The value obtained for Δ were subtracted from the $\frac{\partial n}{\partial c}$ obtained for MX in DMSO at 20°C:

$$Intercept_{(DMSO)} = 0.03398 - 0.00025$$

$$Intercept_{(DMSO)} = 0.03373$$

Combining the slope and the calculated intercept, the regression model for MX_{10} in DMSO becomes $y = 1.23 \cdot 10^{-5}x + 3.37 \cdot 10^{-2}$

The regression models of native and acetate- and pyruvate-free MX_{10} in DMSO are presented in Figure X and Figure Y, respectively.

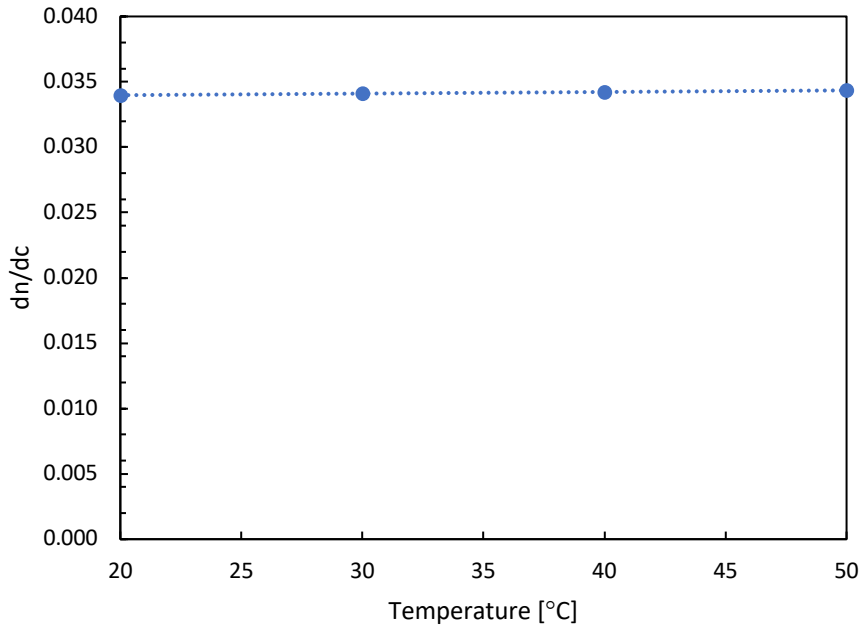

Figure X: The regression model of the refractive index increment ($\frac{\partial n}{\partial c}$)of native MX_{10} in DMSO as a function of temperature, constructed to determine $\frac{\partial n}{\partial c}$ at 30, 40 and 50°C. The regression equation was determined to be $y = 1.23 \cdot 10^{-5}x + 3.37 \cdot 10^{-2}$

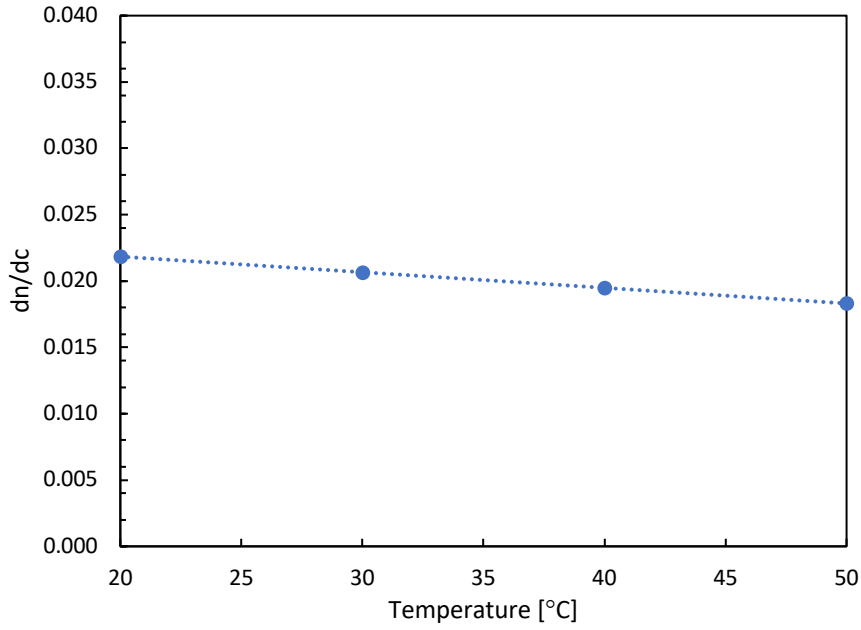

Figure Y: The regression model of the refractive index increment ($\frac{\partial n}{\partial c}$)of acetate- and pyruvate-free MX_{10} in DMSO as a function of temperature, constructed to determine $\frac{\partial n}{\partial c}$ at 30, 40 and 50°C. The regression equation was determined to be $y = -0.0001x + 0.0242$

Karina Gjerdevik Osebakken

Conformation of the Acid Form of Xanthan

NTNU
Norwegian University of
Science and Technology